Titre: Title:	Non-Equilibrium SiGeSn Group IV Heterostructures and Nanowires for Integrated Mid-Infrared Photonics
Auteur: Author:	Anis Attiaoui
Date:	2018
Type:	Mémoire ou thèse / Dissertation or Thesis
Référence: Citation:	Attiaoui, A. (2018). Non-Equilibrium SiGeSn Group IV Heterostructures and Nanowires for Integrated Mid-Infrared Photonics [Mémoire de maîtrise, École Polytechnique de Montréal]. PolyPublie. https://publications.polymtl.ca/3289/

URL de PolyPublie: PolyPublie URL:	https://publications.polymtl.ca/3289/
Directeurs de recherche: Advisors:	Oussama Moutanabbir
Programme: Program:	Génie physique

UNIVERSITÉ DE MONTRÉAL

NON-EQUILIBRIUM SiGeSn GROUP IV HETEROSTRUCTURES AND NANOWIRES FOR INTEGRATED MID-INFRARED PHOTONICS

ANIS ATTIAOUI

DÉPARTEMENT DE GÉNIE PHYSIQUE

ÉCOLE POLYTECHNIQUE DE MONTRÉAL

MÉMOIRE PRÉSENTÉ EN VUE DE L'OBTENTION DU DIPLÔME DE

MAÎTRISE ÈS SCIENCES APPLIQUÉES

(GÉNIE PHYSIQUE)

AOÛT 2018

UNIVERSITÉ DE MONTRÉAL

ÉCOLE POLYTECHNIQUE DE MONTRÉAL

Ce mémoire intitulé :

NON-EQUILIBRIUM SiGeSn GROUP IV HETEROSTRUCTURES AND NANOWIRES FOR INTEGRATED MID-INFRARED PHOTONICS

présenté par : ATTIAOUI Anis

en vue de l'obtention du diplôme de : Maîtrise ès sciences appliquées

a été dûment accepté par le jury d'examen constitué de :

M. FRANCOEUR Sébastien, Ph. D., président

M. MOUTANABBIR Oussama, Ph. D., membre et directeur de recherche

Mme HINZER Karin, Ph. D, membre externe

DEDICATION

TO MY MOTHER AND MY BROTHER

ACKNOWLEDGEMENTS

First and foremost, I would like to express my deepest gratitude and appreciation to my supervisor, Prof. Oussama Moutanabbir, for his invaluable guidance over the last years. His solid knowledge, creative thinking as well as his passion and diligence in research have truly inspired me. My candidature could never be easier without his heartfelt support, strict training, and constant encouragement.

Next, I would like to take this opportunity to thank my colleagues at the Nano and Quantum Semiconductors Laboratory (NHL). My work would not have been finished without their help. I would like to express my tremendous appreciation to Dr. Bill Baloukas and Dr. Simon Lokai for their patient training, generous help, and thoughtful discussions, which benefited me through and beyond my candidature. Besides, I would like to thank my group mates and my friends: Jean-Hughes Lupien Fournier, Fred Vhenes, Simone Assali, Samik Mukherjee, Mathieu-Fortin Dêschenes… I would also like to convey my special thanks and appreciation to the staffs of LCM, Patricia Moraille, Adèle El-Murr, and Joël Bouchard for their support and help.

At the end, I would like to extend my deepest gratitude to my family. I would like to thank my mother, and brother for their unwavering love, support, and encouragement.

RÉSUMÉ

Le développement des nouvelles générations de dispositifs électroniques devient de plus en plus limité par la chaleur générée par effet Joule dans les puces électroniques à haute densité. Des circuits photoniques intégrés sur silicium (Si) compatibles avec les procédés CMOS ont été proposés comme solution rentable pour réduire le réchauffement des dispositifs tout en améliorant leur performance globale. Cependant, les émetteurs à base de Si sont jusqu'à présent les composantes les plus difficiles à concevoir pour ces circuits photoniques intégrés. La principale raison est la bande interdite indirecte qui limite sévèrement l'efficacité de la luminescence du Si. Récemment l'incorporation de l'étain (Sn) dans des alliages silicium-germanium représente une nouvelle direction de recherche qui mènera à des semiconducteurs de groupe IV ayant une bande interdite directe. Les semiconducteurs obtenus $Ge_{1-x-y}Si_xSn_y$ sont des alliages ternaires du groupe IV compatibles avec la technologie CMOS, et peuvent avoir une bande interdite directe ajustable en fonction de la composition et de la contrainte. Ces propriétés ont généré un grand intérêt pour développer ces semiconducteurs et mieux comprendre leurs propriétés.

Dans cette perspective, ce travail présente une étude détaillée de la structure de bande de l'alliage ternaire $Ge_{1-x-y}Si_xSn_y$ contraint et relaxé en utilisant une approche théorique fondée sur le modèle des liaisons fortes. Cette méthode est basée sur une évaluation précise des constantes de déformation de Ge, Si et α-Sn en utilisant une approche stochastique de Monte-Carlo ainsi qu'une méthode d'optimisation basée sur le gradient. De plus, une nouvelle approche d'évolution différentielle efficace est également développée pour reproduire avec précision les masses effectives expérimentales et les énergies de bandes interdites. Sur la base de ces approches, nous avons élucidé l'influence du désordre dans la structure crystalline, de la contrainte et de la composition sur l'énergie de bande interdite de $Ge_{1-x-y}Si_xSn_y$. Quand $0 \leq x \leq 0.4$ et $0 \leq y \leq 0.2$, nous avons trouvé que la contrainte élastique réduit la concentration critique de Sn nécessaire pour obtenir un semiconducteur à bande interdite directe avec des énergies de bande interdite correspondantes inférieures à 0.76 eV. Cette limite supérieure diminue à 0.43 eV pour les alliages ternaires à bande interdite directe complètement relaxés. La transition obtenue vers la bande interdite directe en fonction de la composition est décrite par $y > 0.605x + 0.077$ et $y > 1.364x + 0.107$ respectivement pour les alliages contraints et complètement relaxés. Les effets de la contrainte, à une composition fixe, sur la transition de bande interdite indirecte à directe ont également été étudiés et discutés.

Ensuite, en s'appuyant sur les connaissances acquises à partir des calculs de la structure de bande déjà effectués, nous avons étudié la quantification du confinement des électrons et des trous dans un système de nanofils cœur/couronne $Ge_{1-y}Sn_y/Ge$. À cette fin, les décalages de bande de conduction et de valence ont été évalués. Ensuite, l'équation de masse effective de Schrödinger a été résolue en coordonnées cylindriques en utilisant une technique de différence finie classique pour la géométrie de nanofil. Le rayon du cœur et l'effet de la concentration de dopage sur la distribution de la densité des électrons et des trous sont quantifiés en évaluant l'écart des porteurs de charges normalisée par rapport au cœur. Nous avons trouvé qu'au-dessus d'une concentration de dopage critique de 5×10^{16} cm^{-3} et inférieure à un rayon du cœur de 20 nm, la densité électronique est localisée dans le cœur de Ge pour un système de nanofil cœur/couronne de $Ge_{0.9}Sn_{0.1}/Ge$.

Finalement, la compréhension de l'interaction de la lumière avec les structures $Ge_{1-x-y}Si_xSn_y$ a été élaborée. Nous avons comparé les efficacités d'absorption et de diffusion de couches minces et de nanofils. À cet égard, une étude détaillée de l'influence des couches minces et de nanofils à base de $Ge_{1-x-y}Si_xSn_y$ sur les propriétés optiques a été effectuée. Nous avons trouvé qu'en ajoutant une fine couche d'encapsulation de $Ge_{1-x-y}Si_xSn_y$ sur Si ou Ge, l'absorption de la lumière est grandement améliorée, particulièrement dans la région de l'infra-rouge proche, ce qui entraîne une augmentation de la densité du courant de court-circuit. Pour des couches minces de $Ge_{1-x-y}Si_xSn_y$ ayant des épaisseurs inférieures à 30 nm, une augmentation de 14 fois du courant de court-circuit par rapport au Si a été observée. Cette amélioration diminue en réduisant l'épaisseur de la couche de recouvrement. Inversement, il a été constaté que la diminution de l'épaisseur de la couche de recouvrement améliorait le courant de court-circuit dans les nanofils de type cœur/couronne de $Si/Ge_{1-x-y}Si_xSn_y$ et de $Ge/Ge_{1-x-y}Si_xSn_y$. L'absorption optique devient très importante en augmentant la teneur en Sn. De plus, en exploitant un effet de résonance optique, ces nanofils présentent une absorption lumineuse extrême atteignant un facteur d'amélioration, par rapport aux nanofils simples de Si ou Ge, d'ordre de 10^4 pour $Si/Ge_{0.84}Si_{0.04}Sn_{0.12}$ et de 12 pour $Ge/Ge_{0.84}Si_{0.04}Sn_{0.12}$. En outre, nous avons analysé la réponse optique de l'addition d'une couche diélectrique de Si_3N_4 au nanofil de type cœur/enveloppe $Si/Ge_{1-x-y}Si_xSn_y$ et nous avons trouvé approximativement une augmentation de 50% dans la densité du courant de court-circuit pour une couche diélectrique d'épaisseur égale à 45 nm et un rayon de cœur et une épaisseur d'enveloppes supérieures à 40 nm. L'augmentation des effets optiques dans la structure cœur-enveloppe s'expliquera par la combinaison de l'amélioration apportée par des résonances en mode dans la partie semi-conductrice

et des effets antireflet dans la partie diélectrique. Ces résultats préparent le terrain pour concevoir et optimiser les dispositifs optoélectroniques et photoniques à base des semiconducteurs $Ge_{1-x-y}Si_xSn_y$.

ABSTRACT

Progress in electronic devices has been increasingly limited by the heat generated due to Joule effect in high density electronic chips. Silicon (Si) integrated photonic circuits compatible with CMOS processing has been proposed as a viable solution to reduce the heating of devices while improving their overall performance. However, Si-based emitters are, until now, the most difficult components to design for these integrated photonic circuits. The main reason is the indirect band gap which severely limits the efficiency of Si emission and absorption of light. Recently, the incorporation of tin (Sn) into silicon-germanium alloys has been proposed to overcome this fundamental limit. The obtained semiconductors are $Ge_{1-x-y}Si_xSn_y$ ternary alloys of Group IV elements compatible with CMOS technology, and may have a band gap that is adjustable depending on the composition and the strain. These properties have generated a great interest to grow these semiconductors and to better understand their optoelectronic and physical properties.

With this perspective, this work outlines detailed investigations of the band structure of strained and relaxed $Ge_{1-x-y}Si_xSn_y$ ternary alloys using a semi-empirical second nearest neighbors tight binding method. This method is based on an accurate evaluation of the deformation potential constants of Ge, Si, and a-Sn using a stochastic Monte-Carlo approach as well as a gradient based optimization method. Moreover, a new and efficient differential evolution approach is also developed to accurately reproduce the experimental effective masses and band gaps. Based on this, the influence of lattice disorder, strain, and composition on $Ge_{1-x-y}Si_xSn_y$ band gap energy and its directness were elucidated. For $0 \leq x \leq 0.4$ and $0 \leq y \leq 0.2$, tensile strain lowered the critical content of Sn needed to achieve a direct band gap semiconductor with the corresponding band gap energies below 0.76 eV. This upper limit decreases to 0.43eV for direct gap, fully relaxed ternary alloys. The obtained transition to direct band gap is given by $y > 0.605x + 0.077$ and $y > 1.364x + 0.107$ for epitaxially strained and fully relaxed alloys, respectively. The effects of strain, at a fixed composition, on band gap directness were also investigated and discussed.

Next, building upon the acquired knowledge from the band structure calculation, the analysis was extended toward quantifying the electron and hole confinement in a $Ge_{1-y}Sn_y$/Ge core/shell nanowire system. For that purpose, the conduction and valance band offsets were evaluated. Then, the effective mass Schrödinger equation was solved in cylindrical coordinates using a classical finite difference technique for a core-shell. The core radius and the doping

concentration effect on the electron and hole density distribution are quantified by evaluating a dimensionless core-normalized variance. Above a critical doping concentration of 5×10^{16} cm^{-3} and below a core radius of 20 nm, the electron density was found to be localized in the Ge core for the $Ge_{0.9}Sn_{0.1}$/Ge core-shell nanowire system.

Finally, understanding light interaction with the $Ge_{1-x-y}Si_xSn_y$ material system was the next step in our studies where the absorption and scattering efficiencies of thin-films and nanowires were evaluated based on the same material. With this perspective, a detailed investigation of the influence of $Ge_{1-x-y}Si_xSn_y$ layers on the optical properties of Si and Ge based heterostructures and nanowires is described. Adding a thin $Ge_{1-x-y}Si_xSn_y$ capping layer on Si or Ge greatly enhances light absorption especially in the near IR range leading to an increase in short-circuit current density. For the $Ge_{1-x-y}Si_xSn_y$ structure at thicknesses below 30 nm, a 14-fold increase in the short-circuit current is observed with respect to bare Si. This enhancement decreases by reducing the capping layer thickness. Conversely, decreasing the shell thickness was found to improve the short-circuit current in Si/$Ge_{1-x-y}Si_xSn_y$ and Ge/$Ge_{1-x-y}Si_xSn_y$ core/shell nanowires. The optical absorption becomes very significant as Sn content increases. Moreover, by exploiting an optical antenna effect, these nanowires show extreme light absorption reaching an enhancement factor, with respect to Si or Ge nanowires, on the order of 10^4 in Si/ $Ge_{0.84}Si_{0.04}Sn_{0.12}$ and 12 in Ge/ $Ge_{0.84}Si_{0.04}Sn_{0.12}$. Furthermore, the optical response of the addition of a dielectric layer of Si_3N_4 to the Si/$Ge_{1-x-y}Si_xSn_y$ core-shell nanowire was analyzed and approximatively 50% increase in the short-circuit current density was found for a dielectric layer of thickness equal to 45 nm and a core radius and shell thickness greater than to 40 nm. The core−shell optical antenna effect benefits from a multiplication of enhancements contributed by leaky mode resonances in the semiconductor part and antireflection effects in the dielectric part. These results lay the groundwork to design and optimize innovative optoelectronic and photonic devices based on the emerging semiconductors $Ge_{1-x-y}Si_xSn_y$.

TABLE OF CONTENTS

LIST OF TABLES

LIST OF FIGURES

LIST OF SYMBOLS

Symbol	Description	Unit
b	Optical band gap bowing parameter	
C_{abs}	Absorption cross-section	m^2
C_{sca}	Scattering cross-section	m^2
$Q_{abs}^{TE(TM)}$	Absorption efficiency for transverse electric (magnetic)	
$Q_{sca}^{TE(TM)}$	Scattering efficiency for transverse electric(magnetic)	
n	Refractive index	
n_D	n-type doping density	cm^{-3}
n_c	Core refractive index	
n_s	Shell refractive index	
λ	Wavelength	nm
λ_c	Cutoff Wavelength	nm
R_c	Core radius	nm
t	Shell thickness	nm
y_c	Critical direct-to-indirect crossover composition	(at. %)

LIST OF ABBREVIATIONS

1D	One-Dimensional
2D	Two-Dimensional
1NN-sp^3s^*	First-Nearest Neighbor sp^3s^* tight binding method
2NN-sp^3s^*	Second-Nearest Neighbor sp^3s^* tight binding method
ARC	Anti-Reflective Coating
ASTM	American Society for Testing Materials
CSNW	Core-Shell Nanowire
CBM	Conduction Band Minimum
DPC	Deformation Potential Constants
DFT	Density Functional Theory
ETBP	Empirical Tight Binding Parameters
Ge	Germanium
GeNW	Germanium Nanowire
$Ge_{1-y}Sn_y$	Germanium-Tin binary alloy ($0<y<1$)
$Ge_{1-x-y}Si_xSn_y$	Germanium-Silicon-Tin ternary alloy
GFP	Group- VI Photonics
IRPD	Infra-Red Photodetectors
IT	Information Technology
LCAO	linear combination of atomic orbitals
LMR	Leaky Mode Resonance
MC	Monte-Carlo
MIR	Mid-Infrared

NIR	Near-Infrared
NW	Nanowire
OEIC	Optoelectronic Integrated Circuits
PIC	Photonic Integrated Circuits
SE	Spectroscopic Ellipsometry
Si	Silicon
SiNW	Silicon Nanowire
SWIR	Short-wavelength Infrared
Sn	Tin
TE	Transverse Electric
TM	Transverse Magnetic
VCA	Virtual Crystal Approximation
VBM	Valance Band Maximum

LIST OF APPENDICES

CHAPTER 1 INTRODUCTION

Through the years, the power consumption of the information technology (IT) kept on increasing mainly as a result of the exponential growth in internet traffic which passed in 2016 the zettabyte (1 ZB = 2^{70} bytes) threshold and expected to increase nearly threefold over the next few years to reach the staggering figure of 25 GB per month per capita in 2020.[1] Additionally, networks required for the Internet of Everything and big data platforms will also show a significant growth from 4.9 billion machine-to-machine connections in 2015 to 12.2 billion by 2020.[1] This continuous evolution has been fueling an increasing demand for bandwidth and high-performance computing and signal processing while at the same time raising both technological and environmental concerns. This growing challenge is exacerbated by the driving paradigm of the IT industry which has always been “performance at low cost”. This approach faces another brick wall since the beginning of the past decade when fundamental thermal limits were reached by some integrated circuits (ICs), which are at the core of IT. As the transistor density has been increasing at Moore’s Law pace[2] and transistors are operated at higher frequency, the associated heat management has become a serious burden.[3] For instance, the electrical interconnect delay and power are some of the challenges that need to be addressed as devices scale down.[3] The scaling of electrical interconnections is limited by the physical properties of copper wires which suffers from heat dissipation via Joule effect. [4].

In addition to the scaling challenges, the need for enhanced performance also adds to the aforementioned burdens. For instance, while the input/output pad pitches will remain around 100 µm for IC chips, it is expected that the required line rate for inter-chip interconnect will exceed 40GB/s by 2020. So far, there is no solution to achieve this rate with electrical interconnects on a printed circuit board (PCB). Moreover, their high transmission loss on the PCB and reflections at connectors also limit the reach of electric wires at a high channel line rate. Due to this delay, the density of information that can be sent is limited in order to have good signal to noise ratio. The ITRS roadmap shows that the RC delay is expected to become significant, especially for global interconnects (long L).[5]

In addition to tackling the anticipated scientific and technological challenges, any progress in semiconductor industry must also integrate a variety of other aspects. The progress enabled by the semiconductor-based IT has been an undeniable development engine creating a myriad of new opportunities for society and the economy, but its backbone (the data center industry, networks, and devices) represents a significant environmental burden resulting in energy consumption. The continued expansion of the industry means that the energy use of data centers, networks, and end-user devices, and the associated emissions of greenhouse gases and other air pollutants, will continue to grow.[6] Although the exact energy intensity of data dissemination from a source to a number of users is still a matter of debate,[7,8] there is a general consensus that its energy footprint is prone to continue its rapid growth[7–11] to reach at least 22% of the global electricity supply by 2023.[10] To overcome these limitations, copper wires and low-k dielectrics are used on chips to reduce resistance and capacitance, and improve interconnect speed. There exist other possible physical approaches to improve heat dissipation, including cooling the chips and three-dimensional structures with vertical connections. But the underlying scaling issues and other physical problems are still outstanding challenges.

Recent potential solutions proposed to overcome the technological bottlenecks discussed above, have recognized optical interconnections via silicon (Si) photonic platforms (also know as Group IV photonics GFP) as the key paradigm to simultaneously tackle performance requirements and power challenges.[12–15] Indeed, the use of photons as the medium to detect, process, and transmit information will enable higher data rates and higher interconnection densities at lower system-level power dissipations.[16] In fact, optical interconnects have been progressively eliminating copper-based electrical ones in long-haul networks. The next natural step is to extend this trend to chip-to-chip and inter-chip communications. This is crucial to meet bandwidth demands, heat management, and energy efficiency across servers, boards, and on-chip. As compared to the traditional IRPD, the GFP materials bring serious advantages.

The best approach to integrate electronics and photonics remains an open issue. Some argue for the expedient option of putting electronics and photonics on separate chips. Others have shown that hybrid systems in the telecommunications industry, throughout the bonding of small group III-V devices to Si circuitry, is commercially viable to produce on chip-lasers, amplifiers, modulators, switches and detectors.[17] A third approach would be manufacturing totally monolithic

optoelectronic integrated circuits (OEICs).[18,19] The last approach is attractive because the process is seamless, and deals with homogeneous materials, since the group IV semiconductors are covalently bonded, and have similar chemical and physical properties. One specific benefit of mass-produced chips based on Silicon photonics, is that they offer a path to an extremely low, attojoules-per-bit energy cost for networks, and thus the potential to significantly reduce consumption of the energy that powers today's Internet society.[20]

Emerging applications require operation of photonic integrated circuits, and OEICs within an extremely wide spectral region, ranging from visible to terahertz. The characteristics of group IV elements and alloys give Group-IV Photonics the capability for addressing that broad spectrum, including the near-, mid- and far infrared. To take advantage of opportunities in new applications, scientists now must engineer GFP chips that operate at wavelengths longer than 1.55 μm. Many technologies can harmonize, synergistically, with both electronics, and photonics; including plasmonics, photonic crystals, nano-electromechanics, microfluidics, biological-material attachments, and microwave photonics. An opportunity exists to obtain new system functionalities by combining these technologies on one chip, in a 3-D, multilayer approach.

However, despites the advantages mentioned above, group IV semiconductors (mainly Si and Ge) suffer from a fundamental issue: poor light absorption and emission. Si has rather poor optical properties due to its indirect band gap, and limited light absorption especially in the near-infrared region (NIR) and beyond, thus limiting the efficiency of Si-based photodetectors light emitting devices. Consequently, the need to find a light active material, compatible with silicon technology, active in the range above 2 μm is of paramount significance to the CMOS industry. In general, there exists three approaches to transform an indirect material to a direct one: strain engineering, n-type doping, and alloying. It has been reported that the direct gap of Ge can be tuned with tensile-strain which leads to a slightly larger absorption edge near 1.6 μm.[21–23]

In addition to IT, the aforementioned challenges also limit the progress in the smaller but increasingly important sector of infrared- (IR-) based sensing and imaging. The latter is central in numerous applications such as night vision, building inspection, predictive inspection, maintenance of industrial equipment, environmental monitoring surveillance, automotive and maritime safety, and fire-fighting. In the military, IR imaging is used for thermal weapon sight as well as vehicle and portable vision. Although IR imaging is becoming prevalent, the high production cost has

been a major obstacle in the development of high-resolution devices. For instance, despite their importance in a variety of applications, short-wave IR (SWIR) imagers are currently out of the reach of mainstream IR technologies.[24–30] Traditionally, intrinsic photon infrared photodetectors were mainly based on semiconductor materials such as group IV-VI compounds (lead salts: PbS,[31] PbSe,[32] and PbTe[33]), group II-VI alloy (mercury cadmium telluride HgCdTe[34]), and group III-V compounds (InGaAs, InAsSb, InSb, and InGaSb).[35] However, this class of infrared photodetectors (IRPDs) is undermined by some disadvantages. This includes the high cost and small array size of these detectors translates to an overall cost of a megapixel SWIR sensor exceeding tens of thousands of dollars.[36] This is a major limitation that prevents the broad use of SWIR technologies. Additionally, the IV-VI compounds are known to suffer from poor mechanical properties as well as large permittivity, even though they are low-gap materials and are well studied in literature. In addition, the main motivation behind the numerous attempts to replace the II-VI compounds (HgCdTe) is to circumvent material-related limitations. Among them is the weak Hg–Te bond, which results in bulk, surface, and interface instabilities. Moreover, HgCdTe is known to have non-uniformity over large area, as well as high cost in growth and processing.[34] Finally, the III-V alloys can be monolithically integrated, yet the large lattice mismatch during heteroepitaxy of these compounds renders it an undesirable candidate for industry.[37]

To overcome the limitation imposed by Si and Ge indirect bandgap, this project will focus on developing Si-compatible light sources by exploiting the emerging group IV semiconductors. A possible candidate for such materials are Germanium-Silicon-Tin ternary ($Ge_{1-x-y}Si_xSn_y$ where x and y are respectively the Si and Sn atomic composition) and Germanium-Tin ($Ge_{1-y}Sn_y$ where y is the Sn composition) binary alloys. This provides more flexibility to independently engineer the bandgap and lattice parameter in a similar fashion to the more mature III-V semiconductors. Both theoretical modelling,[38–40] and experimental results[41–48] show that the electronic band structure of Ge can be tuned by varying the Sn composition. It is predicted that electron and hole effective masses of $Ge_{1-y}Sn_y$ decreases with an increasing Sn composition.[49] This has motivated the investigation of $Ge_{1-y}Sn_y$ as a next-generation semiconducting material for high mobility channel metal-oxide-semiconductor field effect transistors (MOSFETs) in the sub-7 nm technology nodes[50–52] and silicon-based photonic devices, *e.g.* infrared photodetectors,[53–58] and light-emitting devices.[59–63] However, the fact that SiGeSn semiconductors can be grown on Si wafers

is crucial to achieve scalable, cost-effective Si photonics. By tuning composition and strain in SiGeSn-based heterostructures and low-dimensional structures, we plan to implement light emitters and detectors targeting the technologically important SWIR range. This novel family of optoelectronic devices will benefit from the compatibility with complementary metal oxide semiconductor (CMOS) processing leading to a full exploitation of the current microelectronic and optoelectronic technologies thus allowing:

- Production in a high-volume Si wafer fab with repeatability, uniformity, and cost-effectiveness;
- Standard design flow making photonics design very similar to CMOS design with a library of elementary devices allowing the manipulation of light in the same way as electrical signals;
- Managing supply chain from wafers to final product including on-wafer testing for electrical and optical functionalities.

Furthermore, coupling light trapping schemes with the dimensionality of $Ge_{1-x-y}Si_xSn_y$ material can lead to an increase in light absorption efficiency in IRPDs. In fact, tuning the dimensionality of the material is another promising approach to increase its absorption efficiency. Conventional light trapping techniques relies on surface texturing and/or antireflection coating.[64–66] Whereas, nanowire photonics, an emerging topic, is gaining traction in the material science community due to a better control and understanding of the growth processes involved. It also allows the investigation of light generation, propagation, detection, amplification, and modulation.[67] Nonetheless, elucidating the fundamental electronic and optical properties of the material is an important task that will pave the road to better implement it in different contexts, and application. Specifically, analyzing the effect of strain and alloying on the electronic structure of GeSiSn will guide research for a more targeted integration of the material in photodetectors for instance.

The main objective of this thesis is to provide the foundation to implement material systems for Si-compatible light sources and photodetectors. This thesis focuses on band structure engineering in $Ge_{1-x-y}Si_xSn_y$ semiconductors. Knowledge of the bandgap energy of $Ge_{1-y}Sn_y$ alloys with different amounts of strain is of paramount importance to design future optoelectronic devices based on these emerging semiconductors. $Ge_{1-y}Sn_y/Ge_{1-x-y}Si_xSn_y$ heterostructures are also

investigated in both thin film and nanowire structures. This document is organized in seven chapters. In Chapter 2, a literature review is presented to describe the current state-of-the-art of the field. Chapter 3 outlines the basics of spectroscopic ellipsometry process, and gives a theoretical description for how to accurately evaluate the electronic structure of $Ge_{1-x-y}Si_xSn_y$ semiconductors. Likewise, the Mie- Lorentz scattering formalism will be developed to calculate light scattering and absorption efficiencies of group IV based nanowire structures. Chapter 4 elaborates on the evaluation of the unstrained and strained electronic structure of $Ge_{1-x-y}Si_xSn_y$ using the second nearest neighbors empirical tight binding approach. Chapter 5 shows that it is possible to confine electron and hole in a radial nanowire $Ge_{1-y}Sn_y/Ge_{1-x-y}Si_xSn_y$ heterostructure, by accurately tuning the geometric dimension of the structure and the doping concentration of carriers inside the core-shell nanowire structure. Chapter 6 discusses light scattering and absorption of group IV based core-shell nanowires. Finally, Chapter 7 ties these topics together with suggestions for future work.

CHAPTER 2 LITERATURE REVIEW

In 1982, $Ge_{1-y}Sn_y$ binary alloys have been mentioned for the first time in literature as a possible direct bandgap group IV semiconductor with unusually high carrier mobilities.[68] $Ge_{1-y}Sn_y$ has long been considered as a hypothetical alloy due to the low solid solubility of Sn in Ge.[69] Despite this limitation, early reports on the growth of monocrystalline Sn-rich alloys started emerging in early 1990s mainly based on solid-source molecular beam epitaxy (MBE).[70] However, the quality of the grown films was not good enough for device fabrication due to dislocation defect presence. Consequently, the interest in this family of semiconductors progressively faded away until late 2000's when the development of stable precursors enabled the growth of device-quality Sn-containing group IV semiconductors using Chemical Vapor Deposition (CVD). The revived interest in this material system has been motivated by the ability to control of the growth kinetics using CVD-based processes, which yield high-quality monocrystalline $Ge_{1-y}Sn_y$ binary and $Ge_{1-x-y}Si_xSn_y$ ternary alloys layers.[70] The availability of monocrystalline layers and heterostructures raised pressing needs to understand their fundamental properties and their behavior as a function of strain and composition. This led to a surge in experimental and theoretical studies of the electronic and optical properties of these materials. In the following, the current understanding of the electronic structure and optical properties for binary and ternary alloys are presented.

2.1 Binary semiconductors $Ge_{1-y}Sn_y$

$Ge_{1-y}Sn_y$ semiconductors have been attracting a great interest in recent years as they provide a reliable path to achieve Si-compatible optoelectronics. Diamond cubic tin (Sn in its alpha phase, α-Sn, or grey-tin) is a semimetal with a conduction band minimum at the Γ point sitting 0.41 eV below the valence band. By alloying Sn and Ge, the conduction band extrema at both L and Γ valleys are predicted to decrease in energy with increasing Sn composition. However, the Γ valley is predicted to decrease more rapidly than the L valley as shown in Figure 2-1. The basic properties of $Ge_{1-y}Sn_y$ have been evaluated using a variety of theoretical approaches. This includes empirical pseudopotential method,[38,49,71,72] the $k.p$ method,[73] tight-binding,[40,74] and density functional theory (DFT)[43,75–80] in virtual crystal approximation (VCA). $Ge_{1-y}Sn_y$ is predicted

to undergo an indirect-to-direct transition around 6% Sn with a direct bandgap energy of 0.66 eV. In addition to theoretical studies, experimental investigations of the optical and electronic properties of $Ge_{1-y}Sn_y$ have also surged in recent years as a result of the progress in the epitaxial growth of Sn-rich films and heterostructures.[41,42,45,46,81–87] It is, however, important to note that strong discrepancies are found when comparing different studies currently available in literature. This mainly concerns the large bowing parameter of the direct band gap, the critical composition at which the direct gap is achieved, the dependence of the energy gaps on the atomic distribution, and the band offsets in the alloy.

2.1.1 Bowing parameter and critical composition

First, a broad range of values has been reported for the optical band gap bowing parameter, *b*. First principle calculations gave *b* of 2.06,[88] 2.75,[43] 2.49,[78] and 1.90,[89] while experimental works based on the spectroscopic techniques generally give a smaller optical band gap bowing of 0.94,[90] 0.25,[91] -0.4,[92] and 0.30.[93] The discrepancy between the band structure calculations and the experimental results has been attributed to the bowing of the bandgap produced by local distortions in the bond lengths and bond angles of the crystal. With the bowing effect, the composition-dependent bandgap energy of alloys can be expressed as a second order approximation

$$E_g\left(Ge_{1-y}Sn_y\right) = yE_g(Sn) + (1-y)E_g(Ge) + by(1-y)$$

where $E_g(Sn)$ and $E_g(Sn)$ are the band gap energy for bulk Sn and Ge, respectively.

Second, the critical composition (y_c) at which the band structure transits from indirect to direct gap is still not accurately established for relaxed and strained $Ge_{1-y}Sn_y$ alloys. Low et *al*. reported a critical composition of 11% Sn using Empirical Pseudopotential Method (EPM) as shown in Figure 2-1. $E_{g,\mathrm{L}}$ and $E_{g,\Gamma}$ are the bandgap energies at the L- and Γ-symmetry direction, respectively. Similar to Ge, $Ge_{0.95}Sn_{0.05}$ [Figure 2-1(a)] is an indirect bandgap material, as the conduction band minimum (CBM) is located at the L-valley. With increasing *x*, both $E_{g,\mathrm{L}}$ and $E_{g,\Gamma}$ shrink, but the latter shrinks faster. Thus, $Ge_{1-y}Sn_y$ becomes a direct bandgap material when *y* exceeds a critical y_c = 0.11, as shown in Figure 2-1(c).[49] There are several theoretical studies predicting Sn concentrations between 6.3 at.% and >20 at.% needed for the indirect-to-direct band gap transition.[78,94,95] For

relaxed $Ge_{1-y}Sn_y$ layers, except for some isolated cases of extreme values of 1.6%[80] or 17%[78], most of the available data from both experimental [45,86] and theoretical [38,39,43, 96] studies remain in a lower range of 4.5-8 at.%. Whereas research for strained materials consistently shows higher values for y_c of over 8%, 10% , and between 10-13%.[39,81,85] This behavior is expected and has been studied theoretically[39] and experimentally in [45].

Thus, establishing accurately the critical composition of $Ge_{1-y}Sn_y$ constitutes a necessary and important step to understand the material system and evaluate its relevance for photonic and optoelectronic applications. This necessitates an accurate calculation of the electronic structure. Additionally, as already mentioned above, strain can play a fundamental role in shaping the band structure and must therefore be incorporated in the estimation the critical composition.

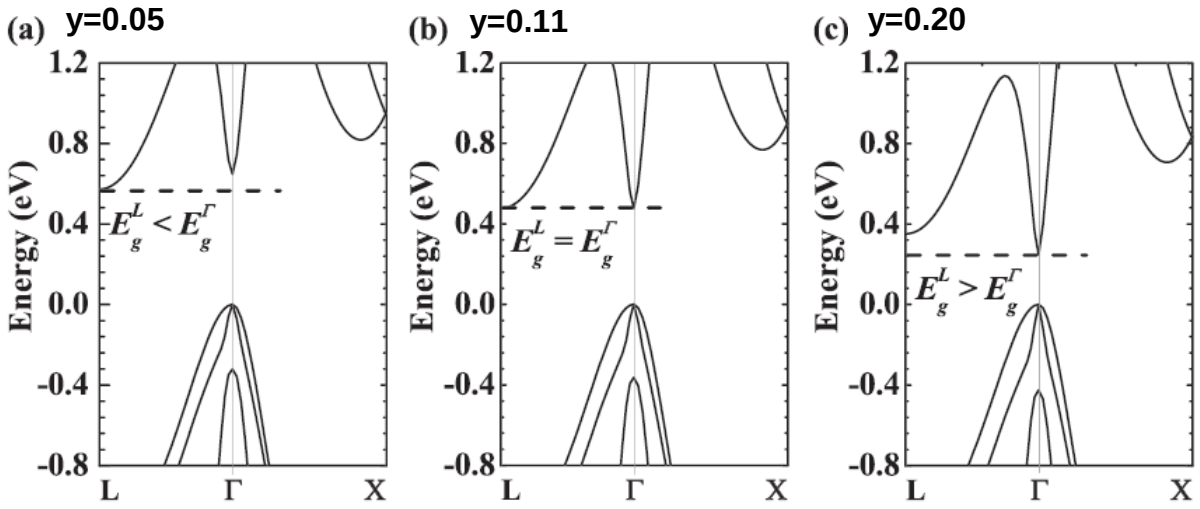

Figure 2-1: Electronic band structures of $Ge_{1-y}Sn_y$ for (a) y = 0.05, (b) y = 0.11, and (c) y = 0.20, showing the transition from indirect [panel (a)] to direct bandgap [panel (c)] of $Ge_{1-y}Sn_y$. Panel (b) illustrates the critical composition of 0.11, where the bandgap energies at L- and Γ-valleys are equal. The dashed line indicates the conduction band minimum (CBM) of $Ge_{1-y}Sn_y$. (After Ref.[49], reprinted with permission)

2.1.2 Strain effect on electronic structure

Expectedly, strain has significant effect on the band structure and optoelectronic properties of semiconductors. For instance, as shown in Figure 2-2, by applying biaxial tensile strain, both the direct and indirect band gaps shrink. However, the direct gap shrinks faster than the indirect band gap, thus the difference between these two valleys decreases. Consequently, with enough strain,

Ge, for example, can transform into a direct band gap material. The critical tensile strain has been predicted to be between 1.6% and 1.9%.[97,98] The approach relying on strain alone to induce direct gap in Ge necessitates the use of non-conventional fabrication and processing techniques such as suspended Ge membranes to achieve the large amount of tensile strain needed for indirect to direct band gap transition.[99,100] The observed effect of strain also emerges as an interesting strategy to achieve direct band GeSn semiconductors. Recent advances in non-equilibrium growth technique for GeSn have enabled the growth of GeSn semiconductors with alloy substitutional Sn content exceeding 16%.[101] Therefore, a combination of strain and Sn alloying, i.e., strained GeSn alloys may be able to relax the requirements on both the amount of Sn as well as the tensile strain needed to obtain a direct band gap.

In principle, biaxial tensile strain can be achieved by three different methods: thermal mismatch, mechanical stress, and lattice mismatch. First, thermal mismatch relies on the fact that thermal expansion coefficient for Si (2.6×10^{-6} °C^{-1}) is half of the coefficient for $Ge_{0.955}Sn_{0.045}$ (5.8×10^{-6} °C^{-1}) which can generate a measured thermal strain of +0.34%.[102] Second, external stress can be applied to designed GeSn Micro-Electro-Mechanical Systems (MEMS) structures.[103] Four times larger strain can be achieved using this approach, compared to the maximum strain using the first method. Third, by epitaxially growing $Ge_{1-y}Sn_y$ layers on a larger parameter lattice. This approach is yet to be demonstrated. Note that the growth on Ge substrates yields compressively strained GeSn layers, which require a much higher amount of Sn to reach a direct band gap.[39,81,85]

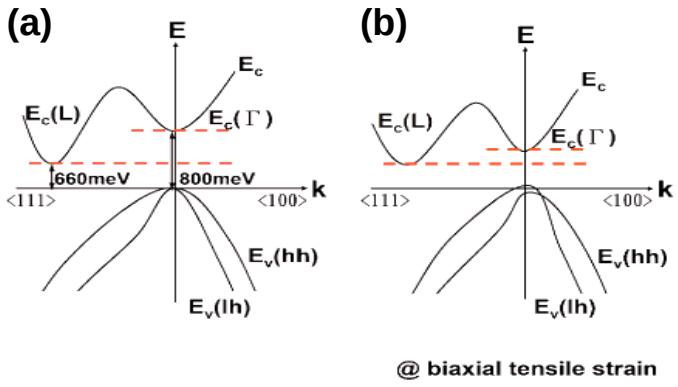

Figure 2-2: **(a)** The band structure of n-type Ge, and **(b)** a schematic diagram of the band gap reduction in L and Γ valleys with biaxial strain. (After Ref.[97], reprinted with permission)

2.1.3 Band offsets

Little information can be found in literature concerning the band offset in $Ge_{1-y}Sn_y$, due to the difficulty in establishing their values, as has been properly discussed in Ref.[43]. The authors report the natural valance band maximum (VBM) offset between Ge and Sn to be 0.91 eV, whereas the conduction band maximum (CBM) offset to be -0.41 eV. Additionally, the natural VBM and CBM (direct band) offsets between Ge and Sn has been calculated to be equal to 0.55 eV and -0.7 eV using DFT approach based on the Tran and Blaha MBJLDA functionals.[104] Furthermore, H-S. Lan et *al.*,[105] analyzed theoretically, using the nonlocal empirical pseudopotential method, the band structure of a p-type Ge cap/fully strained $Ge_{1-y}Sn_y$ quantum well/ Ge (001) where they reported a calculated valance band offset ΔE_v of ~80 meV in $Ge_{0.95}Sn_{0.05}$ by using the model solid theory (MST)[106]. Their estimation was found to be within the reported measurement accuracy range of ±50 meV for y<0.08.[107] Establishing an accurate estimation of the natural band offset is vital from an application point of view. For instance, in heterostructures such as multi-quantum wells, the relative band positions in adjacent layers determine the character of carriers' confinement, which in turn determines the type of the quantum well. We will address this issue in Chapter 5 by using the MST developed by Van de Walle[106] under the framework of the second nearest neighbors tight binding theory.

2.1.4 Enhanced light absorption of GeSn

The tunability of the GeSn band structure through Sn composition is an important advantage to implement optoelectronic devices operating in the NIR and MIR wavelength ranges. However, the use, for instance, of group IV photodetectors is limited by their relatively small range of efficient light absorption. Figure 2-3 shows the room-temperature absorption coefficient (α) versus light wavelength (λ) of Ge, and two GeSn samples with 2% and 4.6% Sn composition. This figure is replotted from Ref.[108] where V. D'Costa *et al.* measured room-temperature absorption coefficients of $Ge_{1-y}Sn_y$ alloys with various Sn contents using spectroscopic ellipsometry. All the $Ge_{1-y}Sn_y$ films were fully compressively strained to the Ge (100) substrates. It can be observed that an Sn composition of around 4.2% extends the absorption edge of $Ge_{1-y}Sn_y$ into MIR region, and the curves shift towards longer wavelengths with increasingly larger Sn composition.

Ge is almost transparent to photons with λ beyond 1.55 μm. The drastic decrease in the absorption coefficient in Ge, near λ = 1.55 μm, can be explained by the direct bandgap (near the Γ

symmetry point, denoted as $E_{g,\Gamma}$) of 0.8 eV. It can be observed that the higher the Sn composition, the more extended the absorption edge into the MIR region, will become. In other words, the absorption coefficient curves shift towards longer wavelength with increasingly larger Sn composition. This makes $Ge_{1-y}Sn_y$ a very promising group IV semiconductor for NIR and MIR photodetectors where adjusting the Sn composition can control the absorption properties. This is will be investigated in detail in Chapter 6.

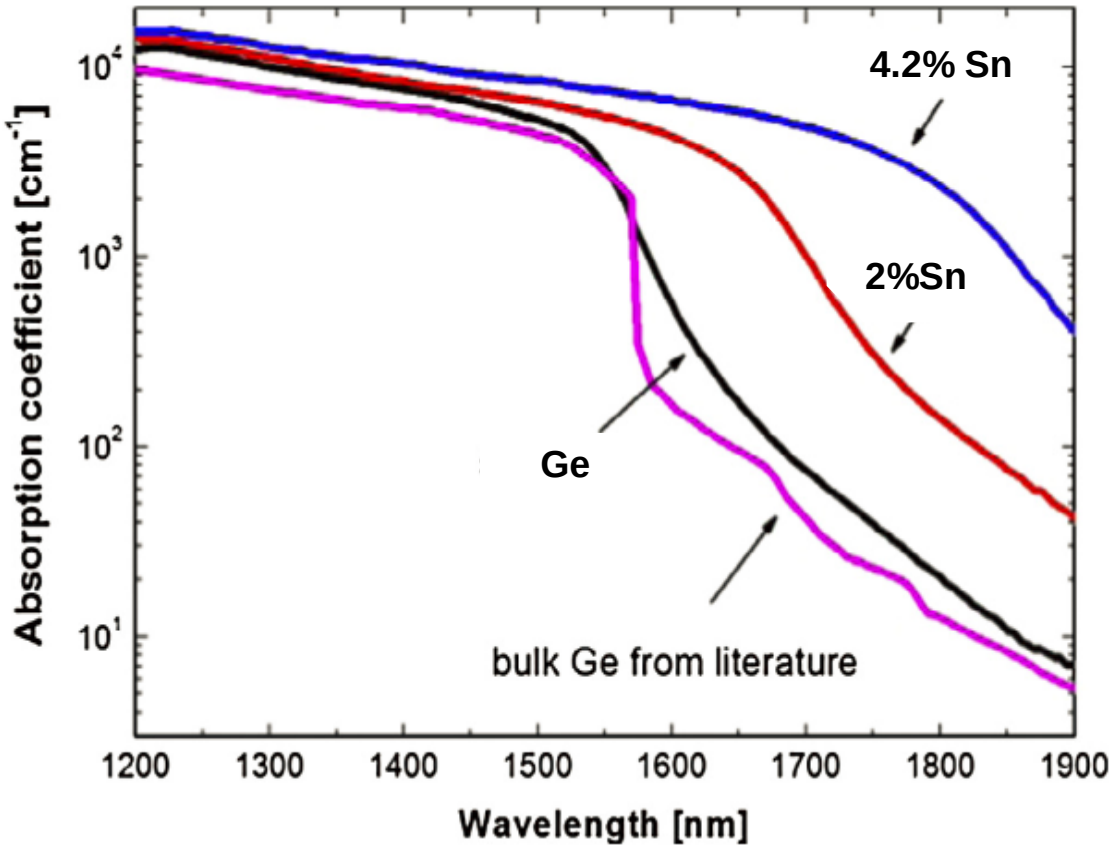

Figure 2-3: Wavelength dependence of the absorption coefficient in cm^{-1} for several semiconductors materials. (After Ref.[109], reprinted with permission)

2.2 $Ge_{1-x-y}Si_xSn_y$ ternary semiconductors

Modern semiconductor technology requires epitaxial layers with a precisely prescribed band gap and lattice constant. This dual requirement, which cannot be accommodated via "one-dimensional" binary A_yB_{1-y} (e.g. $Ge_{1-y}Sn_y$) or pseudo-binary $A_xB_{1-x}C$ alloys, has motivated the quest for "two-

dimensional" ternary ($A_xB_yC_{1-x-y}$), pseudo-ternary ($A_xB_yC_{1-x-y}D$), or quaternary ($A_xB_{1-x}C_yD_{1-y}$) materials whose band gaps and lattice constants can be tuned independently. Ternary group-IV alloys are the simplest semiconductors with a two-dimensional compositional space. Aside for $Ge_{1-x-y}Si_xSn_y$, the only other ternary group-IV semiconductors are those containing carbon, but these can hardly be achieved experimentally due to the very small amounts of carbon that can be randomly incorporated in Si and Ge lattices.[110] In this thesis, the main focus is on the $Ge_{1-x-y}Si_xSn_y$ system. Due to their compatibility with Si substrates, $Ge_{1-x-y}Si_xSn_y$ alloys can act as buffer layers to control strain of device structures on Si substrates. Another special feature of $Ge_{1-x-y}Si_xSn_y$ ternary alloys is the independent manipulation of both lattice constant and band structure. In other words, $Ge_{1-x-y}Si_xSn_y$ alloys have tunable bandgap energy at a fixed lattice constant. D'Costa et. *al*. have grown $Ge_{1-x-y}Si_xSn_y$ alloys by reduced-pressure chemical vapor deposition (RP-CVD), and they fixed the ratio of Si:Sn at 4:1 so that the $Ge_{1-x-y}Si_xSn_y$ alloys were lattice-matched to Ge.[111] Using variable-angle spectroscopic ellipsometer, they observed an increased direct bandgap with increasing Si composition. Other optical transitions were studied in the same way.[112–114] By selecting the composition, the $Ge_{1-x-y}Si_xSn_y$ barrier layer can have the desired lattice constant to strain or match the following Ge or $Ge_{1-y}Sn_y$ QW layer, while keeping larger bandgap energy to confine carriers inside the active Ge or $Ge_{1-y}Sn_y$ layer. For instance, Chang *et. al*. proposed a tensile-strained Ge laser based on a heavily n-type doped $Ge/Si_{0.2}Ge_{0.7}Sn_{0.1}$ MQW structure.[115] Strain-free $Ge_{0.94}Sn_{0.06}/Si_{0.15}Ge_{0.75}Sn_{0.1}$ double heterostructures[116] and strain-balanced $Ge_{0.84}Sn_{0.16}/Si_{0.09}Ge_{0.8}Sn_{0.11}$ MQW lasers[117] were also proposed, and simulated for optical gain as well. Type-I band offset alignment was assumed in these simulations. These simulations show promising results, but, due to limited experimental results, the material properties, such as bandgap energy and effective mass, used in the calculation are mostly based on theoretical predictions, which are fraught with large uncertainties. Moreover, LED device based on $Ge_{0.915}Sn_{0.085}/Ge_{0.8}Si_{0.1}Sn_{0.1}$ MQW were fabricated, as schematically shown in Figure 2-4(a) and yielded an emission peak position of 0.55 eV measured at 300 °C as shown in Figure 2-4(b). They also showed a great enhancement of the peak current density up to 130 A/cm^2 compared to the GeSn homojunction.[118,119]

The accurate knowledge of the dependence of the band gap energy *vs.* composition and strain, as well as effectives masses, is necessary to the success of structure prediction and optimization. In earlier studies, Moontragoon et *al*. have used the charge self-consistent pseudopotential Xα

method[78], whereas Ventura et *al*. used tight-binding approach coupled with VCA[120] to calculate

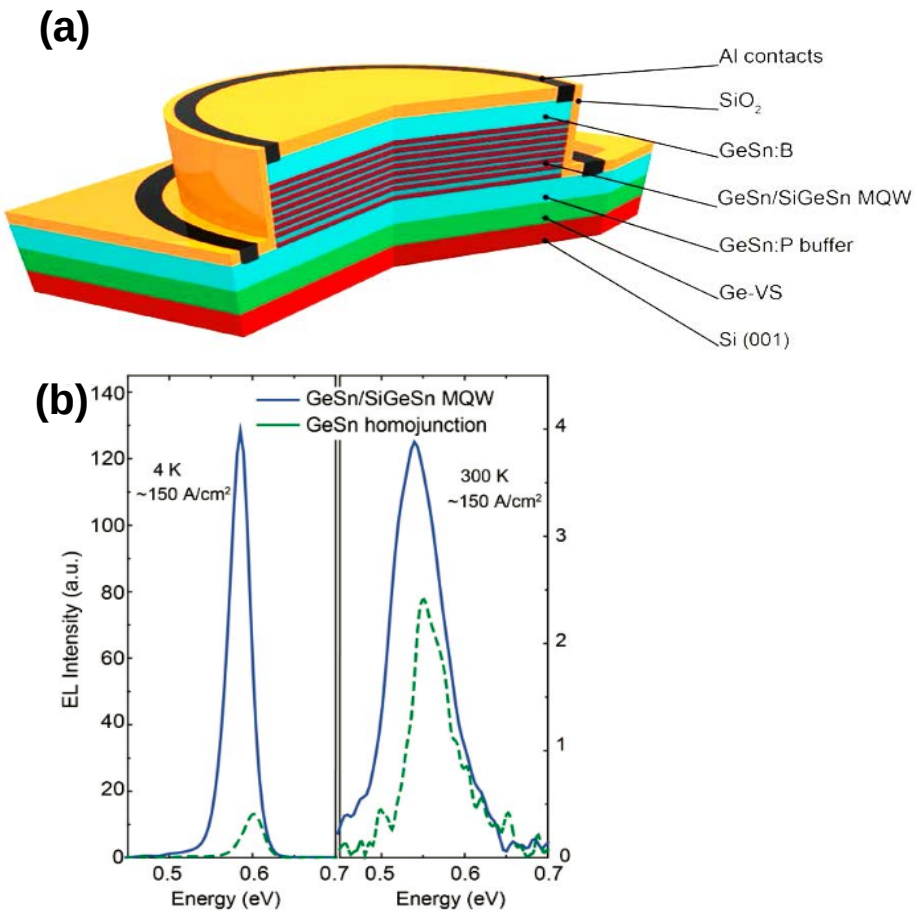

Figure 2-4: **(a)** Schematic of GeSn/GeSiSn MQW LED. **(b)** Emission spectra at 4K and 300K of d=100 µm GeSn/GeSiSn MQW (blue) and homojunction (dashed green) LEDs.

the band structure of $Ge_{1-x-y}Si_xSn_y$. The experimental characterization of the electronic structure of $Ge_{1-x-y}Si_xSn_y$ alloys have been studied using optical and electro-optical methods. For instance, in Figure 2-5(a), Xu et *al*. measured the photoluminescence spectra of multiple $Ge_{1-x-y}Si_xSn_y$ samples grown on a Si substrate with a Sn concentration higher than the Si one ($y>x$). The direct gap emission peak E_0 was measured and was estimated to follow a linear expression of the form $E_0(x,y) = (0.785 \pm 0.013) + (2.41 \pm 0.11)x - (4.06 \pm 0.19)y\ [eV]$.

Additionally, photoreflectance was used to measure the direct gap energy of unstrained $Ge_{1-x-y}Si_xSn_y$ samples. Figure 2-5 shows that increasing Si composition for a fixed Sn/Ge ratio of 0.069 induces a blue shift for band gap.[121] Furthermore, the strong direct transitions were investigated using spectroscopic ellipsometry.[113,114,122] The lowest direct band gap was measured using spectroscopic ellipsometry,[113] photocurrent experiments in diode structures,[123,124] photoreflectance,[121] and photoluminescence (PL).[125] Additionally, the fundamental band gap was determined using photoluminescence spectroscopy for Si and Sn compositions varying respectively from 2.4 at.% to 4.3 at.% and from 5 at.% to 8.1 at.%.[126]

Finally, it is important to note that establishing an accurate, non-computationally expensive methodology for studying the electronic structure and the optical properties of $Ge_{1-x-y}Si_xSn_y$ material system will lay the groundwork to engineer an Si-compatible direct gap semiconductor that is efficient by tuning the Sn and Si composition and the strain independently. An additional degree of freedom to tune and enhance and optoelectronic properties is size and morphology as it is addressed is this project by using nanowire heterostructures. The second nearest neighbour tight binding approach will be our method to evaluate the electronic structure of relaxed and strained $Ge_{1-x-y}Si_xSn_y$ to establish the direct-to-indirect critical composition. Besides, the bowing parameter as well as the band-offset will be extracted and compared to available literature data. Whereas, Mie-Lorentz Scattering formalism will be used to quantify light absorption based on experimental parameters extracted from ellipsometry studies.

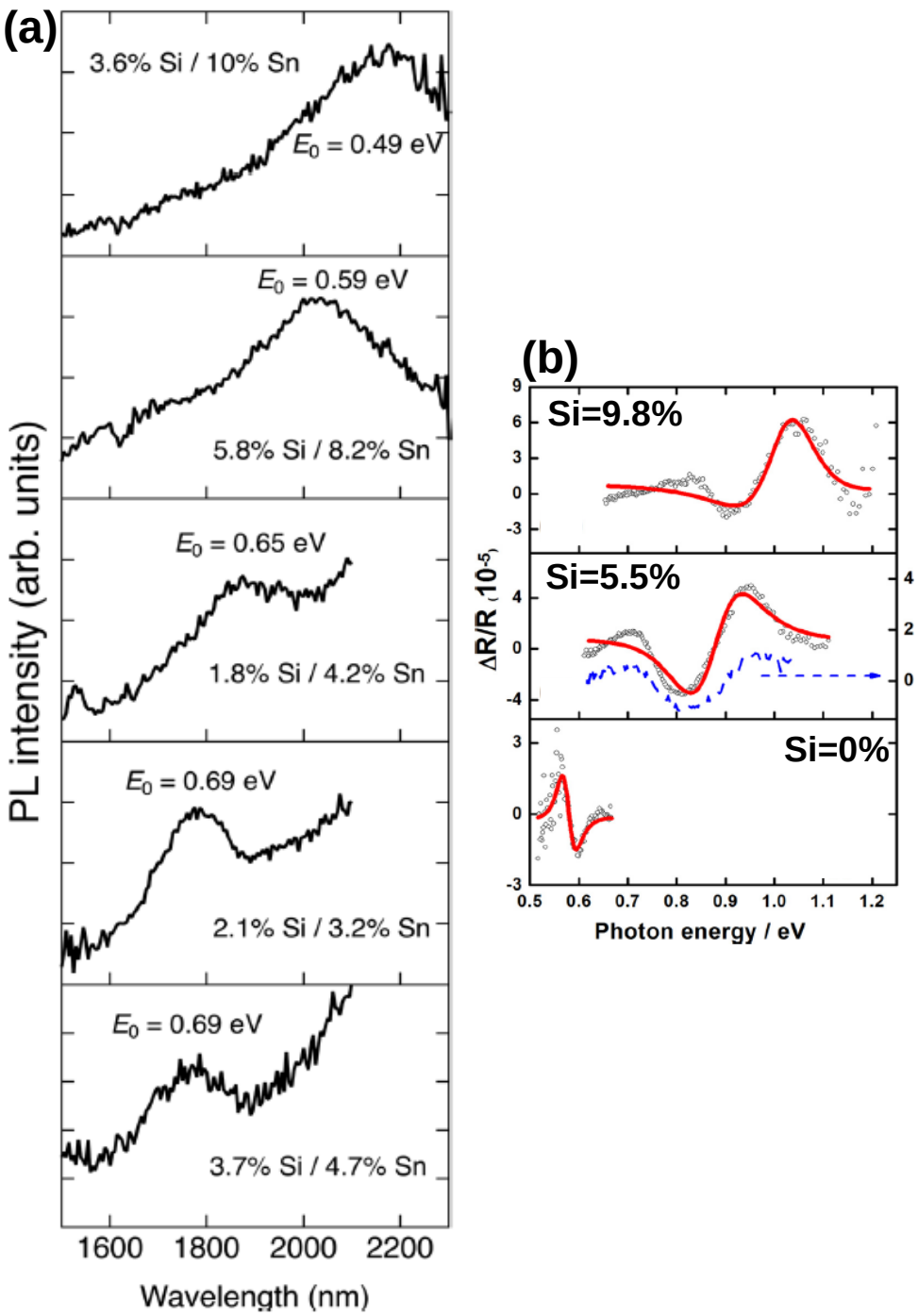

Figure 2-5: **(a)** Room-temperature photoluminescence of $Ge_{1-x-y}Si_xSn_y$/Si samples with y>x. All samples display emission peaks at longer wavelengths than the pure Ge emission at 1550 nm. (After Ref.[125], reprinted with permission) and **(b)** room-temperature photoreflectance spectra of unstrained $Ge_{1-x-y}Si_xSn_y$ sample with fixed Sn/Ge ratio about 0.069, but different Si concentrations of 0%, 5,5% and 9.8 %. (After Ref.[121], reprinted with permission)

CHAPTER 3 METHODOLOGY

The evaluation of the electronic band structure of $Ge_{1-x-y}Si_xSn_y$ is crucial to establish a more accurate understanding of the optical and electronic properties of this emerging class of semiconductors. To this end, we have chosen to use the second nearest neighbor empirical tight binding method (ETBM) to calculate the band structure. This was motivated by a couple of reasons. First, using semi-empirical approaches is computationally less expensive than full first-principle theoretical techniques, such as Density Functional Theory (DFT). Second, ETBM allows for an accurate evaluation of the energy band gaps and effective masses at room temperature which are important for device design and performance optimization. It is also noteworthy that the introduction of empirical parameters allows a better control of the theoretical simulations. Moreover, we also investigated light absorption and scattering inside NW structures based on the Mie-Lorentz scattering formalism to elucidate the light-structure interaction. However, to determine the absorption of light by nanostructure using the Mie-Lorentz approach, it is crucial to measure the optical constant of the material in question. One of the quickest and most accurate technique for that, is spectroscopic ellipsometry (SE).

This chapter is divided into a theoretical section and an experimental section. In the former, we outline the theory behind ETBM and the Mie-Lorentz scattering approach. Next, the experimental section describes the spectroscopic ellipsometry on how it is used to extract the optical properties of the measured samples. We will provide details on the experimental setup and on data analysis to extract the dielectric constant or the complex refractive index. Finally, we will present the steps undertaken to measure the $Ge_{1-x-y}Si_xSn_y$ sample and evaluate the optical properties from the optical model.

3.1 Theoretical Methods

3.1.1 Electronic structure calculations

In developing the tight binding approach for electrons in a solid, we start from the assumption that electrons are tightly bound to nuclei. Bringing atoms closer together, the separation of the atoms becomes comparable to the lattice parameter in solid leading to the overlap of their wave functions.

Thus, it is reasonable to approximate the electrons wave functions by linear combinations of the atomic wave functions.[127] The justification of this approach, known as the linear combination of atomic orbitals (LCAO), resides in the fact that in a covalently bonded semiconductor, such as Ge or Si, one can distinguish between two kind of electronic states: free electrons in the conduction band and localized electrons in atomic-like states in the valence band, thus their wave functions can be approximated by bonding orbitals found in molecules. To briefly formulate the tight binding approach, the wave function can be expressed as an LCAO in terms of Bloch functions ψ_α: $|\Psi\rangle = \sum_{\alpha,\boldsymbol{R}} A_{\alpha,\boldsymbol{R}}\, \psi_\alpha(\boldsymbol{r}-\boldsymbol{R})$ where $\boldsymbol{R}$ and α denotes the position of the atom and the orbital, respectively. The Schrödinger equation can thus be written as:

$$\sum_{\alpha,\boldsymbol{R}} A_{\alpha,\boldsymbol{R}} \left[H_{\alpha\boldsymbol{R},\alpha'\boldsymbol{R}'} - ES_{\alpha\boldsymbol{R},\alpha'\boldsymbol{R}'}\right] = 0; \qquad (3\text{-}1)$$

$$H_{\alpha\boldsymbol{R},\alpha'\boldsymbol{R}'} = \langle \alpha, \boldsymbol{R}|H|\alpha', \boldsymbol{R}'\rangle;\ S_{\alpha,\alpha'}(\boldsymbol{R}-\boldsymbol{R}') = \langle \alpha, \boldsymbol{R}|\alpha', \boldsymbol{R}'\rangle$$

where E is the energy eigenvalue, $H_{\alpha\boldsymbol{R},\alpha'\boldsymbol{R}'}$ is the Hamiltonian matrix element and $S_{\alpha\boldsymbol{R},\alpha'\boldsymbol{R}'}$ is the overlap matrix between the atomic-like orbitals, also called hopping integral. To solve the secular equation, the Hamiltonian matrix elements given in (3-1) need to be evaluated beforehand. There is a multitude of methods that can be followed to find these matrix elements. The simplicity of the first nearest neighbor sp^3s^* (1NN-sp^3s^*), introduced by Vogl et *al.*,[128] resides in the possibility to transform the problem of finding the band structure to a problem of numerical optimization, where the number of parameters evolves with the TB method. For instance, for elemental diamond-like group IV semiconductors, the number of optimization parameters is only eight. However, for the 1NN-$sp^3s^*d^5$, introduced by Jancu et *al.*,[129] the number of parameters reaches nineteen. Thus, a compromise needs to be made between the computational cost (i.e., the numbers of parameters to optimize) and the accuracy of the method. Note that the first nearest neighbor sp^3s^* method produces anomalous effective mass along the X-symmetry points explained by the isotropic interaction between the fictive s^* state and the p state. A possible solution to overcome this issue is to include the second nearest neighbors.[130]

Firstly, an orthogonal minimal basis set was considered, i.e. one *s* state and three *p* states plus an exited state with s symmetry (s*). Such sp^3s^* parameterization can be implemented to find the electronic structure. The addition of the s* state permits the adjustment of the lowest conduction band near X.[128] We used the same notation as in Slater and Köster[130] in order to formulate the bulk Hamiltonian. Here the diamond crystal structure of Si, Ge and α-Sn are treated as zinc-blend structure where the anions and cations are identical. The anion positions are $\boldsymbol{R}_i$, whereas the cation positions are $\boldsymbol{R}_i + \boldsymbol{v}_i$ with $v_i = a_L/4\,(1,1,1)$, with a_L being the lattice constant. The Hamiltonian Matrix element $H_{\alpha\boldsymbol{R},\alpha'\boldsymbol{R}'}$ is presented below where we used three onsite energies, $E_{s,\alpha}, E_{p,\alpha}, E_{s^*,\alpha}$ with $\big(\alpha = a(anion), c(cation)\big)$, five hopping integrals for the 1NN-sp^3s^*. The 20×20 second neighbor Hamiltonian matrix elements for diamond like structures are given in terms of five transfer energy integrals involving nearest neighbors, i.e. $V_{ss}, V_{sx}, V_{xx}, V_{xy}$ and V_{s^*p} and ten transfer energy integrals involving second neighbors, i.e. $V_{ss}(110), V_{s^*s^*}(110), V_{sx}(110), V_{sx}(011)$, $V_{s^*x}(110), V_{s^*x}(011), V_{xx}(110), V_{xx}(011)$, $V_{xy}(110)$ and $V_{xy}(011)$. If only the contribution from the nearest neighbors is considered, the obtained Hamiltonian matrix should be composed of four block matrix elements as given in equation (3-2) where the diagonal 5×5 block matrix $[H_{aa}]$ is the same as $[H_{cc}]$ since the anion and the cation are the same in the considered system. The off-diagonal block $[H_{ac}]$, which represents the coupling between the anion and cation states, is a 5×5 dense matrix. The empirical sp^3s^* tight-binding matrices including only the nearest neighbors' interactions are already defined in Ref.[49]. Nevertheless, for the second nearest neighbors, new matrix elements must be added to incorporate the interaction between the second nearest neighbors, which will add new elements in the Hamiltonian below. The spin-orbit interaction, included in ETB model[131] couples the parallel and anti-parallel spin states located on the same atom, but not the orbitals located on neighboring atoms. Therefore, spin-orbit coupling not only adds off-diagonal elements to the diagonal same spin blocs $[H_{aa}]$ and $[H_{cc}]$, but also adds matrix elements between opposite spin orbitals located at the same atom. Without spin-orbit coupling, the up and down spin blocs in the tight binding Hamiltonian are:

$$\boldsymbol{H_{NO-Spin}} = \begin{bmatrix} \begin{bmatrix} [H_{a\uparrow a\uparrow}] & \\ & [H_{a\downarrow a\downarrow}] \end{bmatrix} & \begin{bmatrix} [H_{a\uparrow c\uparrow}] & \\ & [H_{a\downarrow c\downarrow}] \end{bmatrix} \\ \begin{bmatrix} [H_{c\uparrow a\uparrow}] & \\ & [H_{c\downarrow a\downarrow}] \end{bmatrix} & \begin{bmatrix} [H_{c\uparrow c\uparrow}] & \\ & [H_{c\downarrow c\downarrow}] \end{bmatrix} \end{bmatrix} \tag{3-2}$$

The Hamiltonian of the spin-orbit has the following structure:

$$\boldsymbol{H_{SO}} = \begin{bmatrix} \begin{bmatrix} H_{SO}\uparrow\uparrow & H_{SO}\uparrow\downarrow \\ H_{SO}\downarrow\uparrow & H_{SO}\downarrow\downarrow \end{bmatrix} & \\ & \begin{bmatrix} H_{SO}\uparrow\uparrow & H_{SO}\uparrow\downarrow \\ H_{SO}\downarrow\uparrow & H_{SO}\downarrow\downarrow \end{bmatrix} \end{bmatrix} \tag{3-3}$$

The various blocs of the spin-orbit Hamiltonian are described in Ref.[132]. If the contributions of the same atom are considered, the only non-zero matrix elements are:

$$\begin{aligned} \langle p_x,\uparrow | H_{SO} | p_y,\uparrow \rangle &= -i\delta \\ \langle p_x,\downarrow | H_{SO} | p_y,\downarrow \rangle &= i\delta \\ \langle p_z,\uparrow | H_{SO} | p_x,\downarrow \rangle &= -\delta \\ \langle p_z,\downarrow | H_{SO} | p_x,\uparrow \rangle &= \delta \\ \langle p_y,\uparrow | H_{SO} | p_z,\downarrow \rangle &= -i\delta \\ \langle p_y,\downarrow | H_{SO} | p_z,\uparrow \rangle &= -i\delta \end{aligned} \tag{3-4}$$

and their complex conjugates. $\delta = \Delta_0/3$ is the renormalized atomic spin-orbit splitting.[133,134] The introduction of the spin-orbit interaction in the sp^3s^* model yields, for a zinc-blende structure, a 20×20 total Hamiltonian matrix, which must be diagonalized for each $\boldsymbol{k}$ vector to obtain the bulk band structure. The total Hamiltonian is defined by: $\boldsymbol{H_{Tot} = H_{NO-Spin} + H_{SO}}$

3.1.2 Mie-Lorentz scattering formalism

The calculation of the optical absorption of the core-shell nanowires are performed within the framework of the Lorentz-Mie scattering formalism[135] adapted to a cylindrical geometry. The core-shell nanowire (CSNW) is modeled as an infinitely long coaxial cylinder, as shown in Figure 3-1 (the diameter is at least 10 times smaller than the length), which has been extensively used to

analyze light absorption in various NWs.[136–139] The CSNW has a total radius of $t + R_c$, where t and R_c are the shell thickness and the core radius, respectively. The NW, placed in vacuum, is illuminated by a non-polarized incident plane wave, the wavevector of which, $\boldsymbol{k}_{in}$, is perpendicular to the NW axis, as depicted in Figure 3-1(a). Furthermore, the wavelength range was fixed to 300-1100 nm covering the visible and NIR range of the solar spectrum (AM1.5G).[140] The complex refractive index of $Ge_{1-y}Sn_y$ and $Ge_{1-x-y}Si_xSn_y$ ternary alloys were extracted from spectroscopic ellipsometry measurements. Sn rich GeSn and GeSiSn will be studied to quantify light absorption and scattering efficiencies. The NW far-field optical response is characterized by two dimensionless quantities: the absorption efficiency Q_{abs} and the scattering efficiency Q_{sca} as shown below:

$$Q_{abs(scat)} = \frac{Q_{abs(sca)}^{TM} + Q_{abs(sca)}^{TE}}{2} \tag{3-5}$$

where $Q_{abs(sca)}^{TE}$ and $Q_{abs(sca)}^{TM}$ are the absorption (scattering) efficiencies for transverse electrical TE (electric field is perpendicular to the NW axis) and transverse magnetic TM (electric field is parallel to the NW axis) polarization, respectively. These quantities correspond respectively to the ratio of the absorption (C_{abs}) and scattering (C_{sca}) cross section to the geometrical cross section C_{geo} of the NW.[135] The cross section is defined as a fictive area around the illuminated object.

As soon as a light beam hits this area, the interaction occurs. Let us consider an ideal case where the absorption cross section C_{abs} of a hypothetical, perfectly absorbing black body is always equal to the geometrical area A of the object, the absorption efficiency is therefore always equal to 1. Now, for a system that is an imperfect absorber, the absorption efficiency Q_{abs} is between 0 and 1 within the limits of geometrical optics. However, when a structure is smaller than the illuminating wavelength λ, such as the case for the studied NWs (where the diameters are typically below 200 nm), the absorption efficiencies Q_{abs} can exceed unity.[135] This can be interpreted by higher absorption cross section C_{abs} as compared to the geometrical cross section C_{geo}. In other words, the NW can collect light from an area much bigger than its geometrical area A.[136,141–143]

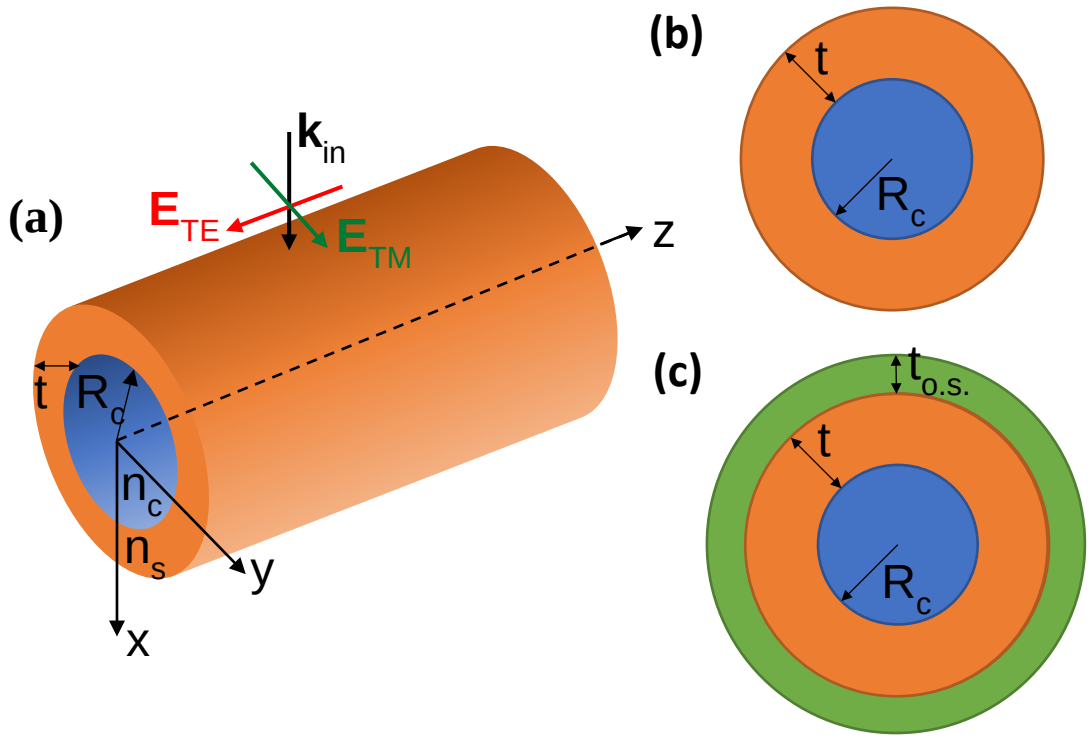

Figure 3-1: **(a)** Schematic of the analytical solution of light interaction with an infinite cylindrical core-shell nanowire. The core and the shell are both formed with group IV semiconductor binary or ternary alloy having respectively different complex refractive index n_c and n_s. Cross-section of a cylindrical **(b)** CSNW system with a core radius R_c and a shell thickness t and a cylindrical **(c)** core-multishell nanowire system having a core radius R_c, an inner-shell of thickness t and an outer-shell thickness $t_{o.s.}$ with the respective complex refractive indices $n_c, n_{s.}$ and $n_{o.s.}$. The material composing the outer-shell in panel **(c)** will either be a non-absorbing dielectric or GeSiSn semiconductor.

In the following, the key equations under the Lorenz-Mie framework are presented allowing the quantification of light absorption by CSNW structures. Under unpolarized illumination, the NW far-field optical response is the average of the absorption efficiencies between TE and TM modes and it is given by Eq. (3-6). In addition, the absorption efficiency is deduced from the difference of the extinction and scattering efficiencies. Thus, we have:

$$Q_{abs}^{TM} = Q_{ext}^{TM} - Q_{sca}^{TM}; \qquad Q_{abs}^{TE} = Q_{ext}^{TE} - Q_{sca}^{TE}; \tag{3-6}$$

These efficiencies are explicitly given by [135]:

$$Q_{ext}^{TE} = \frac{2}{rk_0} Re\left\{\sum_{n=-\infty}^{\infty} a_n\right\}; \qquad Q_{ext}^{TM} = \frac{2}{rk_0} Re\left\{\sum_{n=-\infty}^{\infty} b_n\right\};$$
$$Q_{sca}^{TE} = \frac{2}{rk_0} Re\left\{\sum_{n=-\infty}^{\infty} |a_n|^2\right\}; \qquad Q_{sca}^{TM} = \frac{2}{rk_0} Re\left\{\sum_{n=-\infty}^{\infty} |b_n|^2\right\}; \tag{3-7}$$

where r is the radial dimension of a NW, which is equal to $R_c + t$. Note that the NW core and the shell are composed of different semiconductors that can both contribute to light absorption. Finally, a_n and b_n can be readily obtained by solving Maxwell's equations with the appropriate boundary conditions[135,144] at the core/shell interface and shell/air interfaces. A new detailed treatment for the TE and TM modes for a random incidence angle will be presented in section A.1 of Appendix A. In addition, to benchmark the Lorentz-Mie scattering code, our calculations were validated by studying the scattering efficiency of SiNWs, and comparing our findings with what have been experimentally reported in literature. The benchmark work is presented in section A.2 of Appendix A. However, to use the Mie-Lorentz scattering formalism, the optical properties of the samples need first to be determined. For that purpose, Spectroscopic ellipsometry was used and the technique will be elaborated in full detail in the next section.

3.2 Spectroscopic ellipsometry

In this section, principles and measurement methods of spectroscopic ellipsometry (SE) will be reviewed. There are several types of spectroscopic ellipsometry instruments and, depending on the type of instruments, precision and uncertainty of measurements vary. Accordingly, to perform appropriate ellipsometry data analysis, it is essential to understand the characteristics of measurement methods as well. In this section, we will briefly address the various calibration methods, and measurement errors, in addition to the principles and methods of spectroscopic ellipsometry.

3.2.1 Principle of spectroscopic ellipsometry

When light is reflected or transmitted by samples at oblique incidence, the light is classified into p- and s-polarized light waves depending on the oscillatory direction of its electric field. Each light wave shows quite different behavior. Figure 3-2 illustrates the measurement principle of ellipsometry. When light is reflected or transmitted by a sample at oblique incidence, the light is classified into the p- and s- polarized light waves depending on the oscillating electric field. E_{ip} (E_{is}) and E_{rp}(E_{rs}) show the incident and reflected light waves for the p-polarization (s-polarization). In p-polarization, the electric fields of E_{ip} and E_{rp} oscillate within the same plane of incidence. In ellipsometry measurement, the polarization states of incident and reflected light waves are defined by the coordinates of p- and s-polarization. The vectors on the incident and reflected sides overlap completely when the incident angle is θ=90°. The incident light is the linear polarization oriented at 45° relative to the E_{ip}-axis. In particular, E_{ip}= E_{is} holds for this polarization since the amplitudes of p- and s-polarizations are the same and the phase difference between the polarizations is zero. The amplitude reflection coefficients for p- and s-polarizations differ significantly due to the difference in electric dipole radiation. Thus, upon light reflection on a sample, p- and s-polarizations show different changes in amplitude and phase. As shown in Figure 3-2, ellipsometry measures the two values (Ψ, Δ) that express the amplitude ratio and phase difference between p- and s-polarizations, respectively. In ellipsometry, therefore, the variation of light reflection with p- and s-polarizations is measured as the change in polarization state. Particularly, when a sample structure is simple, the amplitude ratio Ψ is characterized by the refractive index n, while Δ represents light absorption described by the extinction coefficient k. In this case, the two values (n, k) can be determined directly from the two ellipsometry parameters (Ψ, Δ) obtained from a measurement by applying the Fresnel equations. This is the basic principle of ellipsometry measurement. The (Ψ, Δ) measured from ellipsometry are defined from the ratio of the amplitude reflection coefficient for p- and s- polarizations through the following equation:

$$\rho \equiv \tan\Psi \exp(i\Delta) \equiv \frac{r_p}{r_s} \tag{3-8}$$

where Ψ is a measure of the relative amplitude and Δ the relative shift. From Ψ and Δ, the complex pseudo-dielectric function $\hat{\varepsilon}(\lambda) = \varepsilon_1(\lambda) + i\varepsilon_2(\lambda)$ or equivalently the complex refractive index $\boldsymbol{N} = n + ik$ can be readily derived using a two-phase model.[145]

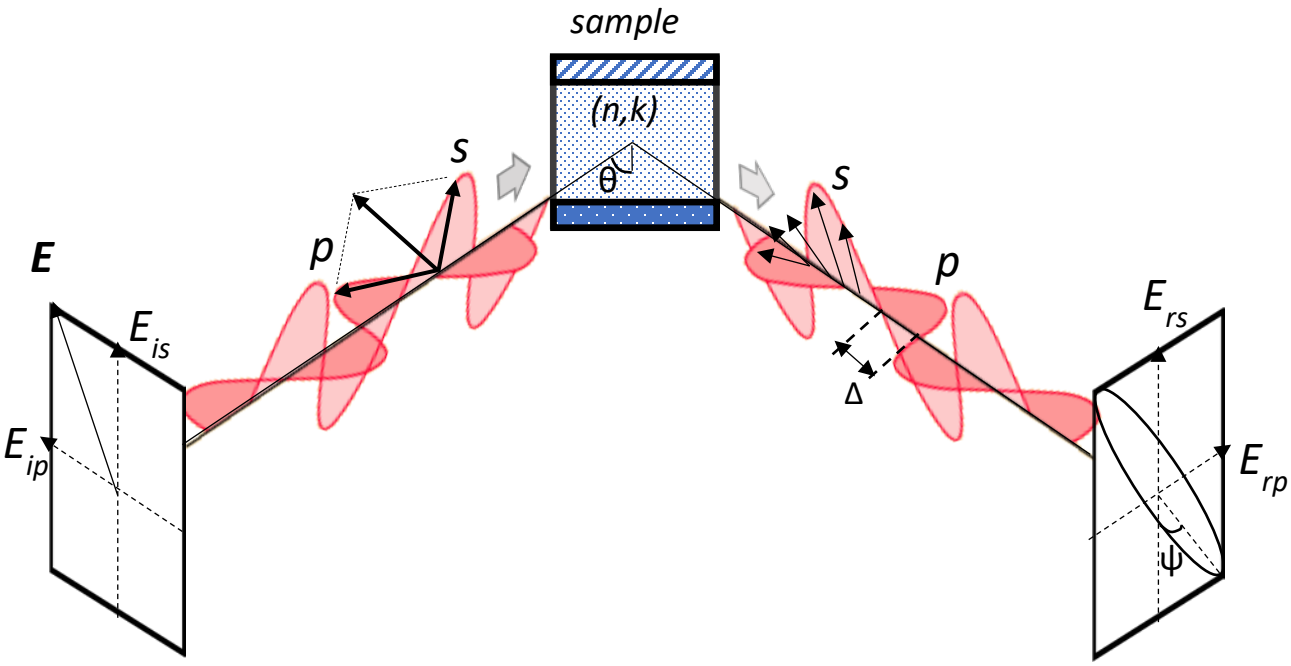

Figure 3-2: Measurement principle of ellipsometry

The objective of data analysis in spectroscopic ellipsometry is to quantify the optical properties of the analyzed sample by accurately determining the complex refractive index (n, k) or the dielectric constant $(\varepsilon_1, \varepsilon_2)$. The dielectric constant can be inferred from the pseudo-dielectric constant $\langle\varepsilon\rangle$. The pseudo-dielectric constant represents a dielectric function measured directly from Ψ and Δ and is calculated from an optical model that assumes a perfectly flat substrate with infinite thickness. Accordingly, the pseudo-dielectric function is basically different from the dielectric function of the material itself. The pseudo-dielectric function is given by

$$\langle\varepsilon\rangle = \sin^2\theta_i\left[1 + \tan^2\theta_i\left(\frac{1-\rho}{1+\rho}\right)^2\right] \tag{3-9}$$

It is evident from Eq. (3-9) that $\langle\varepsilon\rangle$ is evaluated from the measured value of ρ defined in Eq. (3-8) using an incidence angle of θ_i. $\langle\varepsilon\rangle$ is sensitive to the quality of the surface roughness and contamination. If transmitted light is measured instead of reflected light, (Ψ, Δ) are defined as

$$\rho \equiv \tan\Psi \exp(i\Delta) \equiv \frac{t_p}{t_s} \tag{3-10}$$

Finally, if we apply the definition of the reflected amplitude coefficient as a function of the electric field, we can rewrite Eq. (3-8) as:

$$\rho \equiv \tan\Psi \exp(i\Delta) \equiv \left(\frac{E_{rp}}{E_{ip}}\right)\Big/\left(\frac{E_{rs}}{E_{is}}\right) \tag{3-11}$$

For instance, in the case of Figure 3-2, Eq. (3-11) will become $\tan\Psi \exp(i\Delta) \equiv E_{rp}/E_{rs}$ since $E_{ip} = E_{is}$ for a linear light polarization.

3.2.2 Ellipsometry experimental setup

Spectroscopic ellipsometry instruments that are currently used can be classified in two main categories: instruments that use rotating optical elements [8–22], and instruments that use a photo-elastic modulator[21–30]. The rotating-element ellipsometers can further be separated into rotating-analyzer ellipsometry (RAE)[8–16,20–22] and rotating-compensator ellipsometry (RCE).[17–21] Figure 3-3 shows the schematic diagrams of the ellipsometry instrument that have extensively been used in this thesis. In general, these instruments are expressed using symbols of optical elements the rotating-analyzer ellipsometer, for example, is described by PSAR. P, S, and A represent the polarizer, sample, and the analyzer.

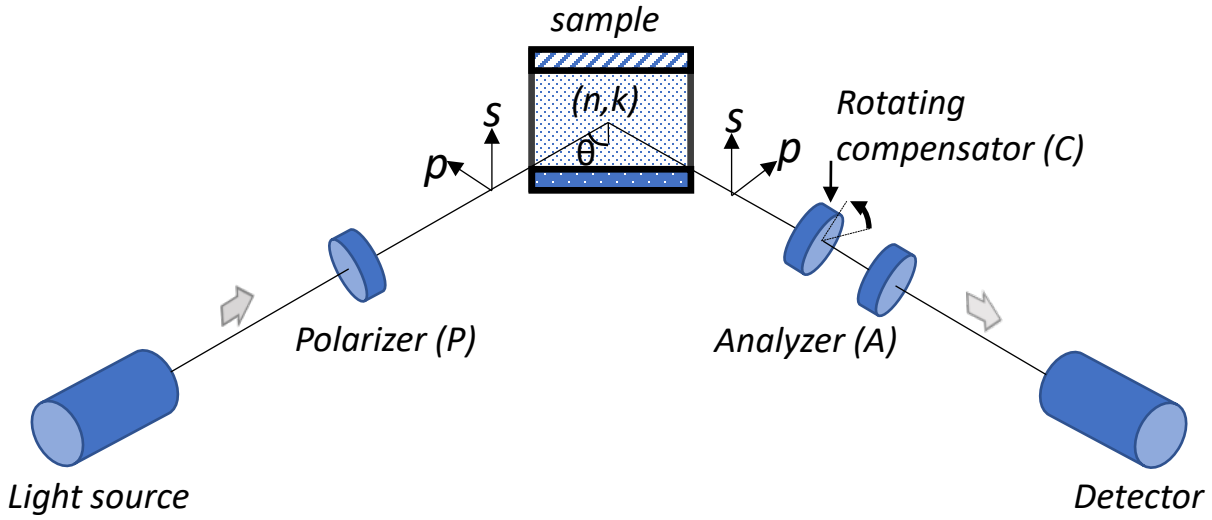

Figure 3-3: The rotating-compensator optical configuration of the used ellipsometry instrument

Understanding the precision and the error of the ellipsometry setup, the sensitivity to film thicknesses and optical constants is a fundamental task for data analysis. Especially, when samples depolarize light, extra care is needed in the interpretation of measured spectra. Many factors can explain light depolarization effects by a sample. To name a few, surface light scattering by a surface roughness of a sample, incident angle variation originating from weak collimation of probe light, wavelength variation caused by the finite bandwidth of the monochromator, thickness inhomogeneity in a thin film on top of a thick substrate and backside reflection that occurs when light absorption of a substrate is weak ($\mathbf{k}\sim0$). The above depolarization phenomena can bias data interpretation if not minimized or incorporated in the optical model. In the following section, we will introduce how optical data modeling is performed within the framework of spectroscopic ellipsometry and how depolarization phenomena can be accounted when present.

One important remark to take into consideration when building the optical model for ellipsometric measurement is the following: Ellipsometry analysis is performed by fitting the measured ellipsometric parameters (Ψ, Δ) using an optical model. Nevertheless, an optical model used in ellipsometry analysis merely represents an approximated sample structure, and the obtained results are not necessarily correct even when the fit is sufficiently good. Accordingly, when the optical constants or film structures of a sample are not known well, the ellipsometry results must be justified using other measurement methods. This is the greatest disadvantage of the ellipsometry technique. However, once an analytical method is established, it becomes possible to perform high-precision characterization in a short time using spectroscopic ellipsometry. To verify sample structures estimated from spectroscopic ellipsometry, various characterization techniques including scanning electron microscope (SEM), transmission electron microscope (TEM), and AFM can be used. Furthermore, if we perform ellipsometry analysis using a data set obtained from different incidence angles or thin film thicknesses, more reliable interpretations of the ellipsometry results can be obtained.

3.2.3 Data Analysis and optical Modeling

The optical measurements of the studied systems were performed with a commercial ellipsometer (variable-angle spectroscopic ellipsometer J. A. Woollam).[146] However, a fundamental issue for ellipsometric measurement is to accurately analyze and model a given layer due to the formation of native oxide on GeSn (e.g., GeO_2) and GeSiSn (e.g., SiO_2) layers, which cannot be prevented

despite of etching it.[146] Therefore, it is required to include surface oxide layers when building the ellipsometric model to extract the pseudo-dielectric function from the complex ellipsometric ratio ρ.

The pseudo-dielectric function is not the true dielectric functions of the investigated layers as it includes the effect of over-layers and the underlying substrates (Si and Ge). Nevertheless, it allows an acceptable interpretation of the dielectric response of the sample. The ellipsometric data were analyzed in term of a four-layer model consisting of a Si substrate, a Ge virtual substrate, a $Ge_{1-y}Sn_y$ or $Ge_{1-x-y}Si_xSn_y$ alloy, and an oxide surface layer. The dielectric function of $Ge_{1-y}Sn_y$ was analyzed with a "parametric optical constant model" developed by Johs and Herzinger. The adjustable parameters of our model are the surface layer thickness, the $Ge_{1-y}Sn_y$ or $Ge_{1-x-y}Si_xSn_y$ thickness, the Ge (VS) thickness and the Johs-Herzinger model that describes the dielectric function of the investigated alloys.[147,148] They were investigated using a proprietary Marquardt-Levenberg algorithm provided by Woollam ellipsometer's manufacturer. The known dielectric function of Si substrate as well as that of GeO_2 [149] were used in their tabulated form.[149] were used in their tabulated form. Initially, the data from Palik[150] was used for Ge virtual substrate.[150] was used for Ge virtual substrate. However, in order to enhance the optical model, we decided later on to etch the GeSn layer from a different reference sample with the highest Sn composition (Si/Ge (VS)/$Ge_{0.88}Sn_{0.12}$) in order to obtain only the bare Ge virtual substrate, which we would then optically characterize in order to extract the optical properties of the Ge VS used during the RPCVD growth of the samples. We used a chemical wet etching procedure, a CYANTEK solution composed of mixture of different solutions (H_3PO_4:$C_2H_4O_2$:HN_3:H_2O) with a volume weight ratio of 72:3:3:22. To verify the quality of the etching, multi-wavelength micro-Raman spectroscopy was employed to confirm the complete etching of the GeSn layer. After investigating the optical properties of the etched surface using VASE, we extracted the ellipsometric parameters (Ψ, Δ) and saved the obtained model and incorporated it when analyzing the studied samples discussed in chapter 6.

CHAPTER 4 ARTICLE 1: INDIRECT-TO-DIRECT BAND GAP TRANSITION IN RELAXED AND STRAINED $Ge_{1-x-y}Si_xSn_y$ TERNARY ALLOYS

This chapter has been published in the Journal of Applied Physics. Some parts were removed and put in the methodology section (3.1.1) The full reference is below: ***Attiaoui A*** *and Moutanabbir O 2014 Indirect-to-direct band gap transition in relaxed and strained* $Ge_{1-x-y}Si_xSn_y$ *ternary alloys J. Appl. Phys.* ***116*** *063712; doi: 10.1063/1.4889926*

Band gap engineering has been a key paradigm in the development of solid-state semiconductor devices. At the core of this paradigm is the ability to independently manipulate strain and band structure thus bringing to existence a variety of semiconductor low-dimensional systems and heterostructures which are the building blocks of electronic and optoelectronic devices. Up to date, III-V semiconductors ternary and quaternary alloys have been a rich playground for a precise and simultaneous control over a broad range of lattice parameter and band gap structure. Extending this concept to group IV semiconductors has, however, been a formidable endeavor. Obviously, overcoming this challenge may create a wealth of opportunities to enable a new class of silicon-compatible electronic, optoelectronic, and photonic devices. In this perspective, germanium-silicon-tin ($Ge_{1-x-y}Si_xSn_y$) alloys have been attracting a great deal of attention in recent years.[151–153] Implementing these Sn-containing group IV alloys remains very challenging from materials perspective due to the low solubility (<1 at.%) of Sn in Si and Ge. The recent progress in low-temperature chemical vapor deposition alleviates some of these difficulties leading to the growth of high-quality monocrystalline[154] layers thus setting the ground for the development of a new generation of group IV-based devices.[155] However, an accurate and optimal design of these devices requires a deep understanding of the basic properties of group IV ternary alloys. Particularly, the influence of the composition and strain on the band structure is a central element that needs to be thoroughly studied. In this regard, combined theoretical and experimental efforts are highly needed.

In this chapter, we present detailed investigations of the combined influence of strain and composition on the properties and the band structure of $Ge_{1-x-y}Si_xSn_y$. Unlike $Ge_{1-y}Sn_y$ binary alloys, which have been the subject of numerous investigations,[38,49,156] the elucidation of the interplay between composition and strain in shaping the band structure of ternary alloys is conspicuously missing in literature despite its crucial importance from both fundamental and technological standpoints. Recently, Moontragoon, Soref, and Ikonic reported a description of the band structure of fully relaxed $Ge_{1-x-y}Si_xSn_y$ alloys by using the empirical pseudopotential method (EPM) and band energy calculations in a surpercell.[155] However, this case of fully relaxed alloys remains mostly theoretical as experiments have demonstrated that there is always a certain level of strain in the epitaxial grown $Ge_{1-x-y}Si_xSn_y$ layers (see reference [157] and references therein). Therefore, a precise analysis of the band structure as well as an accurate identification of the indirect-to-direct band gap transition in these alloys must include the influence of both composition and strain. Moreover, as demonstrated in this work, an intentional introduction of strain can also be effective to tailor the band structure thus providing an additional degree of freedom in design and fabrication of group IV heterostructures and devices. Herein, we address this issue by adapting the second nearest neighbors empirical tight binding (ETB) method (2NN-sp3s*).[128] As a first step, we incorporated the effect of substitutional disorder to draw a better picture of the transition from direct to indirect band gap. Using this method, the mapping of the changes in band gap energy and directness as a function of composition and strain is achieved and compared to the available experimental and theoretical data. Note that the introduction of substitutional disorder effect can be accomplished using other methods such as the augmented space recursion (ASR),[158] the non-local coherent potential approximation (NL-CPA),[159] and the special quasi-random structure (SQS).[160] However, the choice of the method should consider the fact that the computational power and time increase quickly depending on the complexity of the approach. In this work, we show that the use of the time-effective second nearest neighbors sp3s* tight binding model leads to an accurate description of the behavior of the band structure of strained and relaxed Sn-containing group IV alloys. The manuscript is organized as follows.

The first section outlines the formalism of the empirical tight binding and the method employed to count for the effects of disorder on a ternary alloy band structure. In the second section, we present the obtained results for relaxed and strained alloys. To investigate the latter, the methodology to count for the biaxial strain in sp3s* tight binding model and obtain the

necessary deformation potential constants (DPCs) is also presented and discussed. Building on these results, the mapping of the band structure of strained $Ge_{1-x-y}Si_xSn_y$/Ge(001) heterostructure is obtained and the effects of strain, at a fixed composition, on the band structure are elucidated. Finally, salient findings are summarized in the concluding paragraph.

4.1 Empirical Tight binding formalism

4.1.1 Theoretical Background

The basics of the second nearest neighbors empirical tight binding formalism has already been elaborated in section 3.1.1 of Chapter 3. Table 4-1 shows the nineteen tight-binding parameters including the spin-orbit interaction as well as lattice parameters and elastic constants for the first and second neighbor models. It is noteworthy that the use of the parameters reported by Vogl et *al*.[128] for Sn induces an increase in the band gap energy along the ***X*** direction for the GeSn binary alloy when Sn composition increases. This stands in sharp contrast to recent results reported by Gupta et *al*.[38] and Lu Low et *al*.,[49] where the band gap along ***X*** was found to decrease for an increasing Sn composition. To solve this discrepancy, the empirical tight binding parameters (ETBP) were modified for Sn using the values obtained by Küfner et *al*.,[161] which seem to correct this issue for the binary alloys. The use of TB as interpolation scheme relies on an accurate estimation of fitting parameters. Furthermore, if one plans to use the TB as the stepping stone to calculate the electronic or optical properties of nano-scale structures such as nanowires,[162] superlattices,[163] and heterostructures,[164] it is of paramount importance to accurately reproduce the experimental valance and conduction effective masses along the highest symmetry points. However, further optimization may reduce the number of parameters and thus the computing power and time without loss of accuracy.

4.1.2 Optimization of tight-binding parameters

In the following, we define the most suitable tight binding parameters that will allow us to properly reproduce the available experimental data of the studied semiconductors. This includes the effective masses, the band edges, and the experimental band gaps. The high number of parameters to be optimized (nineteen parameters in the 2NN- sp^3s^* model compared to nine in the 1NN- sp^3s^*) renders the choice of the optimization procedure an important, yet complicated task. The problem is constructed to be a global minimization process. There exist a multitude of approaches to solve

this issue such as gradient based approach,[165] non-linear least squares optimization techniques (the Levenberg-Marquardt Algorithm[166] or the Gauss-Newton Algorithm[167]), simulated annealing[168] and its variants,[169] and bio-inspired algorithms.[170,171] Herein, the need for the parallelization and the search for a global optimum solution justify the choice of the evolutionary based method. Specifically, a variant of the Genetic algorithm approach (GA) the differential evolution[172] (DE) was adopted in this work. DE is a metaheuristic optimization approach that make few assumptions about the problem being optimized. [172] The remarkable advantage of the DE formalism compared to other GA approaches is the reduced computational time. The physics of the problem is incorporated into a fitness function that measures the weighted sum of the normalized variances between the calculated physical values and their experimental counterparts. For instance, the evaluated and targeted band gaps and effective masses for different group IV semiconductors are shown respectively in Tables 4-2, 4-3, and 4-4 demonstrating a good agreement between the calculated and targeted values for different semiconductors. It is important to mention that during the optimization procedure, we only focused on reproducing the two lowest and three highest energy bands for the conduction and valance bands (HH, LH and SOH), respectively.

4.1.3 Effect of disorder on calculations of ternary alloy band structure

After verification of the validity of the 2NN-sp^3s^* model by estimating the elemental semiconductors band gaps (Table 4-2), it becomes possible to evaluate the band gaps for the $Ge_{1-x-y}Si_xSn_y$ ternary alloys using the universal tight binding method based on a modified pseudo-cell (MPC) initially introduced by Shim et *al*. to investigate III-V compound semiconductors.[173] The MPC is a periodic virtual cell describing the alloy as an effective-perfect bulk system, in which the alloy $Ge_{1-x-y}Si_xSn_y$ is defined as consisting of three fictive atoms Ge, Si, and α-Sn residing on an atomic site. We have three possible unit Ge, Si, and α-Sn with mixing probabilities of 1-*x*-*y*, *x*, and *y*, respectively. We will consider the effect of disorder by considering that each unit is disordered by the presence of the other two atoms. The alloy Hamiltonian can thus be written under the virtual crystal approximation as: $H_{Ge_{1-x-y}Si_xSn_y} = (1-x-y)H_{Ge} + xH_{Si} + yH_{Sn}$.

The effective Hamiltonian H_{Ge} corresponds to the non-disordered Hamiltonian H_{Ge}^0 plus ΔH_{Ge}, which is the disordered Hamiltonian of Ge induced by the presence of Si ($\Delta H_{Si:Ge}$)and Sn ($\Delta H_{Si:Sn}$) atoms at a composition of *x* and *y*, respectively. This disordered Hamiltonian is given

by $\Delta H_{Ge} = x\Delta H_{Ge:Si} + y\Delta\, H_{Ge:Sn}$. Similarly, we can establish the expression of the disordered Hamiltonian for Si and α-Sn as in the previous equation to finally get the total disordered Hamiltonian of the alloy:

$$\begin{aligned} H_{Ge_{1-x-y}Si_xSn_y} &= (1-x-y)H^0_{Ge} + xH^0_{Si} + yH^0_{Sn} \\ &+ (1-x-y)[x\Delta H_{Ge:Si} + y\Delta H_{Ge:Sn}] \\ &+ x[y\Delta H_{Si:Sn} + (1-x-y)\Delta H_{Si:Ge}] \\ &+ y[(1-x-y)\Delta H_{Sn:Ge} + x\Delta H_{Sn:Si}] \end{aligned} \tag{4-1}$$

Table 4-1: Tight Binding Parameters in eV for the first nearest neighbor method (1NN-TBP) and second nearest neighbors approach (2NN-TBP) using differential evolution method for Si, Ge and α-Sn.

	Elemental Semiconductor					
	Si		Ge		α-Sn	
Tight binding parameters[a]	1NN[b]	2NN-DE	1NN[b]	2NN-DE	1NN[c]	2NN-DE
E_s	−4.2000	−4.20400	−5.8800	−5.80199	−5.5700	−6.13607
E_p	1.7150	1.82224	1.6100	1.94636	1.2100	1.03156
E_{s^*}	6.6850	6.78479	6.3900	6.31711	13.5402	5.90062
V_{ss}	−8.3000	−8.38947	−6.7800	−6.97292	−5.4600	−6.12601
V_{xx}	1.7150	1.68811	1.6100	1.73941	−0.0047	1.44997
V_{xy}	4.5750	4.58185	4.9000	4.99643	1.6802	3.68002
V_{sp}	5.7292	7.11588	4.9617	6.46170	4.0172	4.71063
V_{s^*p}	5.3749	6.05591	4.5434	4.70230	5.5459	3.28819
$V_{ss}(110)$		0.00756		0.03821		0.05774
$V_{s^*s^*}(110)$		0.40000		0.41704		0.16906
$V_{ss^*}(110)$		0.00174		0.02233		0.53341
$V_{sx}(110)$		0.00700		0.00170		−0.73354
$V_{sx}(011)$		0.85685		0.89057		0.60000
$V_{s^*x}(110)$		−0.00279		−0.03667		−0.08661
$V_{s^*x}(011)$		0.61767		0.71905		0.76565
$V_{xx}(110)$		0.11859		0.14554		0.24437
$V_{xx}(011)$		−0.19289		−0.13583		−0.17385
$V_{xy}(110)$		0.28397		0.36186		0.43585
$V_{xy}(011)$		−1.00016		−0.09514		−0.87199
λ[d]	0.0146		0.0966		0.2333	
a (Å)[e]	5.43095		5.64613		6.48920	
C_{11}(ergs/cm^3)[e]	16.57		12.89		10.6	
C_{12}(ergs/cm^3)[e]	6.39		4.83		2.66	
d_1 (Å)[f]	2.35		2.45		2.81	
d_2 (Å)[g]	3.84		4.00		4.58	

a. Table I from Reference [128]
b. Reference [161]
c. λ is equal to $\Delta/3$ where Δ is the renormalized atomic spin-orbit splitting of the anion and cation p states
d. Reference [174]
e. d_0 is the bond length between nearest neighbors atoms, value from Table I in Reference [131] $\left(d_1 = \sqrt{3}a/4\right)$
f. d_1 is the bond length between second nearest neighbors atoms, $d_2 = \sqrt{2}a/2$

All the first and second nearest tight binding parameters are expressed in units of eV.

Table 4-2: Eigenvalues for diamond structure semiconductor at symmetry points Γ, X and L obtained from 2NN-sp3s* model and compared to experimental and non-local pseudopotential method.[175]

		Si		Ge		Sn	
Points	**Levels**	**Calc.**	**Expt.**	**Calc.**	**Expt.**	**Calc.**	**Expt.**
				[eV]			
Γ	Γ_{15c}	3.3321	3.34 [a]	3.1888	3.2060		
	Γ_{25v}	0	0				
	Γ_{6}					2.0999	2.08 [c]
	Γ_{7c}			0.8260	0.89	-0.4162	-0.42 [c,f]
	Γ_{7v}	-0.0440	-0.044 [c]	-0.2900	-0.29 [c]	-0.8000	-0.80 [c]
X	X_{5c}	1.1189	1.13 [a]	1.1598	1.16 [a]	1.0179	0.96 [g]
	X_{5v}	-2.9000	-2.90 [b]	-3.3746	-3.29 [d]	-2.5569	-2.43 [g]
L	L_{1c}	1.9743	2.06 [a]				
	L_{3c}	3.8607	3.90 [a]				
	$L_{4,5v}$	-1.2072	-1.20 [a]	-1.4219	-1.43 [e]	-0.9941	-0.97 [g]
	L_{6c}			0.7596	0.76 [e]	0.1669	0.17 [g]
	L_{6v}			-1.6176	-1.63 [e]	-1.5536	-1.41 [g]
	L_{6c}^{+}					3.2099	3.25 [g]

a. Reference [176]
b. Reference [177]
c. Reference [175]
d. Reference [178]
e. Reference [179]
f. The Γ_7 conduction band has shifted below the Γ_{8v} band, thus $E(\Gamma_{7c})$ is negative.
g. Reference [180]

It is, however, possible to simplify the total disordered Hamiltonian given in (4-1) if we consider that the total disordered energy in the Si:Ge ($\Delta H_{Si:Ge}$) and Ge:Si ($\Delta H_{Ge:Si}$) units can be approximated as the bond alteration energy[173] between Si and Ge such as:

$$\Delta H_{Si:Ge} + \Delta H_{Ge:Si} \cong H_{Si}^{0} - H_{Ge}^{0}.$$

We follow the same procedure for Si:Sn, Sn:Si, Ge:Sn and Sn:Ge to finally get

$$\begin{aligned} H_{Ge_{1-x-y}Si_xSn_y} \cong (1-x-y)H_{Ge}^{0} + xH_{Si}^{0} + yH_{Sn}^{0} + (1-x-y)x\left[H_{Si}^{0} - H_{Ge}^{0}\right] \\ + y(1-x-y)[H_{Ge}^{0} - H_{Sn}^{0}] + xy\left[H_{Si}^{0} - H_{Sn}^{0}\right] \end{aligned} \quad (4\text{-}2)$$

Now we must include this alloy Hamiltonian with the ETB method to evaluate the band structure of the alloy. In the ETB formulation, the Hamiltonian matrix elements are determined by interpolating between the elemental parent crystal TB parameters developed in the first part according to alloy composition and based upon the equation (4-2). Using the d^{-2} Harrison's rule, the ETBP are described by:

$$E_{\alpha\alpha'}(x,y) \cong \left[\sum_{i=Si,Ge,Sn} d_i x_i\right]^{-2}\left[\sum_{i=Si,Ge,Sn} (d_i)^2 x_i E_i + \sum_{\substack{i,j \\ i\neq j}} x_i x_j \left(E_i - E_j\right)\left(d_i - d_j\right)^2\right] \quad (4\text{-}3)$$

where d_i can take two values: the first d_1 is the nearest neighbors distance in crystalline Si, α-Sn, and Ge given in Table 4-1 for the 1NN parameters; and the second d_2 is the second nearest neighbors distance for 2NN parameters. x_i is the composition of the alloying element and E_i is the ETBP. The labels α and α' correspond to the s, p_x, p_y, p_z, and s^* states of the sp^3s^* model describing the atomic orbitals. Thus, with this approach it becomes possible to find the ETBP of the ternary alloy from the TBP of the elemental parent atoms.

Table 4-3: Band gap transition energies of Ge, Si and α-Sn along highest symmetry axes **Γ**, **L**, and **X**.

Band Gaps energies [eV]	**Si**		**Ge**		**Sn**	
	Calc.	**Expt.**	**Calc.**	**Expt.**	**Calc.**	**Expt.**
E^{Γ}	3.3321	3.34 [a]	0.8260	0.898(1) [d]	-0.41	-0.41 [f]
E^{X}	1.157	1.12 [b]	1.1598	1.16 [a]	3.665	3.681 [g]
E^{L}	2.114	2,10 [c]	0.7596	0.76 [e]	0.118	0.12 [h]

a. Reference [176]
b. Reference [174]
c. Reference [181]
d. Reference [182]
e. Reference [179]
f. Reference [183]
g. Reference [184] [between $X_{5c} - X_{5v}$ levels]
h. Reference [185] [between $L_{6c} - \Gamma_8$]

Table 4-4: Effective masses reproduced by the tight-binding parameters of Table 4-1 using the differential evolution method. Masses are expressed in terms of electron mass.

Effective masses $(/m_0)$	**Si**		**Ge**		**Sn**	
	Calc.	**Expt.** [a]	**Calc.**	**Expt.** [b]	**Calc.**	**Expt.** [c]
$m_e^{[001]}$	0.24484	0.188	0.04120	0.0380	--	-0.087
$m_{LH}^{[001]}$	-0.15131	-0.214	-0.04652	-0.0457	--	0.023
$m_{LH}^{[110]}$	-0.16830	-0.152	-0.04826	-0.0417	--	0.024
$m_{LH}^{[111]}$	-0.13493	-0.144	-0.04332	-0.0406	--	0.025
$m_{HH}^{[001]}$	-0.35901	-0.276	-0.27172	-0.2149	-0.246	-0.210
$m_{HH}^{[110]}$	-0.28962	-0.518	-0.22459	-0.3830	-0.352	-0.400
$m_{HH}^{[111]}$	-0.50422	-0.734	-0.47772	-0.5020	-0.419	-0.510
$m_{so}^{[001]}$	-0.21446	-0.296	-0.10114	-0.0950	-0.052	-0.041

a. Reference [186] [using Genetic Algorithm approach]
b. Reference [49]
c. Reference [187]

4.2 Results and discussion

4.2.1 Band structure of unstrained $Ge_{1-x-y}Si_xSn_y$

Using the optimized tight binding parameters, the diagonalization of the 20×20 matrix for each wave vectors $\boldsymbol{k}$ allows us to obtain the band structure of each bulk material. By considering the $\Gamma \rightarrow L$ and $\Gamma \rightarrow X$ directions, we start by presenting the band structure of Si, Ge, and α-Sn using the 2NN sp^3s^* model. The obtained results are displayed in Figure 4-1. Note that the spin-orbit splitting in Si cannot be observed due to the small separation between the Γ_7 (spit off valence band) and Γ_8 (Light and heavy hole valence band) (see the inset in Figure 4-1, middle). The splitting is, however, more apparent for Ge and α-Sn. We try now to consolidate the sp^3s^* by comparing the band energies at the highest symmetry points (X, L, Γ) with data from experimental measurements or first principle calculations whenever available. This comparison is summarized in Table 4-2 demonstrating that the estimated energies between the conduction band minimum (CBM) and the valance band maximum (VBM) are in very good agreement with known values for the three materials with a relative difference below 1%. These energies are crucial for determining the optical properties of the ternary alloys. That is why extra care must be given when writing the fitness function. Next, the transition energies between the CBM and VBM are investigated more in detail by presenting in the Tables 4-2 and 4-3 the direct and indirect band gaps. From these tables, one can deduce that the calculated band gaps agree very well with the measured ones at the highest symmetry points Γ, X, and L.

Additionally, the calculated effective masses are also compared to the available data as shown in Table 4-4. The dependency of the effective masses at the conduction and valance band for the 2NN-sp^3s^* is given in reference [130]. It is noticeable that the calculated and the known values of the effective masses agree fairly well especially for Ge and Si. For α-Sn, we note that it is relatively difficult to directly calculate the effective masses for the electron and light holes. This can be explained by the symmetry inversion[187] between Γ_{8vc}^{+} and Γ_{7c} that occurs in α-Sn. This effect is not incorporated in the 2NN- sp^3s^* effective masses dependency with tight binding parameters. In principle, the missing effective masses can be estimated from the curvature of the calculated valence and conduction bands minima and maxima.

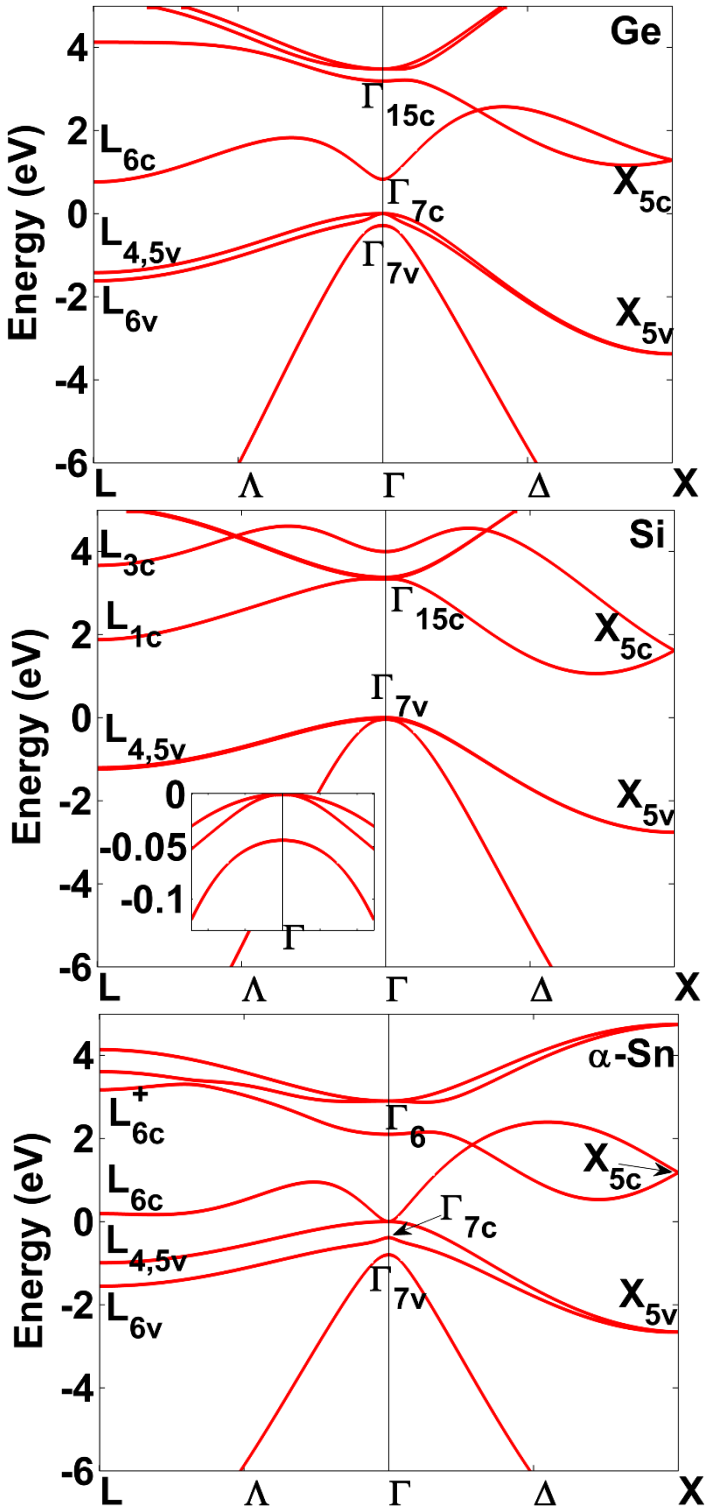

Figure 4-1: Bulk band structure obtained with 2NN-sp^3s^* ETB model for the elemental group semiconductors (a) Si, (b) Ge and (c) α-Sn using the parameters from Table 4-1.

In the following, we include the effect of disorder in band structure based on the procedure presented in the previous section. In order to quantify the effect of disorder on the band gaps, we calculate the band gaps with and without lattice disorder as a function of Si and α-Sn compositions. The obtained values are presented in Table 4-5 in comparison with the available experimental[188] and theoretical data.[155]

Table 4-5: Comparison between experimental values of the band gap[188] and calculated band gap based on the 2NN-sp3s* TB model (with and without the disorder contribution) model and the supercell mixed atom model.[155]

Si [a]	Sn [a]	Band Gap [eV]			
		Without disorder	With disorder	Expt. [a]	Theo. [b]
0	0.0483 ± 0.005	0.7522	0.6145	0.630 ± 0.002	0.70
0	0.0642 ± 0.005	0.7167	0.6080	0.577 ± 0.003	0.68
0.059 ± 0.005	0.052 ± 0.005	0.9364	0.8170	0.95 ± 0.02	0.81
0.055 ± 0.005	0.059 ± 0.005	0.9072	0.7956	0.88 ± 0.02	0.80
0.064 ± 0.005	0.088 ± 0.005	0.9218	0.8301	0.83 ± 0.02	0.72
0.084 ± 0.005	0.073 ± 0.005	0.9866	0.8918	0.95 ± 0.02	0.82
0.098 ± 0.005	0.058 ± 0.005	1.0581	0.9373	1.02 ± 0.02	0.91

a. Reference [188] (The compositions of Si and Sn were measured by x-ray diffraction)
b. Reference [155]

The latter, presented in the sixth column of Table 4-5, are obtained based on the empirical pseudopotential method within the virtual crystal approximation and the supercell (mixed-atom) method. It is clear from this comparison that the best agreement with experimental data, extracted from photoreflectance measurements,[188] is obtained using the 2NN-sp3s* TB when the disorder is accounted for. Using this model, we have then carried out a systematic energy band calculation for $Ge_{1-x-y}Si_xSn_y$ alloys along symmetrical axes ($L \rightarrow \Gamma \rightarrow X$) for x and y varying in the range of 0 to 40 at.% and 0 to 30 at.%, respectively. The TB parameters for the three constituent parent atoms are defined in the previous section. We found that the CBM can occur at the L point ($2\pi/a_L \left(\frac{1}{2},\frac{1}{2},\frac{1}{2}\right)$),

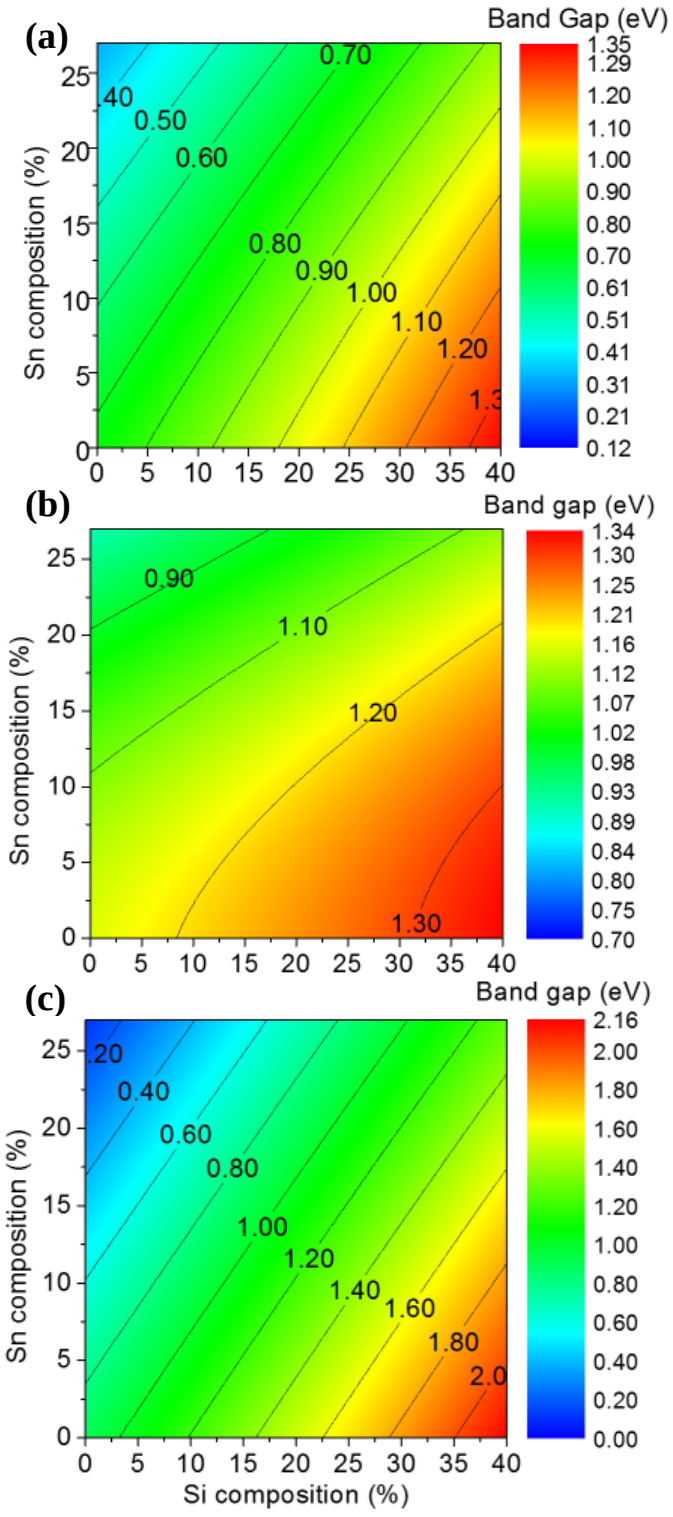

Figure 4-2: Band structure maps of unstrained disordered ternary alloy $Ge_{1-x-y}Si_xSn_y$ through: **(a)** L, **(b)** X and **(c)** Γ symmetry points.

at the X point ($2\pi/a_L$ (1,0,0)), or at the Γ point depending on the value of (x; y) pairs. Therefore, the band gap of the alloy is either direct or indirect depending on the concentration of Si and Sn in the alloy, with the VBM at the center of the Brillouin zone. The composition dependence of the principal band gaps for the $Ge_{1-x-y}Si_xSn_y$ alloys is presented in Figure 4-2 showing the maps around the highest symmetry point X, L and Γ. From this figure, it is possible to evaluate the band gap directness of a given alloy. Figure 4-3 exhibits the map of the crossover between direct to indirect band gap for relaxed ternary alloys. Figure 4-3 also incorporates the effect of disorder on the band gap at the highest symmetry points. We note that when the composition of Sn increases, the band gap energies decrease, whereas when the concentration of Si increases, the band gap becomes wider. At the X symmetry point, the band gap exhibits the same behavior, but varies slowly with the composition as compared to the Γ symmetry point. From these results, it is also possible to study different Sn-containing binary alloys (GeSn and SiSn). For instance, for the GeSn binary alloy, there are conflicting reports in literature suggesting that the direct-to-indirect bandgap transition occurs at an Sn content of 7% (reference [189]) or 11% Sn with a gap of 0.477 eV (reference [147]). Here, we found that the transition occurs at 11% Sn corresponding to a gap of 0.495 eV (the intersection of the solid line with the y axis in Figure 4-3) in agreement with reference [147].

4.3 Band Structure of Strained $Ge_{1-x-y}Si_xSn_y$

4.3.1 Introduction of biaxial strain in sp^3s^* tight binding model

In order to include the strain in empirical tight binding formalism, we need to undertake the following steps. First, we define the equation of the dependence of directional cosine on strain and how it should be integrated with ETBP. Next, we identify the parameters that should change due to the effect of strain following the d^{-2} Harrison rule, which will be defined later. Then, we find the unstrained bond length d_0 and strained ones d. Subsequently, we calculate the scale index empirically. For this, we need to find the DPCs of Si, Ge, and α-Sn as well as those of the ternary alloy. The latter are sensitive to the effect of lattice disorder. Table VII compares the experimental and the calculated DPCs of Si, Ge, and α-Sn. If we consider an epilayer of a zinc-blende-type crystal structure grown epitaxially on a Ge(001) substrate, the in- and out-of-plane strain components are: $\varepsilon_{xx} = \varepsilon_{yy} = \varepsilon_{\parallel} = \Delta a$, $\varepsilon_{zz} = \varepsilon_{\perp} = -2(C_{12}/C_{11}) \times \Delta a$, where and C_{ij}'s are the

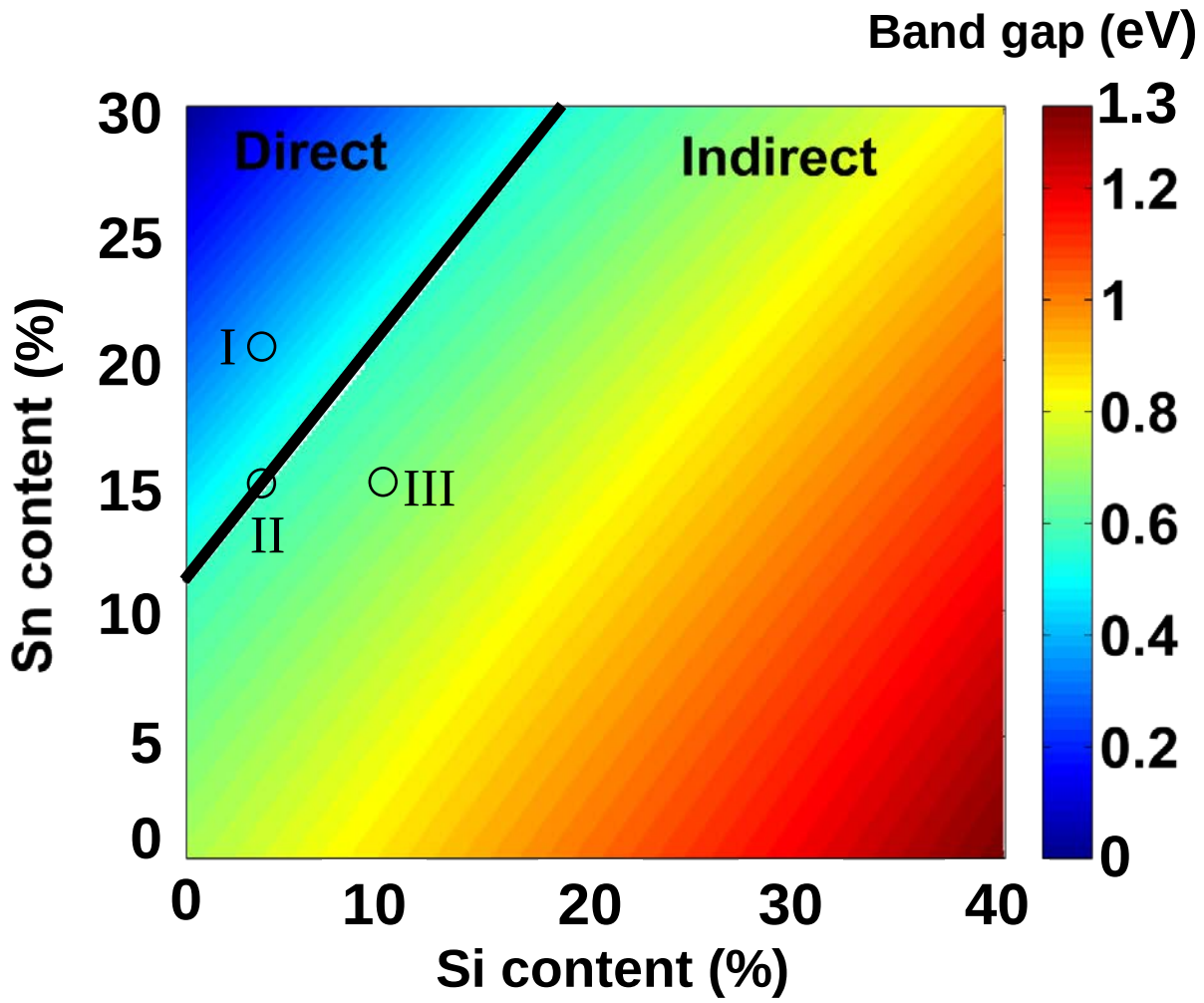

Figure 4-3: Direct-Indirect Crossover of the unstrained $Ge_{1-x-y}Si_xSn_y$ ternary alloy. Two different regions are distinguishable: The direct region and the L-indirect zones. The empty circles indicated are the selected alloys investigated in Figure 4-8.

elastic stiffness constants presented in Table 4-1. $\Delta a = (a_s - a^*)/a_s$ is the lattice mismatch where a_s and a^* denote the lattice constants of the Ge substrate and the $Ge_{1-x-y}Si_xSn_y$ epilayer, respectively. A biaxial strain has two contributions on the band structure: a hydrostatic component which shifts the band gap energy; and a uniaxial component which splits the bands. Note that if the biaxial strain is compressive, $\varepsilon_{\parallel} < 0$, the hydrostatic pressure is also compressive but the uniaxial strain in the [001] direction is tensile in nature. In the absence of strain, the effect of spin-orbit lifts the light and heavy hole bands with respect to the split-off band. The shear components of the strain lead to additional spin-orbit splitting thus producing the final valence band position. The effect of strain on the energy band position can be calculated using the following set of equations: [190–192]

$$
\begin{aligned}
\mathrm{E}_{c\varepsilon}^{\Gamma} &= E_{c0}^{\Gamma} + a_{\Gamma_2^-}(\varepsilon_{xx}+\varepsilon_{yy}+\varepsilon_{zz}) \\
\mathrm{E}_{c\varepsilon}^{\mathrm{L}} &= E_{c0}^{\mathrm{L}} + \left[\Xi_d + \frac{1}{3}\Xi_u - a_{\Gamma_5^+}\right]^L (\varepsilon_{xx}+\varepsilon_{yy}+\varepsilon_{zz}) \\
\mathrm{E}_{c\varepsilon}^{\Delta_2} &= E_{c0}^{\Delta_2} + \left[\Xi_d + \frac{1}{3}\Xi_u - a_{\Gamma_5^+}\right]^\Delta (\varepsilon_{xx}+\varepsilon_{yy}+\varepsilon_{zz}) + \frac{2}{3}\Xi_u^\Delta(\varepsilon_{zz}-\varepsilon_{xx}) \\
\mathrm{E}_{c\varepsilon}^{\Delta_4} &= E_{c0}^{\Delta_4} + \left[\Xi_d + \frac{1}{3}\Xi_u - a_{\Gamma_5^+}\right]^\Delta (\varepsilon_{xx}+\varepsilon_{yy}+\varepsilon_{zz}) - \frac{1}{3}\Xi_u^\Delta(\varepsilon_{zz}-\varepsilon_{xx}) \\
E_{v\varepsilon}^{LH} &= E_{v0}^{LH} + \frac{1}{3}\Delta_0 - \frac{1}{2}\delta E_{001} \\
E_{v\varepsilon}^{HH} &= E_{v0}^{HH} - \frac{1}{6}\Delta_0 + \frac{1}{4}\delta E_{001} + \frac{1}{2}\left[\Delta_0^2 + \Delta_0\delta E_{001} + \frac{9}{4}(\delta E_{001})^2\right]^{1/2} \\
E_{v\varepsilon}^{SO} &= E_{v0}^{SO} - \frac{1}{6}\Delta_0 + \frac{1}{4}\delta E_{001} - \frac{1}{2}\left[\Delta_0^2 + \Delta_0\delta E_{001} + \frac{9}{4}(\delta E_{001})^2\right]^{1/2} \\
\delta E_{001} &= 2b_{\Gamma_5^+}(\varepsilon_{zz}-\varepsilon_{xx})
\end{aligned}
\tag{4-4}
$$

where $E_{\mu\nu}^{m}$ is the strained ($\nu=\varepsilon$) or unstrained ($\nu=0$) conduction ($\mu=c, m=L,\Delta_2,\Delta_4,\Gamma$) or valance ($\mu=v, m=LH,HH,SOH$) band energy level. These equations will be used later to find the DPCs for Si, Ge, and α-Sn through a least-square fitting procedure. In the following, we focus on how the lattice structure of the ternary alloy is affected by the strain. By definition, the strain tensor $\overleftrightarrow{\epsilon}$ is associated to a displacement of an atom located at a position $\boldsymbol{r}$ in the crystalline solid by the vector $\boldsymbol{R}(r)=\overleftrightarrow{\epsilon}\,\mathbf{r}$. Thus, for a biaxial strain in the (001) plane, we find that the changes $\delta\boldsymbol{d}_i$ of the nearest-neighbor vectors $\boldsymbol{d}_j$ in the zinc-blende type crystal can be written as:

$$
\begin{aligned}
\delta\mathbf{d}_1 &= \frac{\mathrm{a}}{4}\left(\varepsilon_{\mathrm{xx}},\varepsilon_{\mathrm{yy}},\varepsilon_{\mathrm{zz}}\right)^{\mathrm{T}} = \frac{\mathrm{a}}{4}\,\varepsilon_{\parallel}(1,1,-2\beta)^{\mathrm{T}} \\
\delta\mathbf{d}_2 &= \frac{\mathrm{a}}{4}\left(-\varepsilon_{\mathrm{xx}},-\varepsilon_{\mathrm{yy}},\varepsilon_{\mathrm{zz}}\right)^{\mathrm{T}} = \frac{\mathrm{a}}{4}\,\varepsilon_{\parallel}(-1,-1,-2\beta)^{\mathrm{T}} \\
\delta\mathbf{d}_3 &= \frac{\mathrm{a}}{4}\left(\varepsilon_{\mathrm{xx}},-\varepsilon_{\mathrm{yy}},-\varepsilon_{\mathrm{zz}}\right)^{\mathrm{T}} = \frac{\mathrm{a}}{4}\,\varepsilon_{\parallel}(1,-1,2\beta)^{\mathrm{T}} \\
\delta\mathbf{d}_4 &= \frac{\mathrm{a}}{4}\left(-\varepsilon_{\mathrm{xx}},\varepsilon_{\mathrm{yy}},-\varepsilon_{\mathrm{zz}}\right)^{\mathrm{T}} = \frac{\mathrm{a}}{4}\,\varepsilon_{\parallel}(-1,1,2\beta)^{\mathrm{T}}
\end{aligned}
\tag{4-5}
$$

where we have defined $\beta \equiv C_{12}/C_{11}$ as the ratio of the elastic compliance constants. Consequently, an atom located at $\boldsymbol{d}_j$ in the unstrained solid will be displaced by $\delta\boldsymbol{d}_j$, and it will be located in the distorted solid at $\boldsymbol{d}_j^{(\varepsilon)} = \boldsymbol{d}_j + \delta\boldsymbol{d}_j$

$$\begin{aligned}
\mathbf{d}_1^{(\varepsilon)} &= \frac{\mathrm{a}}{4}(1,1,1)^{\mathrm{T}} + \frac{\mathrm{a}}{4}\,\varepsilon_{\parallel}(1,1,-2\beta)^{\mathrm{T}} \\
\mathbf{d}_2^{(\varepsilon)} &= \frac{\mathrm{a}}{4}(-1,-1,1)^{\mathrm{T}} + \frac{\mathrm{a}}{4}\,\varepsilon_{\parallel}(-1,-1,-2\beta)^{\mathrm{T}} \\
\mathbf{d}_3^{(\varepsilon)} &= \frac{\mathrm{a}}{4}(1,-1,-1)^{\mathrm{T}} + \frac{\mathrm{a}}{4}\,\varepsilon_{\parallel}(1,-1,2\beta)^{\mathrm{T}} \\
\mathbf{d}_4^{(\varepsilon)} &= \frac{\mathrm{a}}{4}(-1,1,-1)^{\mathrm{T}} + \frac{\mathrm{a}}{4}\,\varepsilon_{\parallel}(-1,1,2\beta)^{\mathrm{T}}
\end{aligned} \tag{4-6}$$

We also define the length d of the distorted bond assuming a uniform deformation of the diamond- like unit cell as: $d = a\sqrt{3 + 4(1-\beta)\varepsilon_{\parallel} + 2[1+\beta^2]\varepsilon_{\parallel}^2}/4$. The description of the newly distorted bonds for the second nearest neighbors' atoms follows the same procedure as in Eq. (4-6). However, the only difference resides in the relaxed atomic positions which are described by $a/2\,\langle 110\rangle$.

The angular variation of bonds due to strain is considered via the changes of the directing cosine entering the two-center integrals terms. Furthermore, the variation of distances between atoms is empirically introduced into the Hamiltonian matrix elements by means of the Harrison d^{-2} scaling rule of the form: $\mathrm{V}_{\mathrm{mn}}^{\varepsilon} = \mathrm{V}_{\mathrm{mn}}^{0}\left(\frac{\mathrm{d}_0}{\mathrm{d}}\right)^{\eta(\mathrm{mn})}$, where the overlap parameters $\mathrm{V}_{\mathrm{mn}}^{\varepsilon}$ and $\mathrm{V}_{\mathrm{mn}}^{0}$ are the strained and unstrained Hamiltonian matrix elements of the atomic orbitals $\{m,n\} \in \{p_x, p_y, p_z, s, s^*\}$; d and d_0 are the distorted and equilibrium bond lengths respectively (given in Table 4-1), and $\eta(mn)$ is the scaling index. Harrison proposed $\eta(\mathrm{mn}) = -2, \forall \mathrm{m,n}$.[193] However, Priester et *al*.[194] found a better agreement between calculated and experimental DPCs. We will follow the same optimization procedure and adjust the scaling indices $\eta(mn)$. Furthermore, in order to include the effect of both the bond length and bond angle modification due to strain, we have used the Slater-Koster[127] relationship given by for the first nearest neighbors parameters:

$$
\begin{aligned}
V_{ii} &= l_i^2 V_{pp\sigma} + \left(1 - l_i^2\right)\mathrm{V_{pp\pi}} \\
V_{ij} &= l_i l_j V_{pp\sigma} - l_i l_j \mathrm{V_{pp\pi}} \\
V_{spi} &= l_i V_{sp\sigma} \\
i, j &= X, Y, Z
\end{aligned}
\tag{4-7}
$$

where l_i is the direction cosines between the strained $\vec{d}$ first and second nearest neighbor vector and the X, Y, and Z vectors.[127] For the second nearest neighbor's parameters, the new strained ETB are modified following the same rule as in Eq. (4-7), but where the l_i, $V_{pp\sigma}$, $V_{pp\pi}$ and $V_{sp\sigma}$ are tight binding parameters whose values depend on the ETBP given in Table 4-1. Munoz and Armelles[195] introduced a new scaling parameters *F* in order to account for the X symmetry point modification due to strain in III-V semiconductors as follows:

$$
\begin{aligned}
V_{s^*p_x} = V_{s^*p_y} &= \left(\frac{d}{d_0}\right)^{\eta(s^*p)+1} \mathrm{V^0_{s^*p_x}}\left[1 + \varepsilon_{xx} - F(\varepsilon_{zz} - \varepsilon_{xx})\right] \\
V_{s^*p_z} &= \left(\frac{d}{d_0}\right)^{\eta(s^*p)+1} \mathrm{V^0_{s^*p_x}}\left[1 + \varepsilon_{zz} + 2F(\varepsilon_{zz} - \varepsilon_{xx})\right]
\end{aligned}
\tag{4-8}
$$

where the new scale index, *F*, is determined from fitting with the experimental values of shear deformation potential. The dependence of the smaller second-nearest neighbor TB parameters on bond angles is not important and therefore it is neglected here. In fact, the difference of magnitude between the first and second nearest neighbors TB parameters allow us to assert this approximation as shown in Table 4-1. Finally, the diagonal matrix element $E_p^{(x,y)}$ is evaluated using the following equations:[129]

$$
\begin{aligned}
E_p^{(x,y)} &= \mathrm{E}_p\left[1 + 2b_p(\varepsilon_{zz} - \varepsilon_{xx})\right] \\
E_p^{(x,z)} = E_p^{(y,z)} &= \mathrm{E}_p\left[1 - b_p(\varepsilon_{zz} - \varepsilon_{xx})\right]
\end{aligned}
\tag{4-9}
$$

where b_p is a shear parameter of the p states fitted to reproduce the uniaxial deformation b of the valance band edges. To recapitulate, in addition to the scaling index $\eta(mn)$ presented in the

equations above, we have added two more scaling indices F and b_p. Our goal is to find good estimation for theses parameters through fitting routines while keeping in mind that we have to reproduce the known experimental and/or theoretical DPCs for Ge, Si, and α-Sn. After achieving this objective, it will become relatively straightforward to estimate the scaling index for the ternary alloy $Ge_{1-x-y}Si_xSn_y$ using a linear interpolation between Ge, Si, and α-Sn values.

4.3.2 Deformation potential constants (DPCs)

To evaluate the DPCs using the 2NN-sp^3s^*, we need to find first the scaling parameters $\eta(mn)$ as well as the parameters F and b_p. Towards this end, we adopted two different approaches: the first is based on a non-linear conjugate gradient optimization method (CGOM); and the second employs Monte-Carlo simulations. The first approach allows a simultaneous evaluation of the scaling parameters and DPCs. On the other hand, the second permits to find only the DPCs by randomly generating 10,000 sets of uniformly distributed scaling parameters within the -4–1 range and then fitting the obtained strained energy to the equations presented in Eq. (4-4) to finally extract the corresponding DPC. For CGOM, we defined a multivariate weighted fitness function in order to achieve a better agreement between the available experimental or theoretical values of the DPC. The expression of the fitness function is given by:[196]

$$f(\eta) = \sqrt{\frac{\sum_i w_i \left(DPC_i(\eta) - DPC_{i,opt}\right)^2}{\sum_i w_i}} \qquad (4\text{-}10)$$

where $DPC_i(\eta)$ are the DPCs calculated with the set of parameters η, $DPC_{i,opt}$ are the optimal values of the DPC, and w_n is a weight chosen from the 1–100 range based on the importance of the considered DPC. The difference between the calculated and the targeted value of a DPC is squared to exclude larger deviations during the optimization process. The convergence of this approach is relatively quick (after 21 iterations, the difference between successive fitness function evaluation is smaller than a tolerance value of 10^{-7}) compared to the Monte Carlo approach. In the first column of Table 4-7, we present, for each elemental material, the value of the DPC obtained by CGOM through the optimization of the scaling parameters.

For the Monte-Carlo simulations, a statistical study is needed to extract the information about the DPCs. After fitting the distributions of each DPC by a Gaussian peak and using the

center of the peak x_c as an estimate of the DPC and the width w of the peak as the error, we present in Table VII the obtained values including the standard deviations (columns labeled MC). Furthermore, we present in Figure 4-5 the distribution of $(\Xi_d + \Xi_u/3 - a)^L$ for Ge, Si, and α-Sn. Ξ_u^{Δ} is obtained from the values of the splitting between Δ_2 and Δ_4 valley under the uniaxial strain, and b is obtained from the splitting of the valance-band level under uniaxial strain. Table 4-7 also lists different DPC values obtained experimentally or evaluated theoretically using either first principle calculations[197] or semi-empirical band structure method such as 30 band *k.p* method[198] or the $sp^3s^*d^5$ tight binding approach.[199]

Dilation deformation potential Ξ_d and a are related to absolute shifts of band extrema, which cannot be extracted from the ETB calculations with periodic boundary condition because the absolute position of an energy level in an infinite periodic crystal is not well defined.[200] Hence, in this work, we do not calculate the absolute deformation potential. Instead, we extract the linear combination $(\Xi_d + \Xi_u/3 - a)$ from the ETB by setting arbitrary value of the top of the valance band. In Table VII, we list the deformation potential for the valance and conduction bands extracted from ETB calculations. For the sake of comparison, data from literature are also shown. The valance band DPC, b, is negative. The uniaxial deformation potential $\Xi_u$is larger at the L minima band than at the Δ minima in all three elements implying that the conduction band at L is more sensitive to (111) strain than (001) strain. In addition, the linear combination of the dilation deformation potential $(\Xi_d + \Xi_u/3 - a)$ at the Δ minima is larger than at the L minima. For Ge and Si, there is an abundance of experimental and theoretical data for the DPCs because they were investigated extensively over the last few decades. However, for grey Sn, the data in literature are rather sparse making difficult the rigorous cross examination of our values. Nevertheless, one notes a fairly good qualitative agreement of the absolute hydrostatic deformation potentials close to the Fermi level at Γ with the calculations reported by Brudevoll et *al*.[187] Furthermore, using the CGOM, we obtained the corresponding scaling indices for each semiconductor thus allowing us to determine the DPC and the scaling index of the ternary alloy through a linear interpolation. The values of these scaling indices are listed in Table 4-6. The value of b_p is comparable to the b value presented in Table 4-7. To analyze rigorously the effect of strain on the band structure, we first focused on the direct-indirect crossover of the band gap of Ge. We have found that at 1.98% of

tensile strain Ge becomes direct (Figure 4-4), which agrees well with the 2% tensile strain measured by photoluminescence[201]

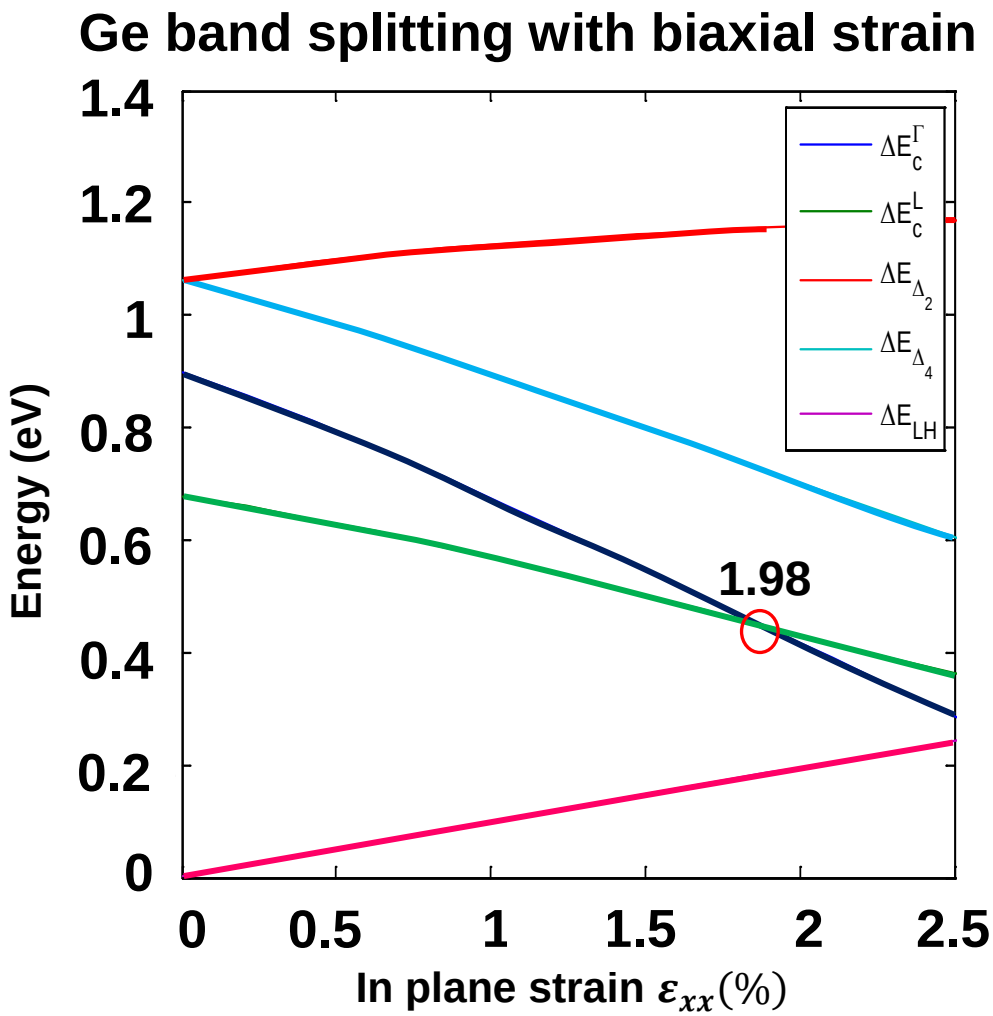

Figure 4-4: Energy dependence of the Γ, Δ_2, Δ_4, L, and LH extrema for Ge as a function of the in-plane biaxial strain. The lines correspond to the results given by the tight binding formalism using the CGOM.

and 1.9% obtained using first principle DFT calculations.[202] We have used the set of equations (4-4) as well as the estimated DPCs in order to plot the variation of band gap along each symmetry direction. The resulting plot of the energy gaps for tensile-strained as well as for relaxed Ge is summarized in Figure 4-4. This result validates the methodology described above, which can be now extended to address the effect of strain on the band structure of ternary alloys. Before doing so, we ought to identify two different types of strain. First, the biaxial strain generated epitaxially

during the growth of a ternary epilayer on Ge substrate. This type of strain depends on the composition of Si and Sn in the epilayer (i.e., $\varepsilon = \varepsilon(x, y)$). Second, the strain generated using post-growth processes that are independent of the composition. For instance, when the ternary layer is capped by local stressors or subjected to an external load thus the lattice parameter can vary independently of the composition. In the following, we address these two cases.

Table 4-6: The dimensionless scaling index $\eta(\mathrm{mn})$ used in the current calculations.

Material $\eta(mn)$	$\eta(pps)$	$\eta(pp\pi)$	$\eta(ss)$	$\eta(sp)$	$\eta(s^*p)$	b_p	F
Si	-1.9616	-2.1422	-4.2275	-0.8084	-2.1513	-2.3928	-0.731
Ge	-2.6842	-3.6842	-3.6842	1.3158	-3.6842	-2.0526	0.9737
Sn	-3.04286	-2.8571	-3.8571	2.8714	-2.1714	-2.5714	-0.8571

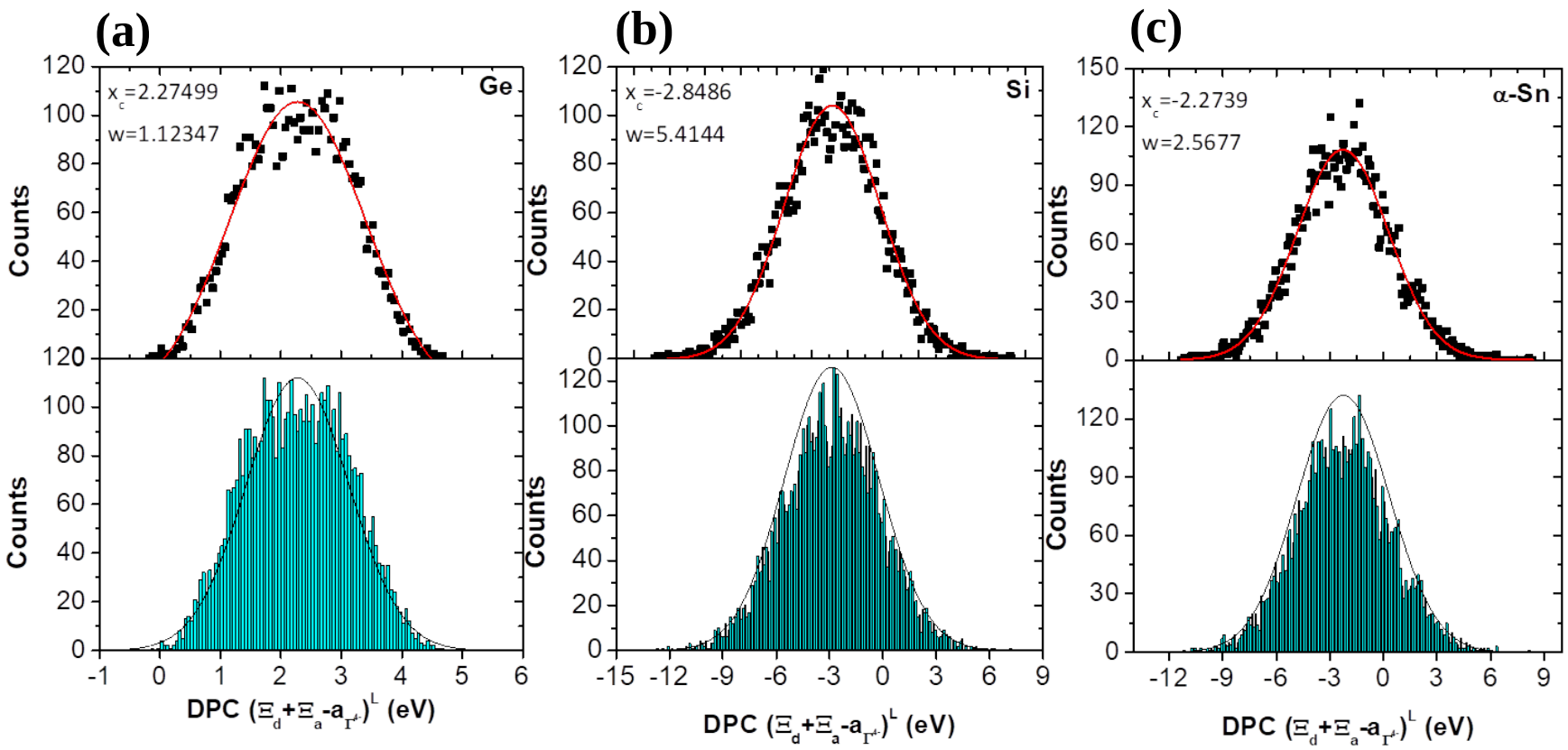

Figure 4-5: The value of the dilation $(\Xi_u + \Xi_d/3 - a)^L$ deformation potential constant obtained from the data set generated by Monte-Carlo simulations for Ge **(a)**, Si **(b)**, and α-Sn **(c)**.

Table 4-7: The deformation-potential constants of Ge, Si and α-Sn. The column labeled ''theor'' gives the values obtained by Van De Walle and Martin.[197] The column labeled MC show the stochastic Monte Carlo analysis performed in order to extract the DPC.

Parameters [eV]	**Si**						**Ge**						**α-Sn**			
	This Work	**Expt.**	**Theor.**	**$sp^3d^5s^{*}$ [l]**	**30 band k.p[k]**	**This Work (MC)**	**This Work**	**Expt.**	**Theor.**	**$sp^3d^5s^{*}$ [l]**	**30 band k.p[k]**	**This Work (MC)**	**This Work**	**Expt.**	**LDA[m]**	**This Work (MC)**
$\lvert b \rvert$	**2.05**	2.10[a],2.33[b], 2.27[c],2.4[e]	2.35	1.85	2.35	**2.35±1.45**	**2.1**	2.86[d],1.8[e]	2.55	2.48	2.55	**3.01±1.04**	**2.7**	NA	7.04	**3.5±2.40**
$(\Xi_d^\Delta + \Xi_u^\Delta/3 - a)$	**1.86**	1.5[a],2.5[j], 0.29[i], -0.18[k]	1.72	0.97	-0.18	**0.74±1.50**	**-1.86**	-2.9[g],-1.9[i], -5.75[j]	-1.31	-3.50	-2.4	**-0.79±3.3**	**2.11**	NA	1.11	**1.14±6.30**
$(\Xi_d^L + \Xi_u^L/3 - a)$	**-3.40**	-3.8[g],-3.12[f], -3.1[j]	-3.12	-2.61	NA	**-2.84±5.41**	**-3.5**	-2[e],-2.87[f], -0.83[j]	-2.78	-2.85	NA	**-2.27±0.85**	**-1.024**	NA	-0.514	**-2.25±2.60**
Ξ_u^Δ	**8.88**	8.6[e],9.2[f], 8.77[c] 9.29[i],10.5[j],9.1[k]	9.16	6.88	9.1	**9.63±3.20**	**9.46**	17.3[k], -9.75[j], 10.2[i]	9.42	6.50	17.3	**8.29±4.30**	**-2.87**	NA	-2.46	**-2.40±1.95**
Ξ_u^L	**15.20**	18[j],16.14[h]				**16.80±5.20**	**17.23**	16.8[j],15.13[h]				**15.23±4.30**	**-2.50**	-1.89	-2.14	**-2.2±1.1**
$a_{\Gamma_2^-}$	**-10.12**	NA	-5.1	NA	-5.1	**-9.18±4.12**	**-9.78**				-8.8	**-10±2**	**-7.65**	-3.3[n]	-7.77	**-7.21±3.10**

a. Reference [190]
b. Reference [203]
c. Reference [204]
d. Reference [205]
e. Reference [206]
f. Reference [197]
g. Reference [207]
h. Reference [106]
i. Reference [208]
j. Reference [209]
k. Reference [210]
l. Reference [199]
m. Reference [187]
n. Reference [211]

4.3.3 Mapping the band structure of strained $Ge_{1-x-y}Si_xSn_y$/Ge (001)

To begin with, we consider the following system: a layer of $Ge_{1-x-y}Si_xSn_y$ of a thickness h_1 is deposited on (001)-oriented Ge substrate of a thickness h_2. We assume all interfaces to be ideal, i.e., the bulk atomic structure of each semiconductor is maintained up to the interface. We will also neglect the effect of other imperfections such as impurities and dislocations. Thus, the strain tensor ε in each material can be described by:[106]

$$\varepsilon = \frac{a_{\parallel}}{a_0} - 1$$
$$a_{\parallel} = \frac{a_i G_i h_i + a_j G_j h_j}{G_i h_i + G_j h_j};\ i,j = \{Ge, GeSiSn\} \quad (4\text{-}11)$$

where a_0 denotes the lattice parameter of the substrate (Ge), h_i and h_j are the thicknesses of Ge and GeSiSn layers, respectively. $G_{i,j}$ $(i,j = \{Ge, GeSiSn\})$ is the shear modulus given by $G_{i,j} = 2\left(C_{11}^{i,j} + 2C_{12}^{i,j}\right)/\left(1 + D_{i,j}/2\right)$, where we use a linear interpolation to find the elastic constants (C_{11}, C_{12}) for the $Ge_{1-x-y}Si_xSn_y$ alloy. The constant $D_{i,j}$ depends on the elastic constants and on the growth direction. In the current work, only the (001) orientation is considered. Figures 4-6 and 4-7 summarize the effect of strain on $Ge_{1-x-y}Si_xSn_y$ band structure. Figure 4-6 displays the influence of strain on L and Γ symmetry and Figure 4-7(a) exhibits the band gap map of strained $Ge_{1-x-y}Si_xSn_y$ ternary alloy. The corresponding strain map is presented in Figure 4-7(b). The black continuous lines in Figure 4-7(a) show the transition between the tensile (positive strain) and compressive region (negative strain) for the ternary alloy. As in the unstrained case, the band gap shows the same qualitative behavior as a function of the composition: a widening when the Si composition increases and a narrowing when Sn composition increases. We also observe that the band gap becomes very sensitive to the composition in the compressive region as compared to the tensile region. Besides, the direct-indirect crossover is mainly modulated by the Γ and *L* symmetry points energy gaps. Interestingly, for $0 \leq x \leq 0.4$ and $0 \leq y \leq 0.2$, we note that tensile strain lowers the critical content of Sn needed to achieve a direct band gap semiconductor. The corresponding upper limit of direct band gap energies is 0.72 eV, which is higher than 0.43 eV in the case of relaxed alloys. We also found that the indirect-to-direct band gap transition crossover lines are given by $y = 0.605 \times x + 0.077$ and $y = 1.364 \times x + 0.107$ for strained and fully relaxed alloys, respectively.

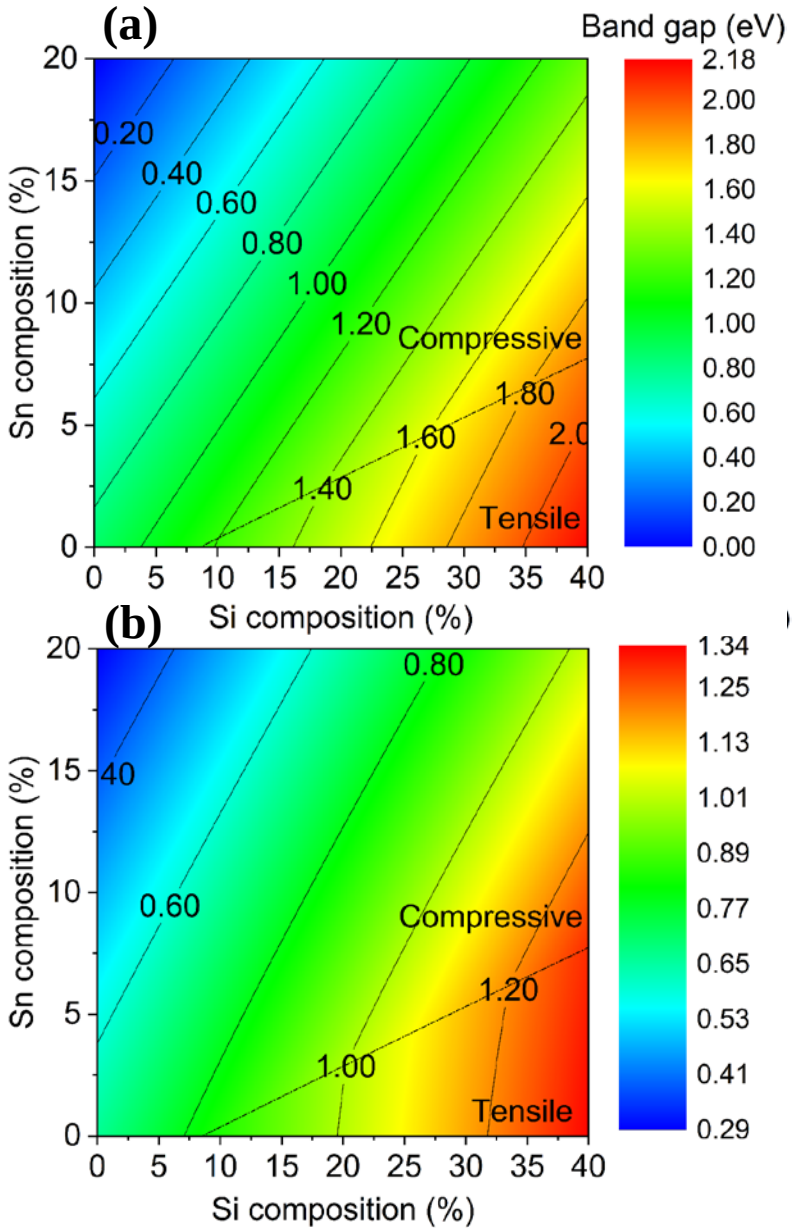

Figure 4-6: Strained band gap map of $Ge_{1-x-y}Si_xSn_y$/ (001)Ge with disorder along **(a)** L and **(b)** Γ symmetry points

Let us now examine the effect of strain on $Ge_{1-y}Sn_y$ alloys. The fully relaxed binary alloy presents an indirect-to–direct band gap transition at 11% Sn with a gap of 0.477 eV, as shown in Figure 4-3. However, under a biaxial tensile strain, the critical Sn content for the transition to a direct semiconductor reduces to 7.5% and the band gap becomes wider reaching 0.653 eV as shown in Figure 4-7(a). This figure displays the crossover lines of the strained (filled square) and unstrained

(open squares) ternary alloy: the composition of Sn in GeSn at which the transition from indirect to direct band gap occurs is shown as the intersection between the $x = 0$ axis and the empty or filled squares for strained and relaxed GeSn, respectively. Furthermore, in the indirect region we also note that there are two different sub-regions: the first is the L region and the second is the Δ_{100} region. The band gap in the L region is smaller than in the Δ_{100} region. We can also see that the rate of change of the band gap in the Δ_{100} region is much slower than in the L region, which imply more sensitivity to the strain effect in the L region when changing the Sn composition. The crossover line between the L and the Δ_{100} regions is shown by the empty circles in the Figure 4-7(a).

Table 4-8: Effect of strain on specific ternary alloy: three types of alloys are considered: a direct (alloy I), direct-indirect crossover compositions (alloy II), and indirect (alloy III). Figure 4-3 show explicitly the evaluated composition.

Alloy	**Si Composition x**	**Sn composition y**	$\boldsymbol{\varepsilon_{cross}}$ (%)	**Band gap [eV]**
I (Direct)	4%	21%	-0,668%	0,4100
II	4%	15%	0,152%	0,5489
III (Indirect)	10%	15%	0,810%	0,58

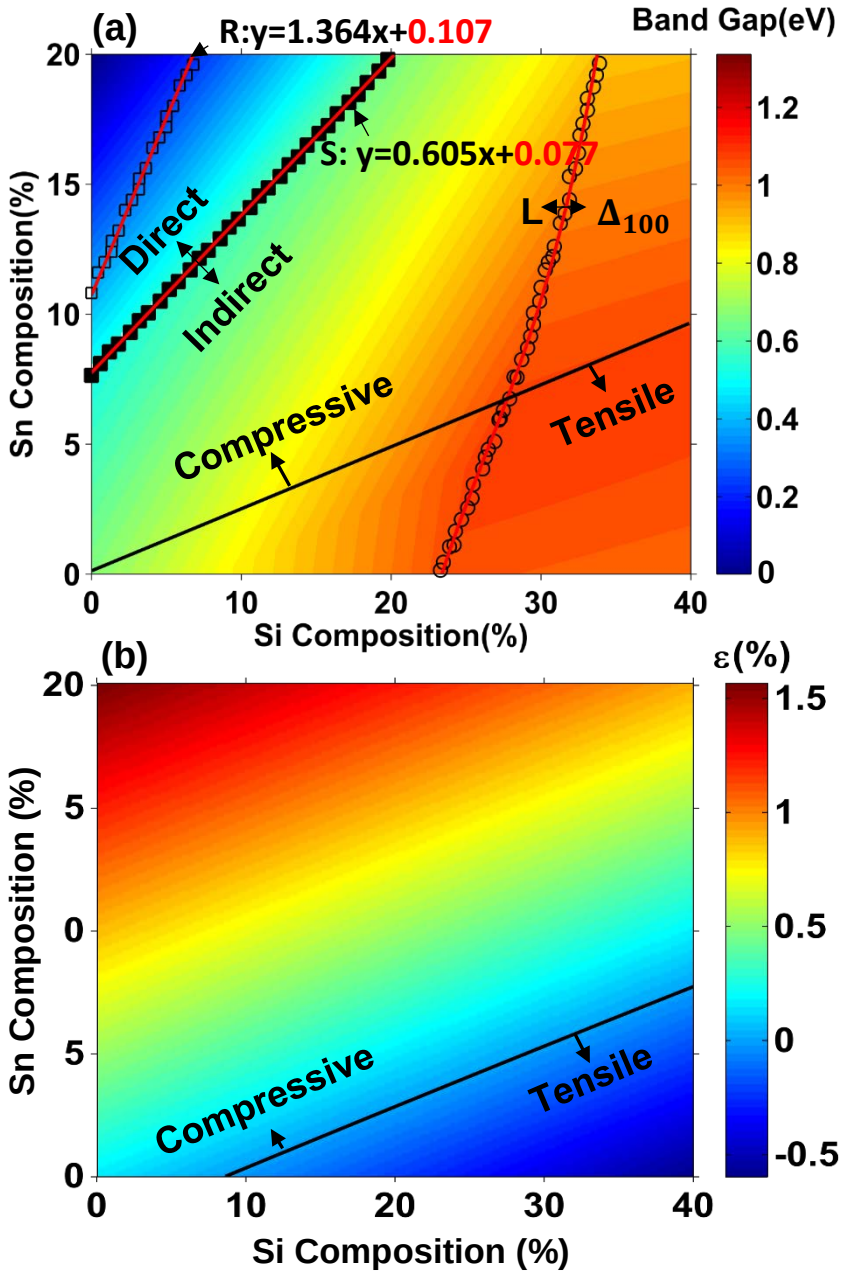

Figure 4-7: **(a)** Band gap map of strained $Ge_{1-x-y}Si_xSn_y$ layer. The black solid line is the transition between the tensile and compressive regions. The filled squares represent the crossover from direct to indirect for the strained ternary alloy and the corresponding equation is a linear fit in the (*x*, *y*) plane (**S** for strained alloy). However, the empty squares represent the direct to indirect transition line for the unstrained $Ge_{1-x-y}Si_xSn_y$ (**R** for relaxed alloys). The red line is a linear fit for both type of crossover to extract the Y-intercept. Finally, the empty circles represent the transition in the indirect region from the L-symmetry point to the X-symmetry. **(b)** The strain map of the $Ge_{1-x-y}Si_xSn_y$/ (001)Ge heterostructure as a function of Sn and Si contents.

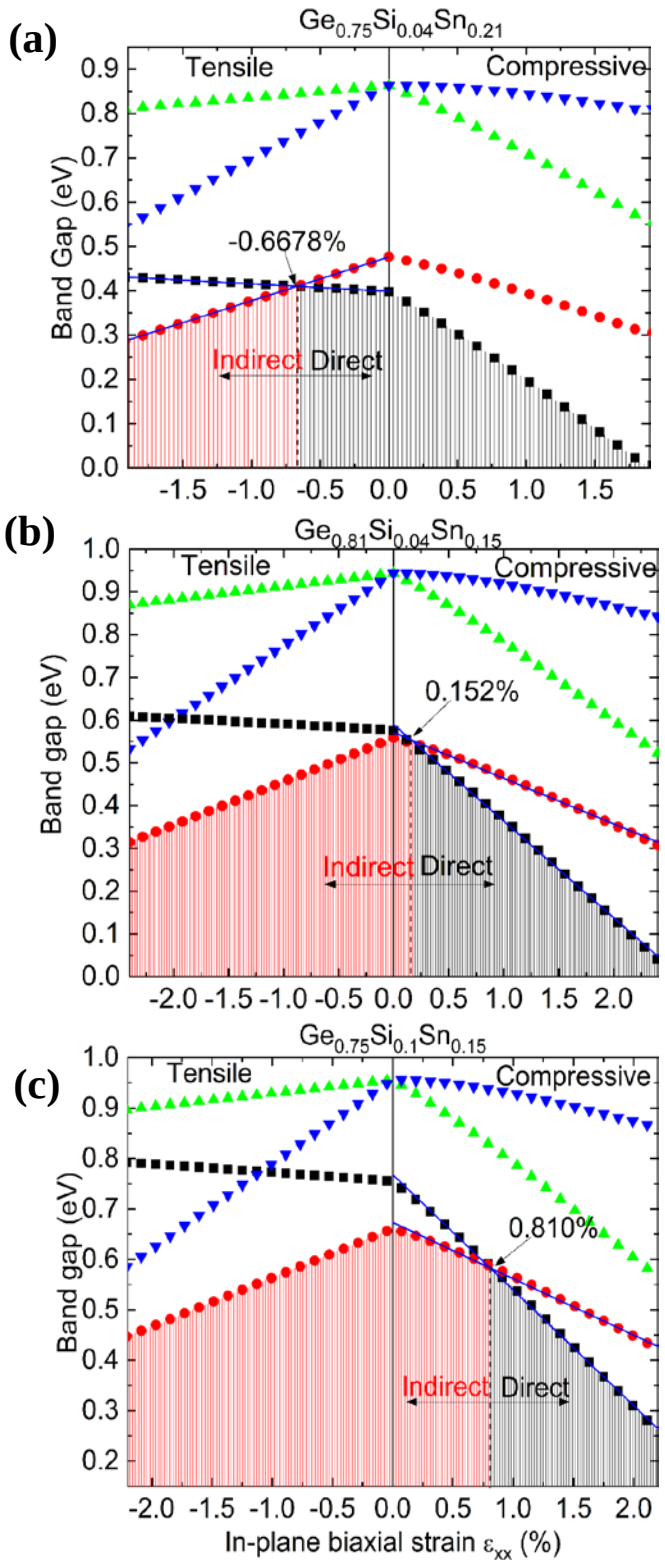

Figure 4-8: Band gap behavior as a function of strain along the symmetry points L, Γ and X for 3 $Ge_{1-x-y}Si_xSn_y$ ternary alloys with: (a) $(x, y) = (4\%, 21\%)$, (b) $(x, y) = (4\%, 15\%)$ and (c) $(x, y) = (10\%, 15\%)$

4.3.4 Effect of strain on ternary alloy direct and indirect band gap

The effect of strain at a fixed composition was also investigated. Herein, we opted to study the behavior of indirect to direct band gap transition as a function of strain and establish the band gap for each combination of x, y, and ε. In general, the calculated band structures indicate that the introduction of a tensile strain facilitates the transition to a direct band gap ternary semiconductor by reducing the concentration of Sn needed. In the following, we show the effect of strain on three different ternary alloys indicated by open circles in Figure 4-3. The first alloy (I) is located in the direct region with a composition of (4% Si, 21% Sn). The second alloy (II) is chosen near the direct to indirect crossover line with a composition of (4% Si, 15% Sn). Finally, an indirect bandgap alloy with a composition of (10% Si, 15% Sn) is chosen as the third alloy (III). Table 4-8 summarizes the calculated properties of the selected alloys and Figure 4-8 exhibits the influence of strain on their band structure and the important modification occurring on the band gap along the highest symmetry directions $\Gamma - L$ and $\Gamma - X$. It is noticeable that alloy I ($Ge_{0.75}Si_{0.04}Sn_{0.21}$) remains direct even under a compressive strain as high as -0.7%. For this alloy, the direct band gap varies between 0.1 and 0.41 eV in the strain range considered in this study. By decreasing the Sn content (y = 0.15) while keeping the Si content unchanged (x = 0.04) in the alloy II, a direct gap, in the 0-0.54 eV range, is only obtained under a tensile strain higher than 0.15%. This critical value increases further to 0.81% when the fraction of Si is increased to x = 0.1 in alloy III. Figure 4-9 (a) and (b) exhibit the behavior of ternary alloy band gap at a variable composition and at fixed values of tensile strain of 0.5% and 1.0%, respectively. The black solid lines indicate the indirect-direct transition crossover lines. For the sake of comparison, the crossover line for fully relaxed alloys is also shown. It is noticeable that, at a fixed Si content, tensile strain reduces the critical concentration of Sn needed to achieve a direct gap alloy. The corresponding Sn critical concentration is given by $y = 0.78 \times x + 0.0624$ and $y = 0.778 \times x + 0.029$ at a tensile strain of 0.5% and 1.0%, respectively. We also note that, for a fixed composition, the introduction of tensile strain increases the upper limit of the energy of the direct gap from 0.43 eV in fully relaxed alloys to 0.60 and 0.72 eV at 0.5 and 1.0%, respectively.

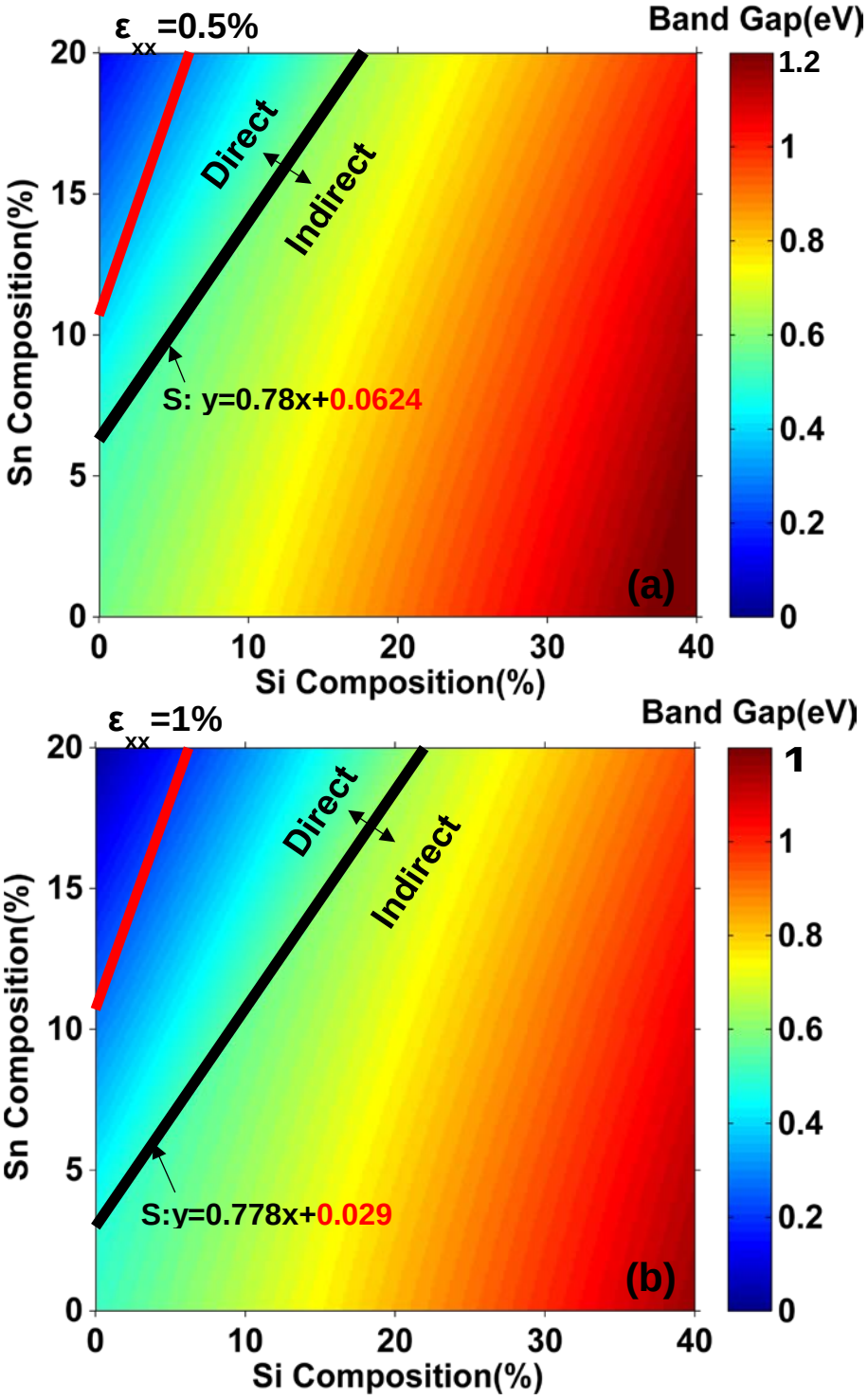

Figure 4-9: Band gap map of GeSiSn/ (100)Ge system for a strain independent composition where the Si and α-Sn compositions vary from 0 to 40% and 0 to 20% respectively and the strain values are equal to **(a)** 0.5% and **(b)** 1.0%. The red lines represent the relaxed direct to indirect crossover, whereas the black continuous lines are the corresponding strained crossover lines.

4.4 Conclusion

In summary, investigations of the effects of composition and strain on the band structure of Sn-containing group IV semiconductors were presented by adapting the second nearest neighbors empirical tight binding method (2NN-sp3s*). For this, a theoretical framework to map the changes in band gap energy and directness as a function of both composition and strain was developed. This method is based on an accurate evaluation of the deformation potential constants of Ge, Si, and α-Sn using a stochastic Monte-Carlo approach as well as a gradient based optimization method (conjugate gradient method). Furthermore, we developed a new and efficient differential evolution method through which the experimental effective masses and band gaps are accurately reproduced. Based on this, we found that a precise analysis of the band structure as well as an accurate identification of the indirect-to-direct bandgap transition in $Ge_{1-x-y}Si_xSn_y$ alloys is obtained by incorporating the effect of substitutional disorder. Moreover, we also elucidated the mutual influence of composition and $Ge_{1-x-y}Si_xSn_y$/Ge (001) lattice mismatch-induced biaxial strain on the band structure of $Ge_{1-x-y}Si_xSn_y$ semi-conductors. For $0 \leq x \leq 0.4$ and $0 \leq y \leq 0.2$, we found that tensile strain lowers the critical content of Sn needed to achieve a direct band gap semiconductor. The corresponding band gap energies are below 0.72 eV. In fully relaxed alloys, the direct band gap energy is located below 0.43 eV. We also found that the indirect-to-direct band gap transition crossover lines are given by $y = 0.605 \times x + 0.077$ and $y = 1.364 \times x + 0.107$ for strained and fully relaxed alloys, respectively. Finally, the sole effect of strain at a fixed composition was also investigated confirming that tensile strain facilitates the transition to a direct gap semiconductor, whereas the transition requires higher content of Sn under a compressive strain. Our results indicate that the interplay between composition and strain effects provide a rich playground to tune over a broad range the band gap and lattice parameter in group IV semiconductor, which provides a wealth of opportunities to create an entirely new class of heterostructures, low-dimensional systems, and Si-compatible devices. The next step involves studying a type-I group-IV based radial heterostructure by evaluating the conduction and valence band offset and using them to solve the Schrödinger equation in a cylindrical geometry to quantify the effect of the dimensionality of the structure on the distribution of the hole and electron carriers.

CHAPTER 5 ARTICLE 2: OPTICAL AND ELECTRONIC PROPERTIES OF GeSn AND GeSiSn HETEROSTRUCTURES AND NANOWIRES

This chapter has been published in a conference proceeding. The full reference is below: ***Attiaoui A*** *and Oussama M (2014) Optical and electronic properties of GeSn and GeSiSn heterostructures and nanowires ECS Transactions, The Electrochemical Society, vol 64, pp 869–79. doi: 10.1149/06406.0869ecst*

Germanium-silicon-tin ($Ge_{1-x-y}Si_xSn_y$) and germanium-tin ($Ge_{1-y}Sn_y$) alloys have been attracting a great deal of attention in recent years as a new and rich platform to expand the capabilities of Si-based technologies.[151–153] Implementing these Sn-containing group IV alloys remains very challenging from materials perspective due to the low solubility (<1 at.%) of Sn in Si and Ge. Nevertheless, the recent progress in low-temperature chemical vapor deposition alleviates some of these difficulties leading to the growth of high-quality monocrystalline[154] layers thus setting the ground for the development of a new generation of group IV-based devices.[155] Herein, the electronic structure of strained and relaxed $Ge_{1-x-y}Si_xSn_y$ ternary alloys semiconductors will be discussed by using a rigorous semi-empirical second nearest neighbor tight binding sp^3s^* method that incorporates the effect of substitutional disorder. We already showed in the previous chapter that the composition of α-Sn at the direct-to-indirect crossover of the ternary alloy decreases from 11% in a fully relaxed alloy to 7% in tensile strained alloy (for a strain value of 0.71%).[40] The interesting properties of Sn-containing group IV alloys can be enhanced further by introducing them in the fabrication of nanoscale heterostructures such as core-shell nanowires. For instance, this nanowire structure provides a unique advantage by allowing the confinement of two-dimensional electron gases (2DEGs) at the semiconductor-semiconductor heterojunction interface which can enhance carriers' recombination. In this perspective, n-type doping densities ranging from 10^{16} to $10^{17}cm^{-3}$ will be investigated, assuming a uniform doping density throughout the nanowire with a Ge core radius ranging from 10 nm to 40 nm with a fixed 20 nm shell layer of $Ge_{1-y}Sn_y$ (y=10% and 14%).

This chapter is organized as follows. The first section briefly resumes our findings of the electronic structure of strained and relaxed $Ge_{1-x-y}Si_xSn_y$ ternary alloys semiconductors, which was developed in detail in the previous chapter. The second section shows the effect of free carriers doping concentration and core radius on electron localization, carried out using the self-consistent resolution of the Poisson-Schrödinger equation.

5.1 Band gap maps for strained and relaxed ternary alloy group IV semiconductors $Ge_{1-x-y}Si_xSn_y$

Sn-containing group IV semiconductors create the possibility to independently control strain and band gap thus providing a wealth of opportunities to develop an entirely new class of low dimensional systems, heterostructures, and silicon-compatible electronic and optoelectronic devices. With this perspective, a detailed investigation of the band structure of strained and relaxed $Ge_{1-x-y}Si_xSn_y$ ternary alloys using a semi-empirical second nearest neighbors' tight binding method is presented. This method is based on an accurate evaluation of the deformation potential constants of Ge, Si, and α-Sn using a stochastic Monte-Carlo approach as well as a gradient based optimization method. Moreover, a new and efficient differential evolution approach is also developed to accurately reproduce the experimental band gaps[40]. Based on this, we elucidated the influence of lattice disorder, strain, and composition on $Ge_{1-x-y}Si_xSn_y$ band gap energy and directness.

An accurate calculation of the band gap of a given semiconductor is an important and a laborious task. There exists a multitude of approaches that answer this problem. DFT is the-state-of-the-art method to address this issue. Yet the task is to choose the most efficient method based on its computational power and accuracy. Therefore, the second nearest neighbors sp^3s^* tight binding approach[128,212] (2NN-sp^3s^*) was chosen. Furthermore, after verification of the validity of the 2NN-sp^3s^* model by estimating the elemental semiconductors band gaps, it becomes possible to evaluate the band gaps for the $Ge_{1-x-y}Si_xSn_y$ ternary alloys using the universal tight binding method based on a modified pseudocell (MPC) initially introduced by Shim et *al*. to investigate III-V compound semiconductors.[173] The MPC is a periodic virtual cell describing the alloy as an effective perfect bulk system, in which the alloy $Ge_{1-x-y}Si_xSn_y$ is defined as consisting of three fictive atoms Ge, Si, and α-Sn residing on an atomic site. Thus, three possible unit Ge, Si, and α-Sn are possible with mixing probabilities of 1-*x*-*y*, *x*, and *y*, respectively. The effect of disorder

will be included by considering that each unit is disordered by the presence of the other two atoms. The alloy Hamiltonian can thus be written under the virtual crystal approximation as: $H_{Ge_{1-x-y}Si_xSn_y} = (1-x-y)H_{Ge} + xH_{Si} + yH_{Sn}$.

Figures 4-3 and 4-7 summarize the effect of relaxed and strained $Ge_{1-x-y}Si_xSn_y$ band structure. Figure 4-3 exhibits the map of the crossover between direct to indirect band gaps for relaxed ternary alloys. In Figure 4-3, the effect of disorder on the band gap at the highest symmetry points was incorporated. We note that when the composition of Sn increases, the band gap energies decrease, whereas when the concentration of Si increases, the band gap becomes wider. Whereas, Figure 4-7 exhibits the band gap map of strained $Ge_{1-x-y}Si_xSn_y$ ternary alloy. The black continuous lines in Fig 2 show the transition between the tensile (positive strain) and compressive region (negative strain) for the ternary alloy. As in the unstrained case, the band gap shows the same qualitative behavior as a function of the composition. Additionally, the band gap becomes very sensitive to the composition in the compressive region as compared to the tensile region. Besides, the direct-indirect crossover is mainly modulated by the Γ and *L* symmetry points energy gaps. Interestingly, for $0 \leq x \leq 0.4$ and $0 \leq y \leq 0.2$, tensile strain lowers the critical content of Sn needed to achieve a direct band gap semiconductor. After acquiring more information on the electronic properties of the relaxed and strained GeSiSn ternary alloy through the 2NN-sp^3s^* code, it now becomes possible to study the merits and demerits of using GeSiSn in practical application. For instance, we will focus on nanowire (NW) structure as a building blocks for photovoltaic cells. For that matter, the effect of doping concentration and the radius of the core on the spatial localization of electrons and holes densities inside the core-shell nanowire will be analyzed.

5.2 GeSiSn based nanowires heterostructures

Initially, in order to map the electron and hole localization in the core-shell NW (CSNW) dependency with the doping concentration and the radius of the core, a brief overview [213,214] of the method used to evaluate this property will be presented. The free electron or hole gas of a modulation-doped CSNW is obtained within the effective mass approximation where the system Hamiltonian is expressed in cylindrical coordinates using a finite difference technique[215] for the CSNW where the core and the shell are made of different alloys. We solved self-consistently the Schrödinger (5-1) and Poisson (5-2) equations until convergence, which are presented below

$$\left[-\frac{\hbar^2}{2}\nabla_i.\frac{1}{m_e^*(r_i)}.\ \nabla_i + V_n(\boldsymbol{r}_i) + V_{CB}(\boldsymbol{r}_i) + V_{e-e}(\boldsymbol{r}_i)\right]\Psi_i^e(\boldsymbol{r}_i) = \epsilon_i^e\Psi_i^e(\boldsymbol{r}_i)$$
$$\left[-\frac{\hbar^2}{2}\nabla_i.\frac{1}{m_h^*(r_i)}.\ \nabla_i - V_p(\boldsymbol{r}_i) - V_{VB}(\boldsymbol{r}_i) + V_{e-e}(\boldsymbol{r}_i)\right]\Psi_i^h(\boldsymbol{r}_i) = -\epsilon_i^h\Psi_i^h(\boldsymbol{r}_i) \quad (5\text{-}1)$$

$$\rho(\boldsymbol{r}) = e[n_h(r) - n_e(\boldsymbol{r}) + \rho_D(\boldsymbol{r}) - \rho_A(\boldsymbol{r})]$$
$$\nabla_r[\varepsilon(\boldsymbol{r})\nabla_r V(\boldsymbol{r})] = -\frac{\rho(r)}{\varepsilon_0} \quad (5\text{-}2)$$

where V_n and V_p are the electrostatic potential generated by electrons and holes free carrier respectively, V_{cb} and V_{vb} are the local conduction and valance band edges, V_{e-e} is the Poisson potential due to electron-electron interactions, $n_h$and n_e in (5-2) are the densities of free electrons and holes $\rho_A$and ρ_D are the ionized acceptors and donors and the electrostatic potential is found by solving the second equation in (5-2). A self-consistent solving routine is necessary to extract the electron/hole density in the CSNW. To do so, Dirichlet boundary conditions were used where we set $\Psi_i(r = r_s) = 0$ and $V_n(r_s) = V_{CB}(r_s) = V_{e-e}(r_s) = 0$. Next, a uniform n-type doping (free electron) density n_D through the NW was used. The temperature, which is a physical parameter that can be incorporated via the Fermi-Dirac distribution, was also included in the code. Table 5-1 shows the important physical parameters used in our self-consistent calculation.

It is important to mention that the transition from direct to indirect band gap in relaxed semiconductor occurs, as shown in the Figure 4-3, around 11% of Sn. By increasing the Sn composition, a crossover from a direct Γ to an L indirect semiconductor occurs. For this reason, Table 5-1 presents two different values for the band gap, the conduction band offset as well as the effective mass of $Ge_{1-y}Sn_y$.

Next, the Schrödinger-Poisson equation was solved self-consistently until convergence and we find the Fermi level at each iteration via the charge neutrality condition.[213]

To quantify the spatial distribution of electron and hole in the CSNW, a dimensionless core-normalized variance of the electron density $\langle r^2 \rangle$ was introduced, defined as

$$\langle r^2 \rangle = \frac{\int r^2 n_e(r) dS}{r_c^2 \int n_e(r) dS} \tag{5-3}$$

where r_c is the core radius, $n_e(r, \theta)$ is the electron density distribution and S is the cross-sectional area of the NW. $\langle r^2 \rangle$ measures the relative spread of the electron density and is bounded between 0 and r_{shell}^2 / r_c^2. A value of $\langle r^2 \rangle$ less than 1 indicate a localization within the core, whereas value larger than 1 represents confinements in the shell.

Table 5-1: Material parameters used in our self-consistent calculations. E_g is the band gap, ΔE_c is the conduction band offset, m^* is the relative electron effective mass which is taken from Ref. [49] (the numerical value aren't presented because they are defined by a numeric cubic spline), and ε_r is the relative static dielectric constant.

Material parameters	**Ge**	**$Ge_{1-y}Sn_y$**
$E_g(eV)$	0.7437[a]	$\begin{cases} 0.665 - 1.848y + 1{,}275y^2 \ if \ y < 11\% \\ 0.796 - 3.035y + 1.826y^2 \ if \ y > 11\% \end{cases}$[b]
$\Delta E_c(eV)$		$\begin{cases} 0.0001 - 3.1481y + 1.94y^2 \ if \ y > 11\% \\ -0.41y - 0.11y^2 \ if \ y < 11\% \end{cases}$[b]
$m^* \ (/m_0)$	0.038[a]	$\begin{cases} m_e^{\Gamma} \ if \ y > 11\% \\ m_e^{L} \ if \ y < 11\% \end{cases}$[c]
ϵ_r	16[a]	$13.18 - 3.12y$[a]

a. Reference.[174]

b. Reference [147]

c. Reference [49]

The following system is considered: a $Ge_{0.90}Sn_{0.10}$/Ge core-shell nanowire. Then, for different core radii and shell thickness in the 10-40 nm range, the electron spatial distribution will be evaluated inside the CSNW. In Figure 5-1 the confinement of electron is mapped versus the radius of the Ge core and the doping concentration of free carrier, for a fixed shell thickness of 20 nm and a fixed

temperature of 200K. Furthermore, in the inset, the conduction and valance band offset for the $Ge_{0.90}Sn_{0.11}$/Ge system, which will give us a better overview of the possible localization of electron in this type I heterostructure is shown. We conclude from Figure 5-1 that the above the doping concentration of 5×10^{16} cm^{-3}, electrons are confined in the core. This change in localization of electron in core/shell nanowire, corresponds to a transition where the electron gas in the middle of the core becomes strongly localized in the heterojunction core/shell interface or beyond.

Then, the Sn composition is increased above 11% so that the $Ge_{1-y}Sn_y$ binary alloy becomes a direct gap semiconductor. This will induce a change in the conduction band offset, which will have a direct effect on the localization of electron in the nanowire. Figure 5-2 presents the obtained results. While analyzing the electronic localization in CSNW, for 11% Sn composition, a different behaviour was observed from the indirect gap GeSn semiconductor, presented beforehand. In fact, from the value of $\langle r^2 \rangle$, which are below 1, the electrons are confined in the core. Although $\langle r^2 \rangle$ is less than 1, Figure 5-2 shows that the localization of electron in the core-thus the electron density-depends on the doping concentration and the core/shell radii. In fact, a higher value of $\langle r^2 \rangle$ can be interpreted as a higher electron density.

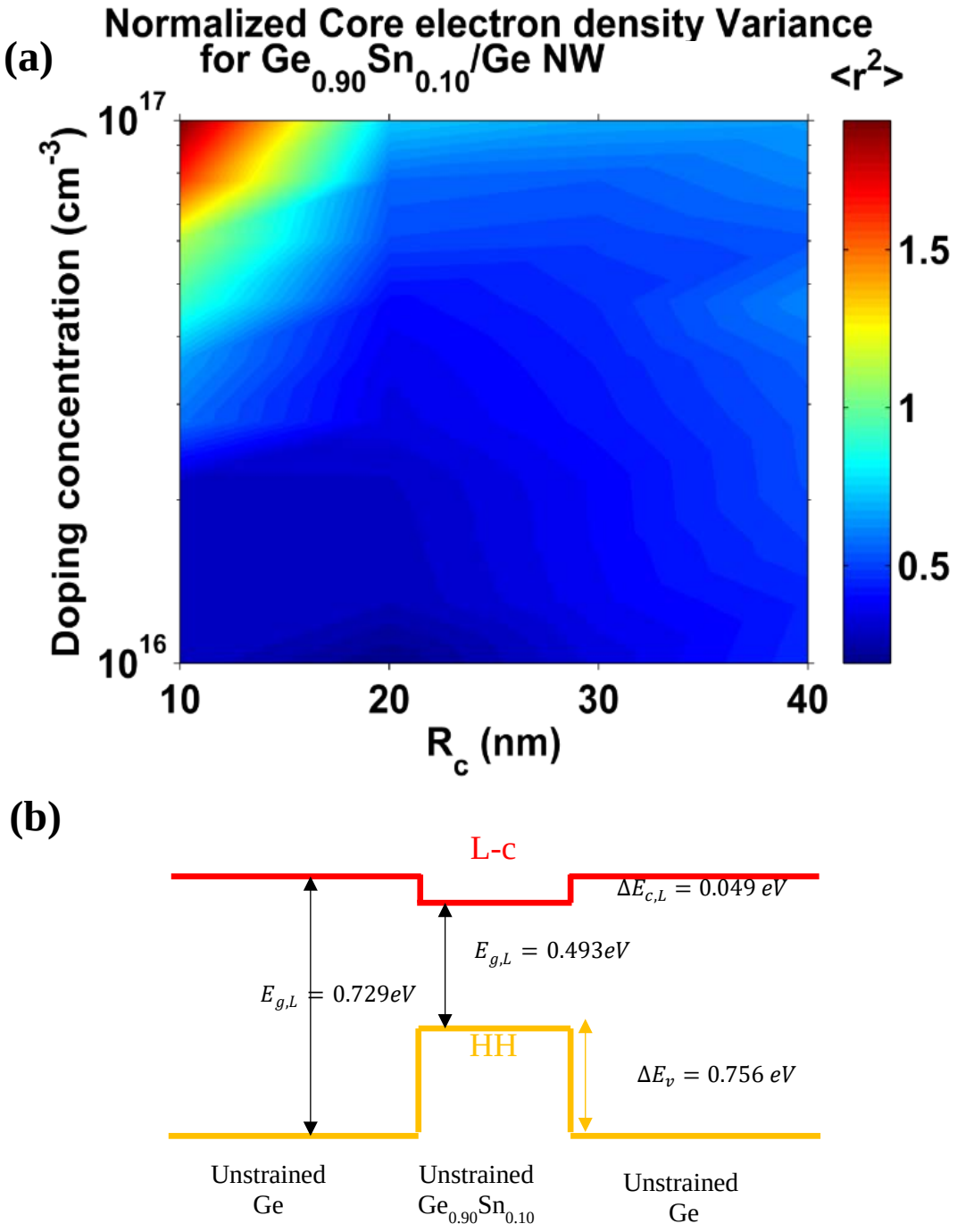

Figure 5-1: **(a)** Dimensionless core-normalized variations of the electron density as a function of the $Ge_{0.9}Sn_{0.1}$ core radius and doping density for a Ge shell of 20 nm. **(b)** This figure shows the conduction band offset for a type I heterostructure. Note that for Sn composition below 11%, GeSn is an direct band gap semiconductor[40,147].

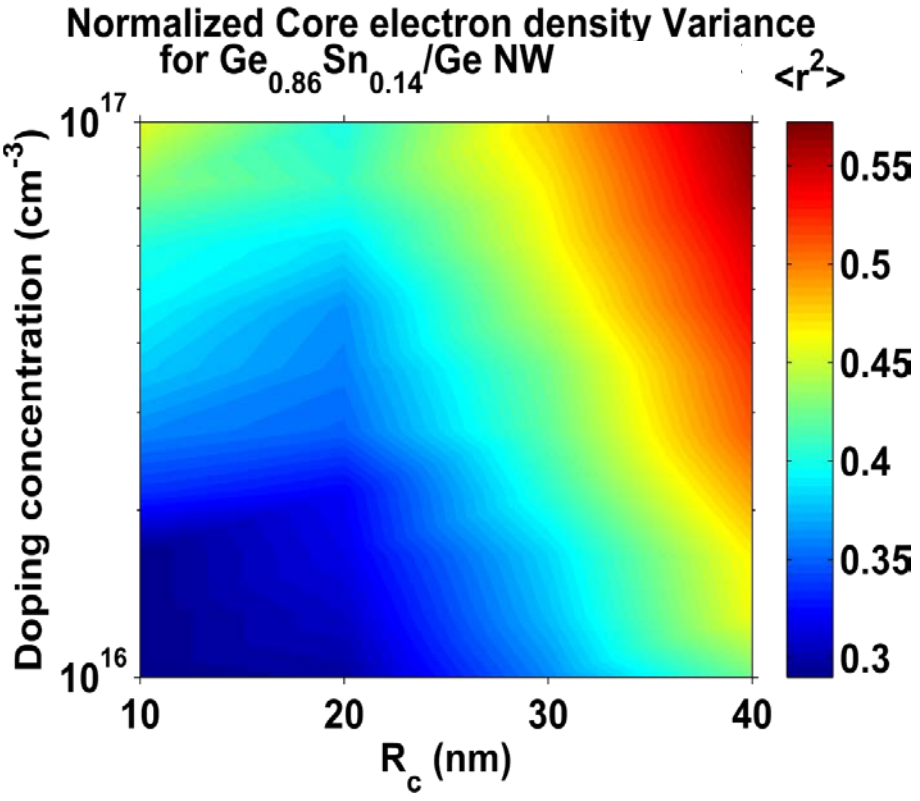

Figure 5-2: Dimensionless core-normalized variations of the electron density as a function of the $Ge_{0.86}Sn_{0.14}$ core radius and doping density of electron free carriers for a Ge shell of 20 nm. The inset show the conduction band offset for a type I heterostructure. Note that for Sn composition above 11%, GeSn is an L-indirect band gap semiconductor

5.3 Conclusion

To summarize, detailed investigations of the effects of composition and strain on the band structure of Sn-containing group IV semiconductors were undergone by adapting the second nearest neighbors empirical tight binding method (2NN-sp^3s^*). For this, we developed and employed a theoretical framework to map the changes in band gap energy and directness as a function of both composition and strain. This method is based on an accurate evaluation of the deformation potential constants of Ge, Si, and α-Sn using a stochastic Monte-Carlo approach as well as a gradient based optimization method (conjugate gradient method). Furthermore, we developed a new and efficient differential evolution method through which the experimental

effective masses and band gaps are accurately reproduced which allowed us to accurately include the effect of strain on the ternary semiconductor. Next, to study group IV core-shell nanowire system, we solved self-consistently the Schrödinger-Poisson equation for the $Ge_{1-y}Sn_y$/Ge core-shell NW system for two different Sn compositions where there is either a direct binary alloy (x<11%) or an indirect one (x>11%). Moreover, the effect of free electron carrier doping on the spatial localization of electron inside the cylindrical core-shell NW was studied. An interesting finding is the possibility to tune the electronic density localization inside the nanowire by controlling the doping concentration and the core and shell radii. A possible implication of this finding is to have a better estimation for the doping concentration and the geometrical properties of the NW to enhance the recombination process in an optoelectronic or photovoltaic device. Furthermore, in the following chapter, we will investigate in detail the CSNW structure as a building block for light absorption and scattering, which can be implemented in a multitude of applications such as solar cell junction or photodetectors.

CHAPTER 6 ARTICLE 3: EXTREME IR ABSORPTION IN GROUP IV -SiGeSn CORE-SHELL NANOWIRES

This chapter has been published in the journal of Applied Physics. Some sections were removed and put in the chapter 3 methodology (section 3.1.2). The full reference is: ***Attiaoui A****, Wirth S, Blanchard-Dionne A-P, Meunier M, Hartmann J M, Buca D and Moutanabbir O 2018 Extreme IR absorption in group IV-SiGeSn core-shell nanowires J. Appl. Phys.* ***123*** *223102. doi: https://doi.org/10.1063/1.5021393*

Engineering light absorption, and scattering in group IV semiconductors has been a powerful paradigm to implement innovative and high performance devices for solar cells[216], photodiodes, photodetectors, and plasmonics[217,218], to name a few. Of particular interest is developing cost-effective and high efficiency photovoltaic cells which rely crucially on the availability of affordable materials that can efficiently absorb light and convert it into charge carriers. Within this broad context, silicon (Si) has been the material of choice due to its cost-effectiveness and its wide use in semiconductor technologies. However, despite its attractive electronic and material characteristics, Si has rather poor optical properties relative to its mainstream semiconductor counterparts due to its indirect band gap and limited light absorption especially in the near-infrared region (NIR) and beyond thus limiting the efficiency of Si-based solar cells. Consequently, electricity generated by Si solar cells, which currently make up over 90% of the photovoltaic market, is still 2-3 times more expensive than that from conventional fossil fuels which hinders their wide-scale adoption.[219] In order to enhance the performance of Si cells, a variety of strategies for light trapping through surface texturing and coating have been recently reported. [220,221] Among these strategies, nanoscale structures such as nanowires (NWs) are emerging as effective building blocks to enhance Si optical properties to enable a broad range of optoelectronic devices[222–224], such as photovoltaic cells[142,225–227], photodetectors[228–230], meta-materials[231–233] and thermal emitters.[234] In this work, we demonstrate that tin (Sn)-containing group IV ($Ge_{1-x-y}Si_xSn_y$) core-shell nanowire (CSNW) structures are effective in enhancing NIR light absorption in Si-based structures. We also

demonstrate that this additional Sn-containing shell layers enhance the optical properties of germanium nanowires (GeNWs).

$Ge_{1-x-y}Si_xSn_y$ is an emerging semiconductor system providing two degrees of freedom for band structure engineering, namely, alloying and strain. This ability to independently manipulate strain and lattice parameter is central to engineering novel, group IV, low-dimensional systems and heterostructures in a similar fashion to the mature III-V materials. Moreover, unlike the indirect band gap of Si and Ge, a direct band gap semiconductor can be achieved using Sn-containing alloys thus providing a promising path towards Si-compatible efficient devices for emission and detection of light.[70,154] The nature of the band gap and its energy depend on the composition of the alloys.[40,235–237]

In the following, we begin by studying the structural properties and crystalline quality of the $Ge_{1-x-y}Si_xSn_y$ layers at variable composition. Next, the optical properties of these layers are investigated using spectroscopic ellipsometry. The obtained optical properties of the analyzed layers were introduced to a Mie-scattering formalism using cylindrical CSNWs to evaluate the effects of the NW dimensions on the scattering and absorption properties. Then, the optical antenna effects will be demonstrated in individual SiNWs and GeNWs, which form the basic building blocks of the proposed CSNWs structures. Next, their absorption efficiencies will be optimized by engineering the best possible match between the absorption spectrum of the wires and visible range (0.4-0.75 μm) as well as the Near-Infrared (NIR) range (0.75-1.4 μm). In addition, as a figure of merit of absorption efficiency, the photocurrent of different group IV $Ge_{1-x-y}Si_xSn_y$ based films and nanowires structures will be analyzed: Si/$Ge_{1-x-y}Si_xSn_y$ CSNWs, Ge/$Ge_{1-x-y}Si_xSn_y$ CSNWs, and CSNWs wrapped in non-absorbing, anti-reflection coating (ARC) layers. Using these structures, an extremely-large absorption and scattering enhancements as compared to SiNWs, GeNWs, and thin films can be achieved.

6.1 Experimental and Theoretical Details

6.1.1 Growth of $Ge_{1-x-y}Si_xSn_y$ samples

These layers were grown using a metal, cold-walled, reduced pressure chemical vapor deposition AIXTRON TRICENTR® (RP-CVD) for 200/300 mm wafers.[70] The growth of $Ge_{1-x-y}Si_xSn_y$ layers was performed on Si (100) wafers using low-defect density Ge virtual substrates.[238–240]

The epitaxial layers were grown using Si_2H_6, Ge_2H_6 (10% diluted in H2), and $SnCl_4$ precursors using N_2 as a carrier gas, which warrant reasonable growth rates at temperatures in the 350-475 °C range. The $Ge_{1-x-y}Si_xSn_y$ layers were grown with Si and Sn concentrations in the range of 4-20% and 2-12%, respectively. Prior to Raman investigations, the composition and structural properties of $Ge_{1-x-y}Si_xSn_y$/Ge/Si layers were characterized using Rutherford backscattering spectrometry (RBS), xray reciprocal space mapping (RSM), and transmission electron microscopy (TEM).

6.1.2 Structural and Optical Properties

Detailed investigations of structural and optical properties of $Ge_{1-x-y}Si_xSn_y$ semiconductors are still in their infancy despite their scientific and technological importance. Herein, to extract the optical properties needed for a more accurate theoretical treatment of light-NW interaction, spectroscopic ellipsometry was employed to characterize $Ge_{1-x-y}Si_xSn_y$ thin layers. Spectroscopic ellipsometry was employed to quantify the optical constant of the material. A detailed description of the principal of spectroscopic ellipsometry was developed in section 3.2 of Chapter 3. Figure 6-1(a, b) exhibits high-resolution Scanning Transmission Electron Microscopy (STEM) images near the $Ge_{1-x-y}Si_xSn_y$/Ge interface for two different Sn and Si compositions [(x, y) = (12%, 4%) and (4%, 12%), respectively]. These figures clearly indicate the possibility of an epitaxial growth of GeSiSn on a Si substrate. X-ray reciprocal space mapping (not shown) confirmed that the grown layers are strained with an out-of-plane tetragonal distortion, typical to pseudomorphic growth, in agreement with the electron diffraction patterns (Figure 6-1(c, d), inset). The latter also demonstrate the absence of Sn precipitates despite the Sn content exceeds by several factors its equilibrium solubility (<1.1 at. %) which is a characteristic of metastable growth techniques.[69]

Next, the optical properties of the grown films were investigated at room temperature using Variable-Angle Spectroscopic Ellipsometer (VASE). Using the visible-UV instrument, the dielectric function of our samples was determined from 1 to 5 eV with 0.01 eV steps based on measurements at four different angles of incidence. The ellipsometric data processing is elaborated in the section 3.2.3 of Chapter 3. After extracting the optical constants, the complex refractive index was incorporated into a Lorentz-Mie formalism to quantify the absorption, scattering, and extinction efficiencies of CSNW, as it will be shown in the following section. The $\boldsymbol{N}(E)$ spectra resulting from the modeling of the two spectroscopic parameters (Ψ, Δ) are displayed in Figure 6-2 which express the amplitude ratio and phase difference between p- and s-polarizations,

respectively. In this figure, the obtained spectra are presented for the binary alloy semiconductor $Ge_{1-y}Sn_y$ (top) and the ternary alloy $Ge_{1-x-y}Si_xSn_y$ (bottom), where the composition of Sn has been measured by EDX and Rutherford backscattering spectrometry.[157]

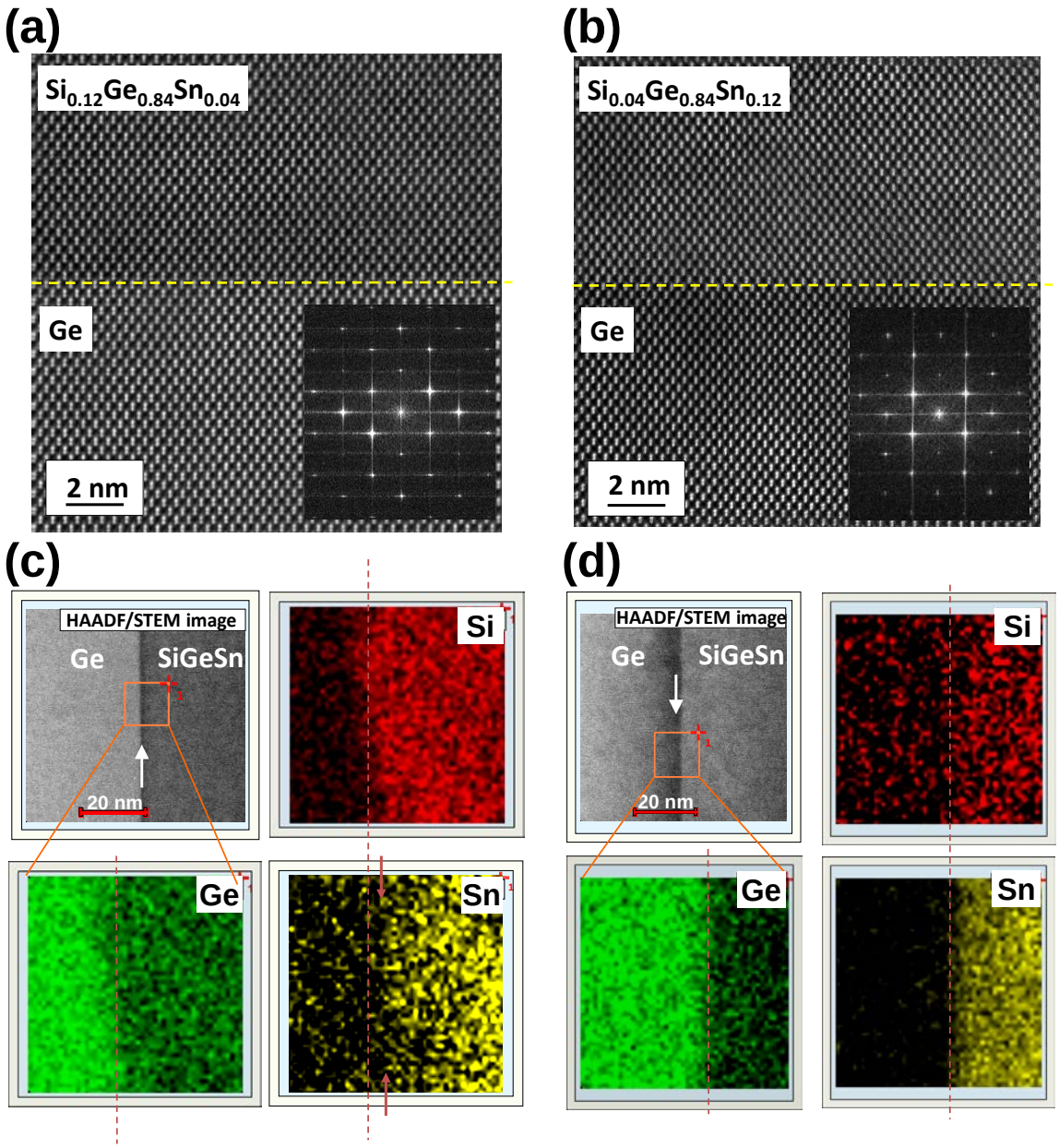

Figure 6-1: High Angle Annular Dark Field Scanning Transmission Electron Microscopy (HAADF/STEM) image of $Ge_{0.84}Si_{0.12}Sn_{0.04}$ **(a)** $Ge_{0.84}Si_{0.04}Sn_{0.12}$ **(b)** layers grown on Ge virtual substrates. Note the absence of dislocations or extended defects in the ternary layer or at the interface. The corresponding diffraction patterns measured at the interface are shown as inset figures in (a) and (b) confirming the high crystallinity as well as the absence of Sn precipitates. Low magnification HAADF/STEM images and EDX maps of Si, Ge, and Sn in $Ge_{0.84}Si_{0.12}Sn_{0.04}$ **(c)** and $Ge_{0.84}Si_{0.04}Sn_{0.12}$ **(d)** layers.

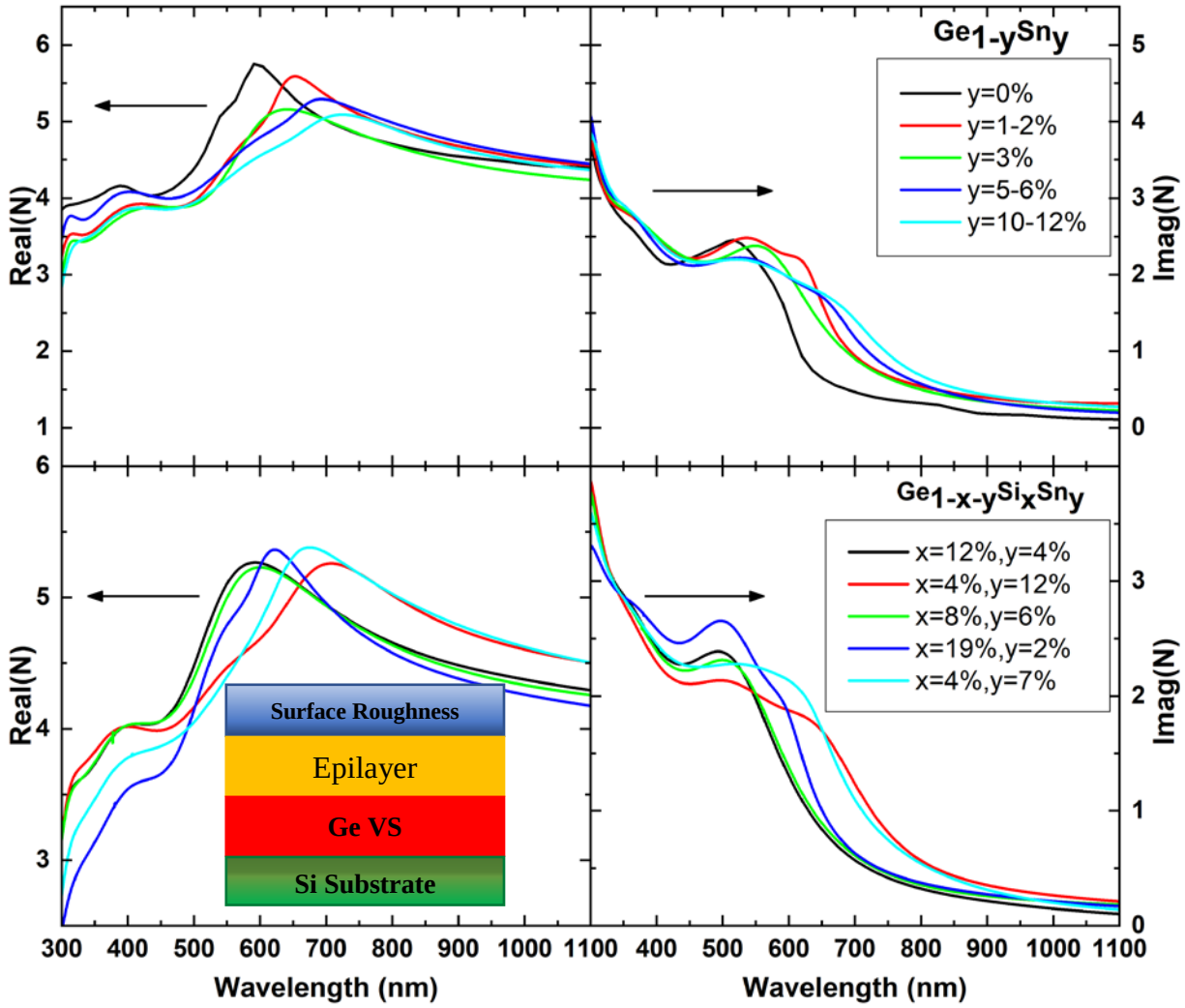

Figure 6-2: The complex refractive index constant $N(\lambda)$ spectra of (top) $Ge_{1-y}Sn_y$ binary semiconductor alloy as a function of wavelength for different Sn composition and (bottom) of $Ge_{1-x-y}Si_xSn_y$ ternary alloy as a function of wavelength for different Si and Sn composition obtained from a spectroscopic ellipsometry measurement. The inset show the multilayer model used to extract the optical properties (section 3.2.3 of Chapter 3)

6.1.3 Theoretical Calculations

To implement the Lorentz-Mie scattering formalism, already presented in section 3.1.2 of Chapter 3, a MATLAB® code was developed to solve the Maxwell equations in all the aforementioned NW systems (NW and CSNW). Furthermore, a Full-Vector, Finite-Difference, complex mode solver was developed in order to find the effective refractive index of the CSNW structure based on the work presented in Ref. [143]. Calculations were carried out on a PC equipped with a single Intel Core 4 Quad 2.40GHz processor equipped with 32GB of RAM.

6.2 Results and Discussion

Different CSNWs were investigated, including Si/$Ge_{1-y}Sn_y$, Si/$Ge_{1-x-y}Si_xSn_y$, Ge/ $Ge_{1-y}Sn_y$ and Ge/$Ge_{1-x-y}Si_xSn_y$. Firstly, before investigating the solar absorption enhancement in CSNWs, Figure 6-3, shows the calculated short-circuit current density enhancement of a bilayer thin film structure of equal thickness $d_1 = d_2$ composed of different group IV semiconductor alloys; mainly Si/Ge, Si/ $Ge_{0.88}Sn_{0.12}$, Ge/ $Ge_{0.88}Sn_{0.12}$, Si/ $Ge_{1-x-y}Si_xSn_y$ and Ge/ $Ge_{1-x-y}Si_xSn_y$ with (x, y) = (12%, 4%) and (4%, 12%). The short-current density was evaluated using Eq. (6-2) and the absorption efficiency for the single and double layer was calculated using the Transfer Matrix Method (TMM) described extensively in Reference [241] under a TM polarization and normal incidence. Figure 6-3 demonstrates a significant enhancement in the photocurrent when Si and Ge are capped by an Sn-containing binary or ternary layer, relative to a single Si and Ge layer of the same thickness. On the one hand, this enhancement is more pronounced for a Si based substrates where a ~9 nm-thick $Ge_{0.88}Sn_{0.12}$ or $Ge_{0.84}Si_{0.04}Sn_{0.12}$ capping layer yields a ~14-fold increase in photocurrent as compared to bare Si. Moreover, we can conclude by comparing the short-current enhancement of Si/Ge and Si/$Ge_{0.99}Sn_{0.12}$ that these large enhancement factors are a result of the addition of the unique optical properties of the Sn alloy rather of the small band gap of Ge. On the other hand, adding Sn-rich binary or ternary alloys ($Ge_{0.88}Sn_{0.12}$ or $Ge_{0.84}Si_{0.04}Sn_{0.12}$) on a Ge substrate seems to affect less the short-circuit current enhancement with an increase of ~25% at 11 nm thickness, compared to its Si counterparts. It is important to note that the richer in Sn the samples are, the higher the short-circuit current enhancement is. Afterwards, this behavior will be investigated to see if it still holds for CSNW structures and compare the short-current enhancement of CSNW to thin films. It is worth mentioning that in a conventional planar structure, increased reflection or backscattering from the material's front surface decreases light absorption. Thus, changing the geometry from thin films to 1D subwavelength NW would increase scattering, which is an indicative of an enhanced optical antenna effect, which increases both scattering and absorption in the NW.

Secondly, Lorentz-Mie calculation is used to generate 2D maps of absorption and scattering efficiencies as a function of the incident wavelength and of the NW core radius for the Si/GeSn

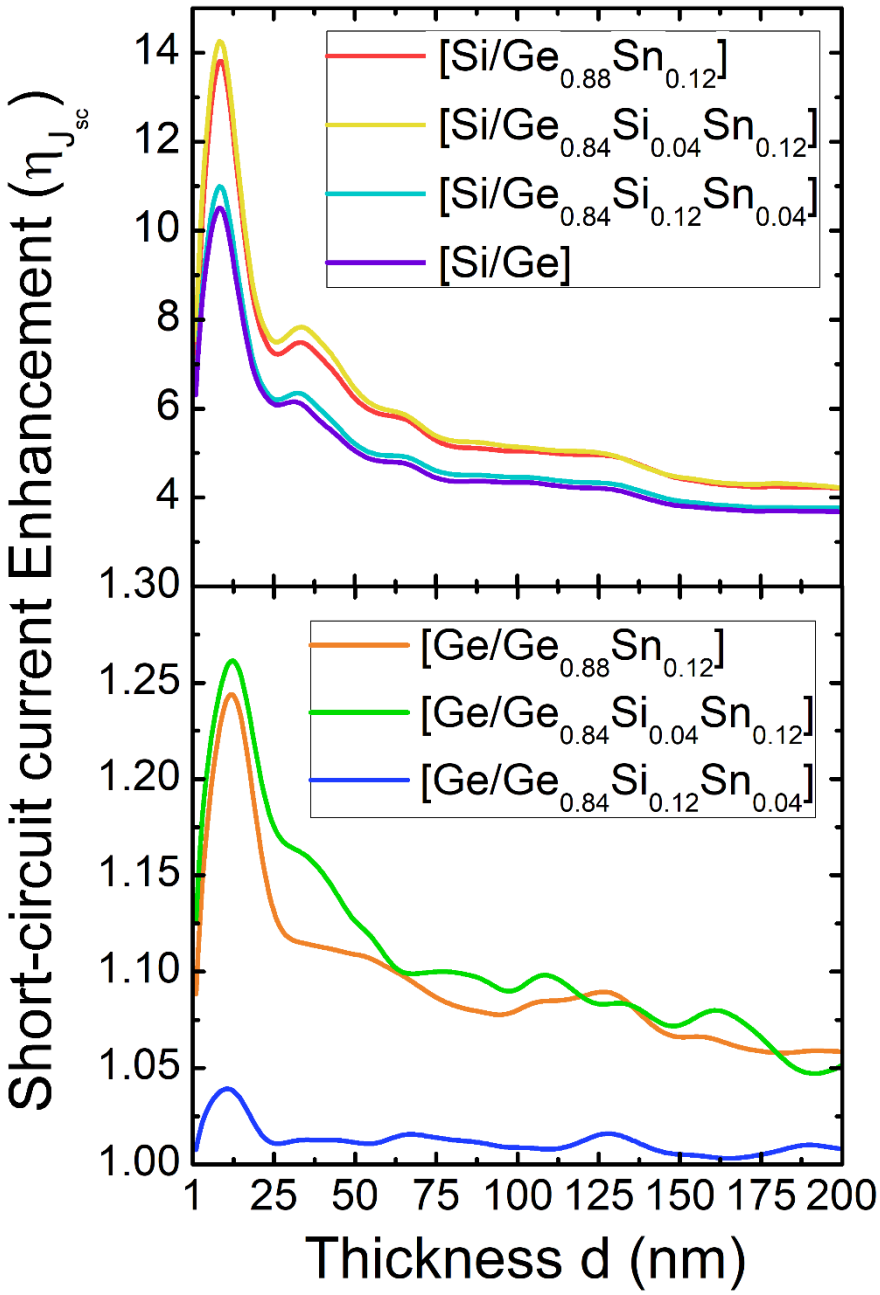

Figure 6-3: Photocurrent enhancement for a bilayer structure having film thicknesses between 1 and 200 nm where the first layer of thickness d_1, shown in the inset is either Si or Ge layer and where the top thin layer of thickness d_2 is either $Ge_{0.88}Sn_{0.12}$, $Ge_{0.84}Si_{0.04}Sn_{0.12}$ or $Ge_{0.84}Si_{0.12}Sn_{0.04.}$ The short-circuit current enhancement is evaluated for when $d_1 = d_2$.

and Ge/GeSn structures. The maps of absorption and scattering efficiencies of CSNWs, with a shell made of the binary alloy GeSn and a core made of Si or Ge, are examined as displayed respectively in Figures 6-4 and 6-5 at two shell thickness $t = R_c/4$ and $t = R_c$. Figure 6-4 exhibits the

absorption (top) and scattering (bottom) efficiencies of the Si/$Ge_{0.88}Sn_{0.12}$ CSNW, whereas Figure 6-5 shows the corresponding results for the Ge/$Ge_{0.88}Sn_{0.12}$ CSNW.

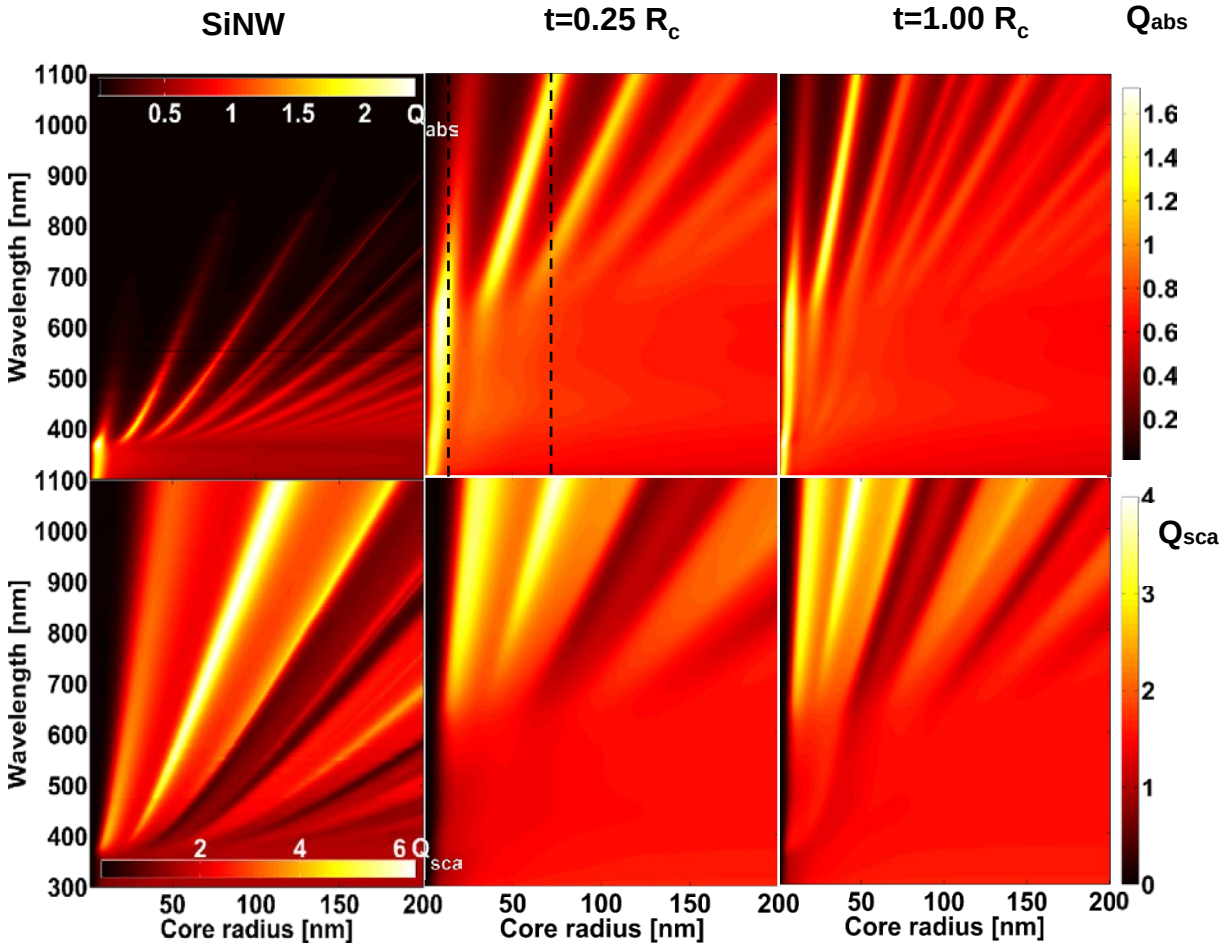

Figure 6-4: Unpolarized absorption efficiency Q_{abs} (top) and unpolarized scattering efficiency Q_{sca} (bottom) of Si/$Ge_{0.88}Sn_{0.12}$ CSNW surrounded by air as a function of the core radius R_c and the incident light wavelength for two different shell thicknesses: $t = R_c/4$ and $t = R_c$. For comparison, SiNW absorption and scattering efficiencies are also shown. The three black-dashed lines indicate the selected radii: on-resonance (at $R_c = 8\ nm$) and off-resonance (at $R_c = 60\ nm$).

Moreover, the figures also display the absorption and scattering efficiencies for SiNW and GeNW thus highlighting the effect of the Sn-containing shell on the absorption and scattering efficiencies. For wavelengths larger than ~550 nm, Q_{sca} shows distinct features in terms of bright whiskers for both TE and TM polarization (not shown in Figures 6-4 and 6-5, but can easily be inferred from

the unpolarized 2D map because $Q_{sca}^{Unp} = (Q_{sca}^{TE} + Q_{sca}^{TM})/2$). The slope of the whiskers is decreasing with increasing core radius R_c and decreasing wavelengths. A possible way to explain these whiskers of the scattering efficiency is by considering the theoretical expression of Q_{sca} given by the Lorenz-Mie formalism for a CSNW (formulas of the scattering coefficients are presented in section 3.1.2 of Chapter 3).

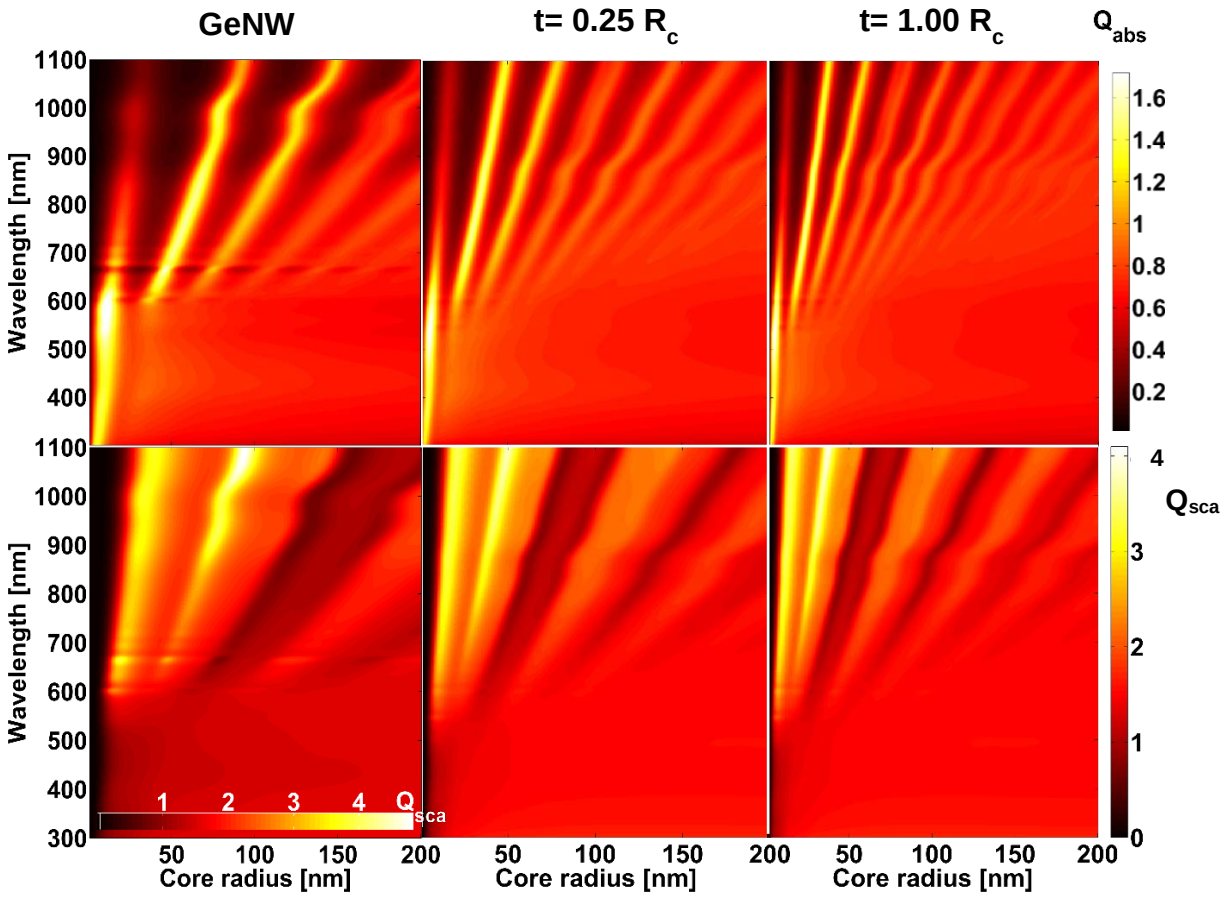

Figure 6-5: Unpolarized absorption efficiency Q_{abs} (top) and unpolarized scattering efficiency Q_{sca} (bottom) of Ge/ $Ge_{0.88}Sn_{0.12}$ CSNW surrounded by air as a function of the core radius R_c and the incident light wavelength for two different shell thicknesses: $t = R_c/4$ and $t = R_c$. For comparison, GeNW absorption and scattering efficiencies are also shown.

In fact, since the complex refractive index of $Ge_{0.88}Sn_{0.12}$ shows a weak dependence on the wavelength for $\lambda > 550$ nm (see Figure 6-2), the scattering coefficients are proportional to the size parameter $x_{j\ (j\in\{shell,core\})} \propto R_c/\lambda$. Thus, Q_{sca} is nearly constants along straight lines in the (λ,

R_c) –plane. The same behavior is observed for scattering efficiency Q_{sca} for both CSNW systems with a $Ge_{0.88}Sn_{0.12}$ shell but the whiskers are observed in different regions.

Next, the effect of the shell thickness on the absorption and scattering efficiencies will be studied thoroughly. By examining the data obtained for the Si/$Ge_{0.88}Sn_{0.12}$ CSNW (Figure 6-4), two important observations emerge. First, the whiskers resonance distribution shows an evolution as a function of the core and shell dimensions. Particularly, the whiskers distribution with increasing GeSn shell thickness t will move toward higher wavelength. In fact, for a fixed core radius ($R_c = 60\ nm$) and an increasing shell thickness, Figure A.3(a-b) in Appendix A show, qualitatively, this behavior where the effect of the geometrical parameters on the leaky resonant modes is shown. In fact, by focusing on the TM_{41}, increasing the shell thickness will induce a redshift in the leaky mode resonance. Besides, the higher leaky modes are located at a smaller wavelength, whereas the fundamental mode TM_{01} is located near the mid-infrared range. Three resonant Mie absorption peaks were observed at 720.6 nm, 932 nm, 733 nm, and 1073 nm for a shell thickness equal to $0.5 \times R_c$ (green curve in Figure A.3(a), Appendix A). Incident electromagnetic waves having specific wavelength, λ, are trapped along the periphery of core/shell nanowires similar to whispering gallery modes in micrometer-scale resonators. The resonant field intensity is built up inside the nanowire and then the confined mode leaks due to the small size of nanowires compared to the wavelength of the light ($\lambda > 300\ nm$ and $d < 200\ nm$). The leakage effect is observable in the electric field profile shown in Figure A.3(b), Appendix A for the fundamental leaky mode TM_{01} and a core radius of 8 nm and a shell thickness equal to $0.25 \times R_c$. To quantitatively analyze the leaky modes evolution *vs.* the core radius, the Helmholtz-Eigen equation was numerically solved by using a full-vector, finite difference (FVFD) approach coupled with a perfectly matched layer (PML) boundary condition terminated with a zero boundary condition [242] to find the complex effective refractive index n_{eff} of the CSNW. Each complex solution is the eigenvalue of a specific leaky mode. Leaky modes can be characterized by an azimuthal mode number, *m*, which indicates an effective number of wavelengths around the wire circumference and a radial order number, *l*, describing the number of radial field maxima within the cylinder (for instance TM_{ml}).[141] The leaky mode resonances, TE_{ml} and TM_{ml}, have previously been shown to correspond to peaks in the scattering and absorption spectra of nanowires.[141,243] The real part of n_{eff} is indicative of the resonant wavelength and propagation constant and the imaginary part is indicative of the radiative loss of the mode, which for a lossy medium is also a

measure of the absorptive loss. Thus, the resonant scattering wavelength can be estimated from $m\lambda/n_{eff} = \pi d$ where $m = 1, 2, \ldots$, λ is the free space wavelength of incident light, n_{eff} is the effective refractive index, and d is the diameter of the nanowire. For instance, the nanowire with a 120 nm diameter ($R_c = 60\ nm$) exhibits an absorption peak at 1073 nm as shown in Figure A.4(a). By using the above formula, n_{eff} is found to be equal to 2.862 (for m = 1), which is close to the refractive index of the Si core (3.55) at this wavelength. Using the FVFD approach, the effective refractive index was estimated to be 3.13656. Such a result reveals two important features: the optical antenna effect is maximized at each resonance and the scattering and absorption spectra are highly structured with multiple discrete peaks; and this optical antenna effect is enhanced by decreasing the NW core radius. As shown in Figures 6-4 and 6-5 (bottom), when the core radius is smaller or the wavelength of the incident light is longer, the scattering efficiency increases. The data presented in Figs. 6-4 and 6-5 clearly demonstrate the ability to tune the absorption and scattering of light using CSNWs by controlling either the NW radius or the light wavelength in the visible and especially the NIR range where the scattering efficiency is maximized. The second important element affecting the absorption efficiency is the presence of localized resonant modes. Similar observations were reported in different systems: GaN nanowire cavity,[244] hydrogenated amorphous silicon a-Si:H core with a dielectric shell [245] and polycarbonate (PC) - polyvinylidene difluoride (PVDF) CSNW.[246] Interestingly, it is possible to engineer the resonant properties inside a CSNW by tuning the core radius and/or the shell thickness in a way that light absorption can be enhanced at resonance regions, the so called the leaky-mode resonance (LMR) enhancement. This effect will be explored to optimize the morphology of CSNWs to achieve efficient light absorption. For this, in the following the optimal core radius, shell thickness, and the shell type (be it $Ge_{1-y}Sn_y$ binary alloy or $Ge_{1-x-y}Si_xSn_y$ ternary alloy) will be defined. The absorption behavior can be understood by means of the Fano-resonance effect[247] that is an interference effect arising from the incident light and the localized reemitted leaky-mode resonance light due to the subwavelength size of NWs. Moreover, in order to quantify the absorption of different CSNW structures across the solar spectrum, the ultimate efficiency η_{eff} will be evaluated [248], assuming that each absorbed photon with energy greater than the band gap produces a single electron-hole pair with energy hc/λ_g, where λ_g is the wavelength corresponding to the minimum band gap between the core and the shell. Note that unstrained Si and Ge have an indirect band gap of 1.12

eV and 0.66 eV, respectively, whereas the unstrained $Ge_{0.88}Sn_{0.12}$ is a direct gap semiconductor having a gap of 0.49 eV.[40] η_{eff} is given by:

$$\eta_{eff} = \frac{\int_{0.3\ \mu m}^{\lambda_g} F_s(\lambda) Q_{abs}(\lambda, r_c, t) \frac{\lambda}{\lambda_g} d\lambda}{\int_{0.3\ \mu m}^{4\ \mu m} F_s(\lambda) d\lambda}; \quad (6\text{-}1)$$

where λ is the wavelength, $F_s(\lambda)$ is the spectral irradiance (power density in $W.m^{-2}.nm^{-1}$) of the ASTM AM1.5G direct normal and circumsolar spectrum[140], $Q_{abs}(\lambda, R_c, t)$ is the spectral absorption efficiency evaluated with the Mie-Lorentz scattering formalism and λ_g is the wavelength corresponding to the minimum band gap between the core and the shell. Special care is needed when evaluating the integrals in Eq. (6-1), due to the non-uniformity of the spectral range in the ASTM data. To solve this issue, a Piecewise cubic Hermite interpolating polynomial was used to interpolate the optical properties between 300 and 1100 nm, to match the ASTM spectra wavelength steps. For instance, if we consider the Si/GeSn CSNW, then λ_g =2.583 μm. The ultimate efficiency can be linked to the maximum short-circuit current, J_{sc}, by assuming an ideal carrier collection efficiency where every photogenerated carrier reaches the electrodes and contributes to photocurrent. Under this condition, J_{sc} is written:

$$J_{sc} = \frac{q}{hc} \int_{0.3\ \mu m}^{\lambda_g} F_s(\lambda) Q_{abs}(\lambda, R_c, t) \lambda d\lambda = 0.0726 \times \lambda_g \eta_{eff}\ [mA/cm^2] \quad (6\text{-}2)$$

where q is the elementary charge. However, because Q_{abs} can reach values greater than unity, as explained above, the integrated solar absorption cannot truly be considered as the real ultimate photocurrent intensity or the short-circuit current density. Nevertheless, J_{sc} is a figure of merit proportional to the actual photocurrent intensity, very useful to compare to the absorption efficiency capability of the studied quantum structures.[227]

The photocurrent enhancement is defined as the ratio of the short-circuit current of a two-layer stack to the short-circuit current of a Si or Ge film. For instance, the enhancement of the photocurrent of Si/$Ge_{0.88}Sn_{0.12}$ thin film (red line in Figure 3a) is evaluated by calculating the ratio

$$\eta_{J_{sc}} = \frac{J_{sc}^{Si/GeSn}}{J_{sc}^{Si\ Bulk}}\ \ (Bulk)\ or\ \eta_{J_{sc}} = \frac{J_{sc}^{Si/GeSn\ CSNW}}{J_{sc}^{Si\ NW}}\ \ \ (NW)$$

where $J_{sc}^{Si/GeSn}$ and $J_{sc}^{Si\ Bulk}$ are the photocurrents generated in Si/$Ge_{0.88}Sn_{0.12}$ stack and Si thin film, respectively. To quantify the short-circuit current enhancement for thin-films or nanowire structures, the reference short-circuit current ($J_{sc}^{Si\ Bulk}\ or\ J_{sc}^{Si\ NW}$) is evaluated following this procedure: (*i*) for thin films A/B, the short-circuit current is evaluated for a thin-film slab of thickness $d_A + d_B$ composed only from material A, whereas (*ii*) for A/B CSNW structure, the short-circuit current is calculated for a single nanowire composed of material A and having a core radius of $R_c + t$ where t is the shell thickness of the B layer in the A/B CSNW structure. $\eta_{J_{sc}}$ displays a few peaks attributed to Fabry-Pérot resonance which is much weaker than LMR in NWs.

To investigate the absorption enhancement in CSNWs, the integrated solar absorption efficiency was evaluated as a function of the NW dimensions for the four structures proposed above and analyzed in Figure 6-6. Figure 6-6 (a) displays the variation of the solar absorption efficiency as a function of the shell thickness (t) and the core radius (R_c). The whiskered features can be recognized, similar to the absorption efficiency presented in Figures 6-4 and 6-5, attributed to LMR modes. Interestingly, the 2D photocurrent enhancement maps of Si/$Ge_{0.88}Sn_{0.12}$ and Si/$Ge_{0.84}Si_{0.04}Sn_{0.12}$ NW structures show narrow regions ($R_c < 56\ nm$ and $t < 40\ nm$) where an extreme enhancement of J_{sc} is achieved reaching an increase of 11-22-fold for Si/$Ge_{0.88}Sn_{0.12}$ and 25-47-fold for Si/$Ge_{0.84}Si_{0.04}Sn_{0.12}$ compared to SiNW. Besides, from the maps of Ge/$Ge_{0.88}Sn_{0.12}$ and Ge/$Ge_{0.84}Si_{0.04}Sn_{0.12}$, when the core radius is larger than the shell thickness ($R_c > t$), we observe a maximum short-current enhancement of 7-fold compared to the GeNW system. The enhancement is governed by the LMR modes, where the highest enhancement occurs for a shell thickness below 8 nm and a core radius between 30 and 45 nm. Table 6-1 summarizes the key results of the short-circuit current enhancement for the above CSNW structures.

Additionally, to quantitatively compare the short-current enhancement between CSNW and thin film systems, Figure 6-6(b) presents the ratio $\eta_{J_{sc}}$ for the Si/$Ge_{0.88}Sn_{0.12}$ at two different shell thickness ($t = R_c/4\ , R_c$) for the CSNW (red curves) and two top layer thickness ($d_2 = d_1/4\ , d_1$)

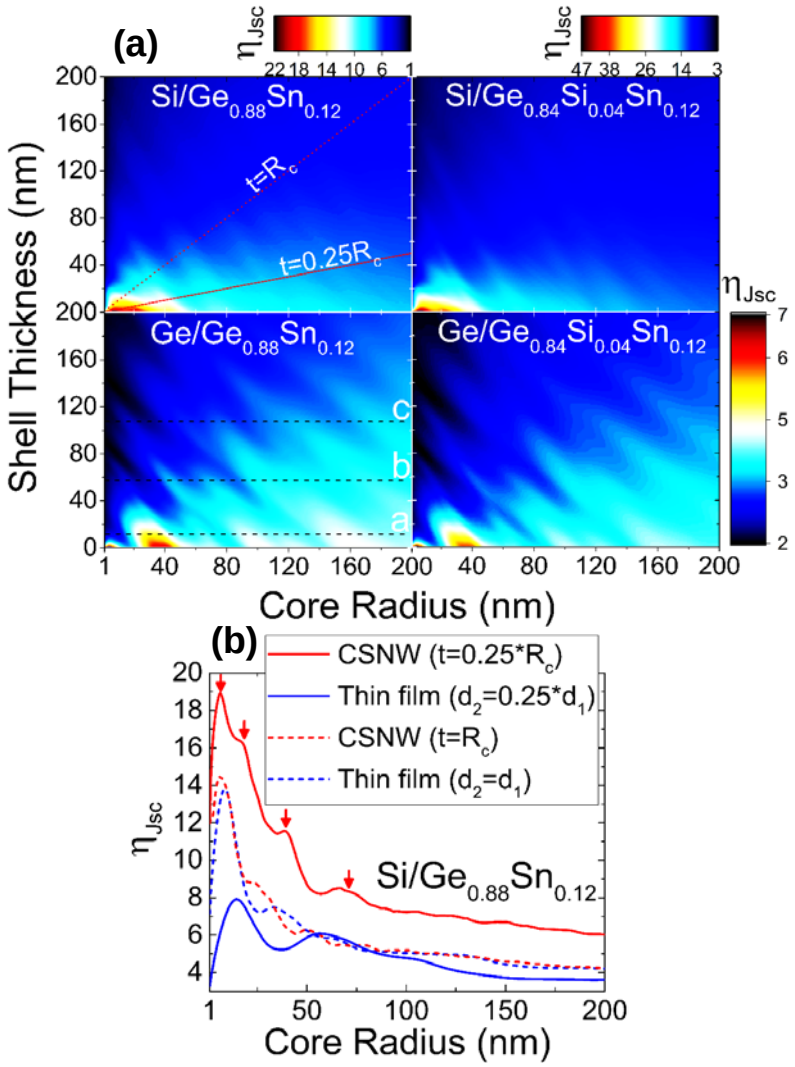

Figure 6-6: **(a)** 2D short-circuit photocurrent enhancement $\eta_{J_{sc}}$ map as a function of the shell thickness t and the core radius R_c for the CSNW structures: from top-left to bottom-right: Si/ $Ge_{0.88}Sn_{0.12}$, Si/ $Ge_{0.84}Si_{0.04}Sn_{0.12}$, Ge/ $Ge_{0.88}Sn_{0.12}$ and Ge/ $Ge_{0.84}Si_{0.04}Sn_{0.12}$. $\eta_{J_{sc}}$ is equal to the absorption efficiency of the CSNW structure divided by the one for the core NW with a radius of $R_c + t$. The horizontal dashed lines represent 3 different shell thicknesses (line a→t=3 nm; line b→t=50 nm and line c→t=100 nm) that will be analyzed more in detail in Figure 6-7. Additionally, we present in panel **(b)** a line profile of Si/ $Ge_{0.88}Sn_{0.12}$. CSNW 2D map, along two shell thickness ($t = [0.25, 1] \times R_c$) directions, shown as solid red and dashed-red lines respectively in panel (a). The red lines represent intensity profiles extracted from the 2D map in panel a following the directions $t = R_c$ and $t = R_c/4$. We also present the short-current enhancement of thin-film structure for 2 different top-layer thickness ($d_2 = 0.25d_1$ and $d_2 = d_1$) for a Si/ $Ge_{0.88}Sn_{0.12}$ stack. The red arrows represent the peak core radius positions attributed to LMR.

for the thin films (blue curves). The short-circuit current enhancement $\eta_{J_{sc}}$ is evaluated by calculating the ratio of J_{sc} of the CSNW structure with a core radius R_c and a shell thickness t divided by J_{sc} of the core NW with a core radius of $R_c + t$. $\eta_{J_{sc}}$ of the CSNW at $t = R_c$ is almost comparable to its counterparts for the thin film. Nevertheless, the outer layer thickness decreases from $t = R_c$ to $t = R_c/4$ for the CSNW and from $d_2 = d_1$ to $d_2 = d_1/4$ for the thin film, a maximum short-current enhancement is observed from 14 to 19, respectively, in the CSNW and a decrease from 13 to 8 in the thin film. This is an interesting finding suggesting that to increase light absorption in CSNW, the shell thickness t of the CSNW must be inferior than the core radius R_c. Thus, on the one hand, decreasing the shell thickness from R_c to $R_c/4$ of Si/GeSn CSNW will improve-on average- the short-current by 45%. On the other hand, decreasing the top layer thickness of the Si/GeSn thin-film from d_1 to $d_1/4$ will deteriorate-on average- the short-circuit current by 15%.

Table 6-1: Core radius and shell thickness range corresponding to the optimal short-current enhancement (the highest value $\eta_{J_{sc}}$) for the four Core/Shell NW structures.

Core		Si		Ge
Shell	$Ge_{0.88}Sn_{0.12}$	$Ge_{0.88}Si_{0.04}Sn_{0.12}$	$Ge_{0.88}Sn_{0.12}$	$Ge_{0.88}Si_{0.04}Sn_{0.12}$
R_c (nm)	3-31	3-45	30-45	30-42
t (nm)	1-11	1-14	1-8	1-5
$\eta_{J_{sc}}$	13-22	22-47	6	5.5

To better illustrate the effect of the shell thickness on the photocurrent, data obtained for three different thicknesses (t = 3, 50, and 100 nm) are selected from the 2D photocurrent maps (dashed lines labeled a, b and c in Figure 6-6(a)) and plotted in Figure 6-7. The corresponding photocurrents are compared to those generated in SiNW and GeNW. Note that the latter two have been extensively investigated in recent years[136,249–251] and our estimated photocurrents for SiNW and GeNW are in full agreement with early reports. More importantly, Figure 6-7 clearly

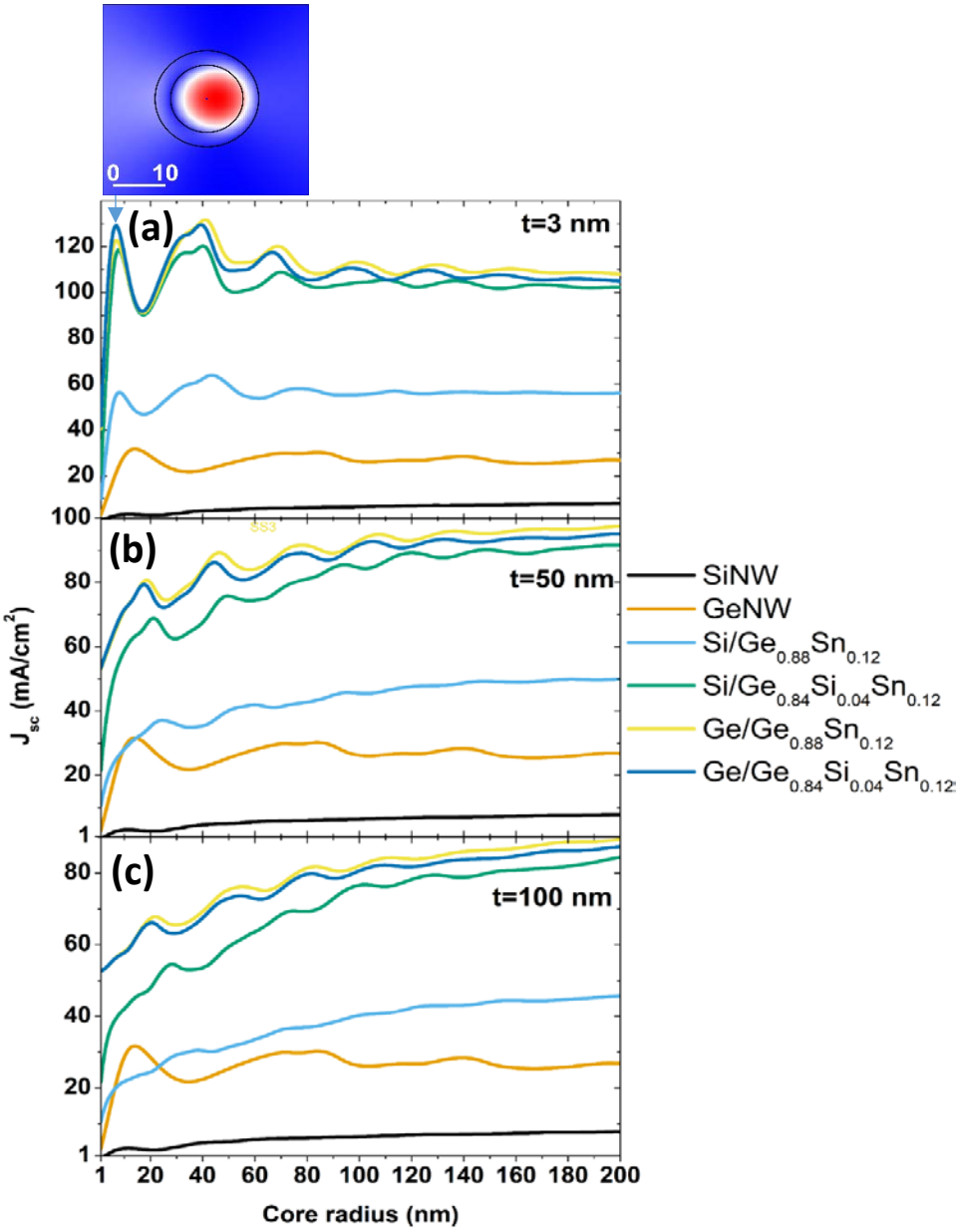

Figure 6-7: Integrated solar absorption J_{sc} (mA/cm^2) as a function of the core radius of the CSNWs consisting of absorbing group IV binary and ternary alloy semiconductors materials. The shell thickness is fixed to **(a)** 3 nm, **(b)** 50 nm and **(c)** 100 nm and plot the solar absorption as a function of the core radius for Si/ $Ge_{0.88}Sn_{0.12}$, Si/ $Ge_{0.84}Si_{0.04}Sn_{0.12}$, Ge/ $Ge_{0.88}Sn_{0.12}$, Ge/ $Ge_{0.84}Si_{0.04}Sn_{0.12}$, GeNW and SiNW structures. The GeNW and SiNW solar absorption are presented for comparison sake, with a core radius equal to $R_c + t$ for a fair comparison, to easily visualize the enhancement of light absorption in these structures. We also show the near electric field profile at the highest achievable short-current at a shell thickness of 3 nm and a core radius of 7 nm. We can infer from the profile distribution that the leaky fundamental mode is responsible for such a high short-current.

shows that the addition of a SiGeSn or GeSn shell enhances significantly the photocurrent. For instance, the photocurrent enhancement has almost increased five-fold in Si/GeSn and ten-fold in Si/GeSiSn CSNW structures as compared to SiNW (black curves in Figure 6-7) at a shell thickness of 3 nm for core radii larger than 60 nm. Also, when the shell thickness is equal to 3 nm (Figure 6-7(a)), the highest value for J_{sc} reaching up to 130 mA/cm^2 is obtained for the Ge/ GeSn structure at a core radius of 40 nm. This is due to the presence of the TM_{11}/TE_{01} leaky resonance mode at a core radius above 30 nm for all the studied NWs. Also, an important improvement in J_{sc} is noticed at smaller core radii which can reach 120 mA/cm^2 for Ge/GeSn, Ge/GeSiSn and Si/GeSiSn structures for a 3 nm-thick shell. Increasing of the shell thickness will contribute to a deterioration of the short-circuit current, as it can be seen from Figures 6-7(b) and (c) and has been shown from the latter analysis of Figure 6-6(b). Additionally, when panels (b), and (c) in Figure 6-7 are compared with each other, it shows that there is relatively little difference between panel (b) and (c) in absolute values, suggesting similar behavior for shell thickness greater than 50 nm. This can be deduced from the top left panel in Figure 6-6(a). This extreme enhancement at a very small core radius ($R_c = 7\ nm$) and shell thickness ($t = 3\ nm$) is due to the TM_{01} leaky resonance mode which is shown by the near-field profile inset in Figure 6-7.

The fact that the photocurrent enhancement is practically independent of the core radius above ~100 nm is an interesting result suggesting that the generated photocurrent can be tuned through a simple control of the shell thickness rather than the core radius thus providing more flexibility in the fabrication process. However, to ensure the integration of these structures in photonic devices, it is important to also optimize the efficiency of charge collection, which depends on the minority carrier lifetime, lattice defects, contact quality and design.

In addition, to further investigate the optimal CSNW geometry for light absorption, we defined a dimensionless parameter, η_{abs}, as the ratio of the absorption efficiency of the CSNW to that of a pure NW (SiNW or GeNW) with a core radius of $R_c + t$ equal to its CSNW counterparts. For instance, if we consider the structure Si/GeSn, the absorption enhancement factor is defined as

$$\eta_{abs}(r_c, t, \lambda) = \frac{Q_{abs}^{Si/GeSn}}{Q_{abs}^{SiNW}}; \tag{6-3}$$

If η_{abs} takes values larger than unity, then CSNW structures absorb light efficiently as compared to SiNW or GeNW. The higher the value of η_{abs}, the more efficient absorber the CSNW is.

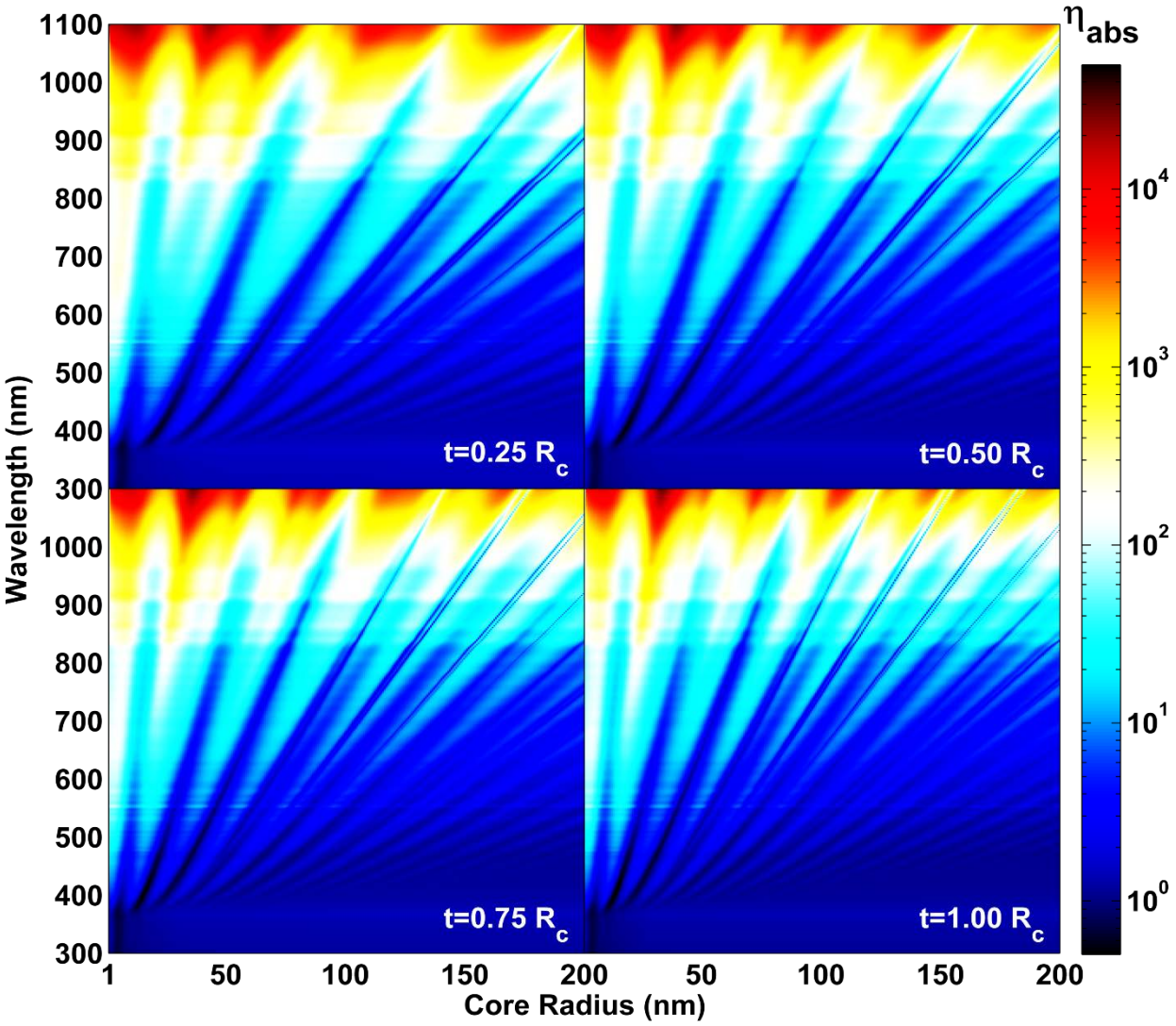

Figure 6-8: Extreme light absorption enhancement map as a function of the core radius and the incident light wavelength for the Si/$Ge_{0.88}Sn_{0.12}$ core-shell nanowire for different shell thicknesses t= [0.25, 0.5, 0.75, 1] × R_c.

The enhancement of solar absorption and photocurrent are due to the plurality of spectrally-separated LMR supported by large core diameters. In the enhancement maps (Figure 6-8 for the Si/$Ge_{0.88}Sn_{0.12}$, Figure A.4(a), Appendix A for the Si/$Ge_{0.84}Si_{0.04}Sn_{0.12}$ and Figure A.4(b), Appendix A for the Ge/$Ge_{0.88}Sn_{0.12}$), a strong absorption enhancement that follow very specific directions is

observed. In fact, when the incident wavelength matches one of the leaky modes supported by the NW [249,250], optical responses, including light scattering and absorption, were found to be substantially enhanced as compared to a simple SiNW. A gradual increase in the enhancement of light absorption for the Si/GeSn system is observed as compared to a SiNW where between 800 and 1000 nm, η_{abs} ~10^3. Next, between 1000 and 1100 nm, η_{abs} reaches its maximum ~10^4. For instance, at $r_c = 33\,nm$, $\lambda = 1086\,nm$ and $t = R_c$, $\eta_{abs} \cong 3 \times 10^4$ for Si/GeSn CSNW. Additionally, when increasing the thickness of the shell, the leakier resonance modes are excited, which is reflected by the increase in the number of whiskers in the map: at $t = R_c/4$, only five broad whiskers are observed, whereas at $t = R_c$, eight are found for $Si/Ge_{0.88}Sn_{0.12}$ at the same core radius. Interestingly, the $Ge/Ge_{0.88}Sn_{0.12}$ CSNW's enhancement map (see Figure A.4(b), Appendix A) displays a different result. Indeed, unlike the Si-based CSNW, the enhancement in the Ge-based CSNW is relatively small (~12 vs. ~10^4). Besides, above 700 nm, the enhancement along the LMR is clear and it reaches its maximum in NIR region for $860 \leq \lambda \leq 1100\,nm$ and $R_c = 42, 37, 32\ and\ 30\,nm$ for each shell thickness t. Specifically, at $980 \leq \lambda \leq 1100\,nm$, $R_c = 30\,nm$ and $t = R_c$, the absorption enhancement factor η_{abs} is between 9 and 12. This is in accordance with the short-current enhancement map where at the same core radius and shell thickness, $\eta_{J_{sc}}$ is equal to 3.5 which is equivalent to a high short-current of 95 mA/cm^2.

The extreme enhancement of light absorption in Si/GeSn and Si/GeSiSn structures presents an interesting opportunity to achieve optimal wavelength selectivity in the desired NIR region through an optimal choice of the core radius and shell thickness of the CSNW. Therefore, it is important to optimize the physical dimensions (R_c, t) of the CSNW in order to guarantee both photocurrent and absorption efficiency enhancement. Thus, for $Si/Ge_{0.88}Sn_{0.12}$, we propose using core radii R_c =17, 41, 70, 113, 132 and 172 nm for a shell thickness $t = R_c/4$, at which Q_{abs} is enhanced. In addition, when $R_c = 6.3, 17$ and 38 nm, the short-circuit current is enhanced as shown in the red solid curve of Figure 6-6(b) where the red arrows indicate the corresponding core radii. Thus, a core-radius of 17 nm would guarantee a simultaneous short-current and an absorption efficiency enhancement. Besides, for $t = R_c$, the optimal core radii are 10, 32, 73, 108 and 149 nm. On the other hand, for $Si/Ge_{0.84}Si_{0.04}Sn_{0.12}$ and at $t = R_c$, the optimal radii are 9, 31, 50, 72, 106, 118 and 147 nm.

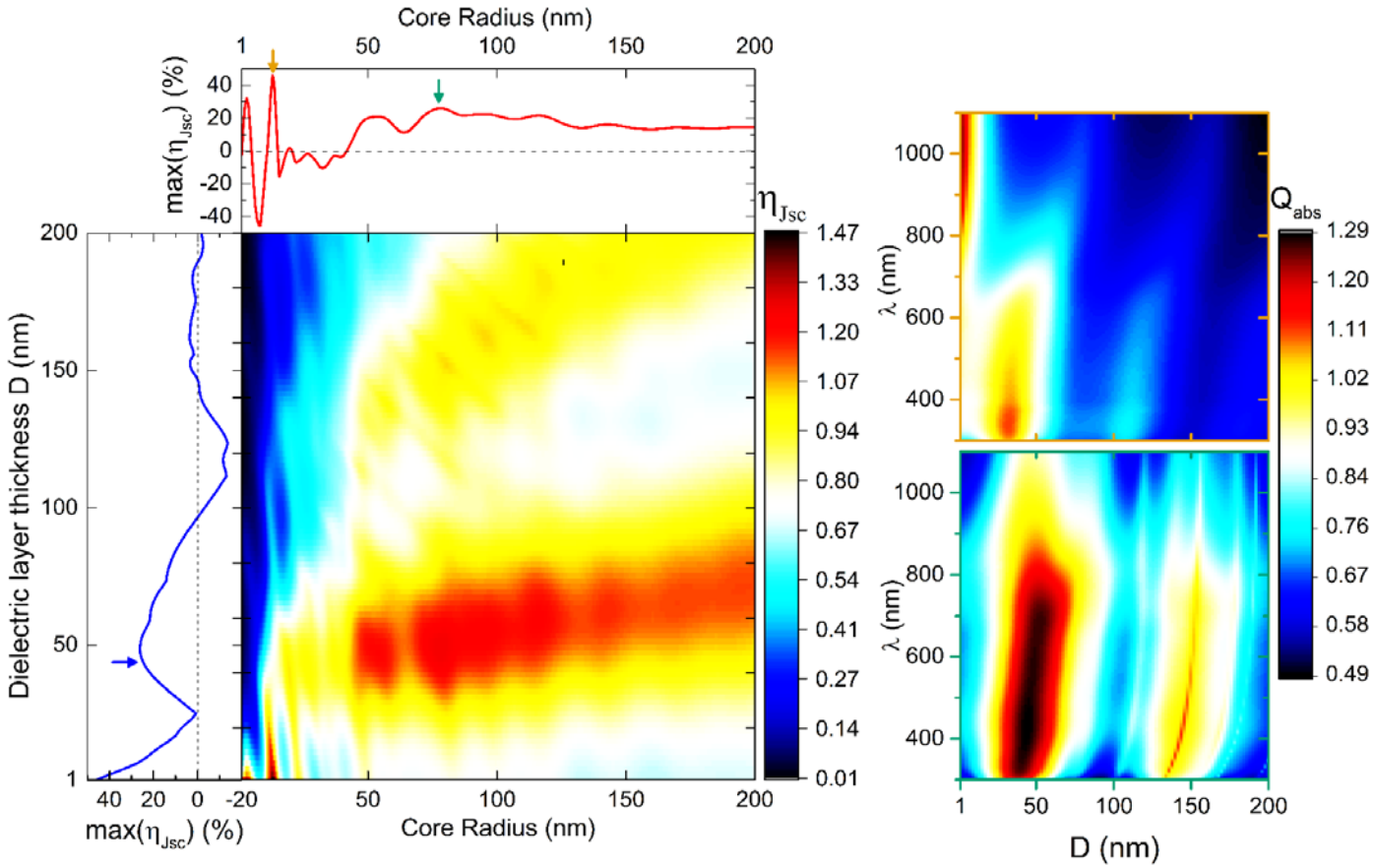

Figure 6-9: **(a)** The short-current enhancement map of the ($Si/Ge_{0.88}Sn_{0.12}/Si_3N_4$) system where the inner-shell thickness was set to be equal to the core radius ($t_{i.s.} = R_c$) and the dielectric capping layer thickness D was varied from 1 to 200 nm. The top panel shows the relative maximum change of the short-current enhancement ($\max(\eta_{Jsc})$ in %) *vs.* the core radius, whereas the left panel represents the relative change of $\max(\eta_{Jsc})$ *vs.*D. The relative change is evaluated using the following equation: $(\eta_{Jsc} - 1) \times 100$. The short-current enhancement was evaluated as the ratio of the short-current of the core-multishell nanowire to the short-current of the base CSNW (Si/GeSn) ($\eta_{J_{sc}} = J_{sc}^{\mathrm{Si/GeSn/SiN}} / J_{sc}^{Si/GeSn}$). The orange and green arrows in the top panel represent, respectively, the core radii R_c equal to 13.6 and 78.2 nm, where J_{sc} is enhanced. Next, fixing R_c to the previous radii, panel **(b)** and **(c)** show, a 2D map of the absorption efficiency Q_{abs} as a function of the incident wavelength λ and the dielectric thickness D.

The investigations described above provide the basis to design high performance NW-based optoelectronic and photonic devices. In the following, the influence of an additional layer around the CSNW structure will be addressed and the collective properties of an array of CSNWs will be elucidated. A single configuration will be considered: a non-absorbing dielectric layer (Si_3N_4) around an Si/$Ge_{0.88}Sn_{0.12}$ CSNW (Si/$Ge_{0.88}Sn_{0.12}$/Si_3N_4) (The optical properties of Si_3N_4 are taken from Ref.[252]). The choice of silicon nitride (Si_3N_4) as a coating material emanates from two characteristics: firstly, the surface passivation effect [253,254] and secondly the antireflective properties reducing light reflection considerably. Taking into consideration these aspects, light absorption and scattering in a Si/$Ge_{0.88}Sn_{0.12}$/Si_3N_4 NW was simulated. Because optical resonances serve to enhance the light−matter interaction of the NW cavity, the dielectric-shell optical antenna effect is expected to increase not only light scattering but also light absorption in PV devices.[249] Figure A.1(c), Appendix A shows the geometrical configuration and the necessary parameters for the previous system. Figure 6-9 displays the calculated short-current enhancement $(\eta_{J_{sc}})$ at a fixed inner-shell (t) of the $Ge_{0.88}Sn_{0.12}$ layer equal to the core radius ($t = R_c$) and the dielectric capping layer thickness D was varied from 1 to 200 nm. In the top and left panels in Figure 6-9, the relative change-in percent- of the maximum short-current enhancement (*i.e.* a positive value means an enhancement or increase in the J_{sc}) is shown, whereas a negative value entails a deterioration or decay in J_{sc} relative to a CSNW system without the dielectric layer. Additionally, the antireflection role of the dielectric shell can be further confirmed from examining the absorption spectra. It can be seen that the dielectric shell of the Si/$Ge_{0.88}Sn_{0.12}$/Si_3N_4 NW gives rise to a broad absorption peak, clearly shown in Figure 6-9(b) and (c) for two distinct core radii (13.6 and 78.2 nm). So, a core radius R_c equal to 78.2 nm (green arrow in top panel in Figure 6-9(a)), an inner- shell thickness t equal to the core radius and a thickness of the dielectric capping layer D equal to 43 nm (blue arrow in left panel of Figure 6-9(a)) provides a 25% increase in the short-circuit current density as well as a high absorption efficiency. The enhancement at smaller core radius ($R_c < 20\ nm$; more specifically at $R_c = 13.6\ nm$, shown as an orange arrow in top panel of Figure 6-9(a) where ~40% increase in J_{sc} is achieved) and at a capping layer thickness of $D = 25\ nm$ occurs where the LMR whiskers are present. This enhancement is explained by an increase in scattering. In fact, in the case of a subwavelength NW, the increase in scattering is indicative of an enhanced optical antenna effect, which increases both scattering and absorption in the NW. This can be observed in Figure 6-10a. Likewise, tuning the spectral range of the absorption throughout the dielectric layer

thickness can be accomplished for a given core radius of 13.6 nm: in fact, when $D = 33$ nm, the structure will absorb in the visible spectrum, but when $D = 3$ nm the NIR spectrum will be active, with a 40% short-current enhancement compared to the $Si/Ge_{0.88}Sn_{0.12}$ CSNW structure. Furthermore, when the core radius is increased to 78 nm, the optimal Si_3Ni_4 capping layer thickness D is found to be 45 nm from Figure 6-9(c) with a corresponding short-current enhancement of 25%.

Next, the effect of the additional dielectric layer can be better understood in Figure 6-10(a) displaying TM-like mode absorption efficiency (Q_{abs}^{TM}) for three sets of NW structures: Si, $Si/Ge_{0.88}Sn_{0.12}$, and $Si/Ge_{0.88}Sn_{0.12}/Si_3N_4$ at $R_c = 13.6$ and $75\,nm$, and $D = 33$ and 45 nm, respectively for each core radii. Figure 6-10(b) represent the resonant profiles of the total TM-polarized Poynting vector $|\mathbf{S}|_{TM}^2$ inside the nanostructure and display a leaky-mode resonance behavior (see Figure 6-10(b) maps 5,10), which is associated with the selective scattering of light in a specific wavelength depending on the structure size. The NWs are investigated at wavelengths corresponding to the peaks labeled 1 to 10 in Figure 6-10(a). When coating the $Si/Ge_{0.88}Sn_{0.12}$ CSNW with Si_3N_4 layer, an increase of the absorption efficiency is apparent regardless of the core radius.

Note that adding a GeSn shell and increasing the core radius will induce a redshift in the LMR spectral position where higher order modes were observed to appear. Furthermore, the number of excited LMR diminishes due to the presence of the dielectric capping layer. The opportunity to control the spatial distribution of the energy flux density in the three previous structures, by introducing a shell layer, provides wavelength tuneability of the absorption efficiency which is clearer in the absorption maps presented in Figure 6-10(b). Besides, a simple dielectric shell can double light absorption and dramatically increase light scattering in Si core NWs by enhancing the optical antenna effect of the wires. This effect has been proven for different dielectric layers (SiO_2). [255]

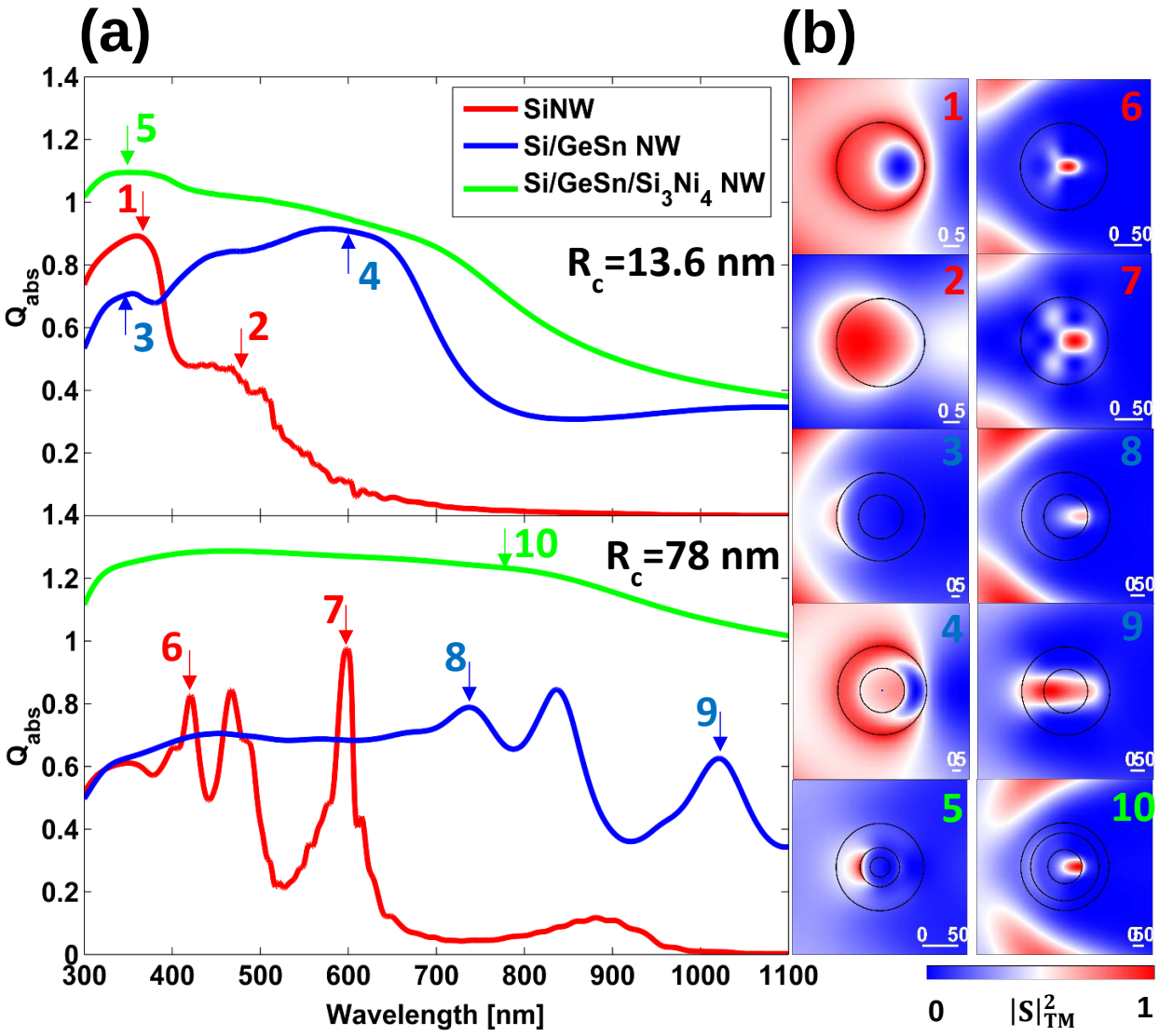

Figure 6-10: **(a)** TM-like mode absorption efficiency (Q_{abs}^{TM}) of the Si NW structure (red curve), Si/ $Ge_{0.88}Sn_{0.12}$ CSNW structure (blue curve) and Si/ $Ge_{0.88}Sn_{0.12}$/ Si_3N_4 structure (green curve), surrounded by air, for 2 different core radii: $R_c = 13.6$ and 78 nm. The GeSn shell thickness was fixed to the core radius and the dielectric capping layer D is chosen to be 33 and 45 nm, respectively for each core radius. The resonant peaks were labeled from 1 to 10 for the different structures. **(b)** Near field magnitude for the total TM-polarized Poynting vector $|\mathbf{S}|_{TM}^2$ by the three different structures evaluated with the analytical solution for a perpendicular incident illumination at the wavelengths corresponding to the peaks labeled 1−10 in panel (a). The corresponding scale bar is presented for each structure which reflects the dimension of the structure.

6.3 Conclusion

In conclusion, LMR-induced field enhancements were demonstrated inside $Ge_{1-x-y}Si_xSn_y$ alloy heterostructures and core-shell nanowires. Our theoretical calculations demonstrated that a ~14-fold increase in photocurrent can be achieved in $Si/Ge_{1-x-y}Si_xSn_y$ heterostructure as compared to bare Si. Furthermore, when the outer layer thickness decreases relative to the core radius in the core-shell nanowires, the maximum short-circuit current enhancement factor increases. Conversely, a thinner Sn-containing top layer limits the enhancement of light absorption in thin films. Moreover, the photocurrent increase in nanowire is found to be restricted to narrow regions (core radius $R_c < 56\,nm$ and shell thickness $t < 40\,nm$) where a significant enhancement relative to Si nanowires is achieved reaching 11-22-fold for $Si/Ge_{0.88}Sn_{0.12}$ and 25-47-fold for $Si/Ge_{0.84}Si_{0.04}Sn_{0.12}$ core-shell nanowires. Additionally, an extreme enhancement of light absorption for the Si/GeSn was shown, where the absorption efficiency in the near-infrared region is four orders of magnitude higher than that of SiNW. For $Ge/Ge_{1-y-x}Si_xSn_y$ core-shell nanowires the enhancement in light absorption is relatively limited as compared to $Si/Ge_{1-y-x}Si_xSn_y$ core- shell nanowires. The observed enhancement is due to a multiplication of contributions from LMRs in both core and shell semiconductors. These effects can be exploited through the control over the size and composition of the nanowire structure. Moreover, the calculations also suggest that the addition of a Si_3N_4 ARC layer on $Si/Ge_{1-y-x}Si_xSn_y$ core-shell nanowires improves the absorption efficiency. In fact, by tuning the core radius and the dielectric layer thickness, it is possible to selectively control the spectral range (visible or NIR) where the structure becomes optically active. For instance, with a core radius larger than 75 nm, a dielectric layer thickness of 40 nm, a 30% increase in the generated photocurrent relative to $Si/Ge_{1-y-x}Si_xSn_y$ core-shell nanowires can be achieved. The obtained results indicate that Si-based nanowire structures are more advantageous in terms of absorption enhancement as compared to thin films for applications in solar cells and photodetectors.

CHAPTER 7 CONCLUSION AND RECOMMENDATION

$Ge_{1-x-y}Si_xSn_y$ is a versatile group IV material system which has attracted great attention in recent years mainly for electronic and photonic applications. These semiconductors have relatively high electron and hole mobilities as compared to Si and Ge, making them promising candidates for high mobility channels in metal-oxide-semiconductor field effect transistors (MOSFETs) for the sub-7 nm technology nodes. Moreover, $Ge_{1-x-y}Si_xSn_y$ significantly extends the absorption edge range, and enhances the absorption coefficient of group IV semiconductors, as mentioned in Chapter 2. This makes $Ge_{1-x-y}Si_xSn_y$ an ideal platform to implement near-infrared (NIR) and mid-infrared (MIR) photodetectors and imaging devices. $Ge_{1-x-y}Si_xSn_y$ technologies are in principle CMOS-compatible, which is ideal for large-scale and cost-effective integration with standard semiconductor processing. In this chapter, we will highlight the key findings in this Master's thesis and outline our perspective for important directions and potential next steps to implement $Ge_{1-x-y}Si_xSn_y$ devices and harness their attractive properties.

7.1 Band gap engineering

To engineer efficient and scalable optoelectronic devices, theoretical investigations are needed to pave the way for material selection and performance optimization. The first task in this thesis has been the study of electronic structure of $Ge_{1-x-y}Si_xSn_y$ ternary alloys using a formalism that incorporates strain effect on the band structure, which can be used to accurately estimate the band edges relevant for heterostructure engineering. In chapter 4, we presented detailed investigations of the effect of composition and strain on the band structure of Sn-containing group IV semiconductors by adapting the second nearest neighbors empirical tight binding method (2NN-sp3s*). Furthermore, an efficient differential evolution approach was used through which the experimental effective masses and band gaps are accurately reproduced. In $Ge_{1-x-y}Si_xSn_y$, we found that tensile strain lowers the critical content of Sn needed to achieve a direct band gap semiconductor. For $0 \leq x \leq 0.4$ and $0 \leq y \leq 0.2$, the corresponding band gap energies are below 0.72 eV. In fully relaxed alloys, the direct band gap energy is located below 0.43 eV. We also found that the indirect-to-direct band gap transition crossover lines are given by $y = 0.605 \times x +$

0.077 and $y = 1.364 \times x + 0.107$ for tensile strained (pseudomorphic to Ge) and fully relaxed alloys, respectively. Furthermore, the effect of strain at a fixed composition was also investigated confirming that tensile strain facilitates the transition to a direct gap semiconductor, whereas the transition requires higher content of Sn under a compressive strain. Our results indicate that the interplay between composition and strain effects provides a rich playground to independently tune over a broad range the band gap energy and lattice parameter in group IV semiconductor. This progress in the understanding of the electronic structure of the material laid the groundwork for us to study the effect of free carrier doping density and core radius on the spatial localization of carriers inside core-shell NWs.

7.2 Properties of charge carriers in $Ge_{1-x-y}Si_xSn_y$ NW heterostructures

We started by analyzing a type I $Ge_{1-y}Sn_y$/Ge radial heterostructure for which we solved self-consistently the Schrödinger-Poisson equation for the $Ge_{1-y}Sn_y$/Ge core-shell NW system for two different Sn compositions: y <11% (indirect gap) or y >11% (direct gap). To that end, the conduction and valance band offsets of the heterostructure were determined by extracting the valence and conduction band edges. Moreover, the effect of doping on the spatial localization of electrons inside the radial core-shell NW was studied. One of the interesting findings is the ability to tune the electronic density localization inside the core-shell NW by controlling the doping concentration and the core and shell radii. For instance, when the core radius is below 20 nm and the free carrier doping concentration is 8×10^{17} cm^{-3}, the normalized core electron density variance for a $Ge_{0.9}Sn_{0.1}$/Ge CSNW was found to be 1.25, which translates to a core carrier confinement of electrons. A possible implication of this finding is to have a better estimation for the doping concentration and the geometrical properties of the NW to enhance the recombination process in an optoelectronic device. To complete the analysis, we also studied the effect of light interaction with $Ge_{1-x-y}Si_xSn_y$ CSNW structures where the absorption and scattering efficiencies of $Ge_{1-x-y}Si_xSn_y$ based thin films and CSNWs were quantified using the Lorentz-Mie scattering formalism.

7.3 Light absorption engineering in $Ge_{1-x-y}Si_xSn_y$ NW heterostructures

In Chapter 6, we measured the complex refractive index of $Ge_{1-y}Sn_y$ and $Ge_{1-x-y}Si_xSn_y$ for different Sn and Si compositions by SE. The optical properties were then used to evaluate theoretically the

absorption and scattering efficiencies as well as the photocurrent of $Ge_{1-x-y}Si_xSn_y$ based thin-films and core-shell NWs. Mie-Lorentz scattering formalism was used to evaluate these efficiencies. Our theoretical calculations demonstrated that a ~14-fold increase in photocurrent can be achieved in $Si/Ge_{1-x-y}Si_xSn_y$ thin-films as compared to bare Si. Furthermore, when the outer layer thickness decreases relative to the core radius in the core-shell NWs, the maximum short-circuit current enhancement factor increases. Conversely, a thinner Sn-containing top layer limits the enhancement of light absorption in thin films. Moreover, the photocurrent increase in NW is found to be restricted to narrow regions (core radius $R_c < 56\,nm$ and shell thickness $t < 40\,nm$) where a significant enhancement relative to Si NWs is achieved reaching 11- to 22-fold for $Si/Ge_{0.88}Sn_{0.12}$ and 25- to 47-fold for $Si/Ge_{0.84}Si_{0.04}Sn_{0.12}$ CSNWs. Additionally, an extreme enhancement of light absorption was predicted for the Si/GeSn CSNWs, where the absorption efficiency in the NIR region is four orders of magnitude higher than that of SiNW. Moreover, the calculations also suggest that the addition of Si_3N_4 as an anti-reflection coating layer on $Si/Ge_{1-x-y}Si_xSn_y$ CSNWs improves the absorption efficiency by tuning the core radius and the dielectric layer thickness to selectively control the spectral range (visible or NIR) where the structure becomes optically active. For instance, with a core radius larger than 75 nm, a dielectric layer thickness of 40 nm, a 30% increase in the generated photocurrent relative to $Si/Ge_{1-x-y}Si_xSn_y$ core-shell nanowires can be achieved. These findings are of paramount importance in the design of new optoelectronic devices. In the following, we outline a few examples of group IV optoelectronic devices that can be implemented and optimized based our investigations.

7.4 Future work

Theoretical investigations are a necessary tool to evaluate the basic properties of emerging semiconductors. Nevertheless, the experimental demonstration remains key to either validate or refute the findings of these theoretical tools. For that purpose, the obvious next steps emerging from this work is to develop Sn-containing group IV semiconductors and investigate their electronic and optical properties in the light of the results presented in this thesis. First, $Ge_{1-y}Sn_y$-based high-performance photodetectors (PDs), relevant for electronic-photonic integrated circuits (EPICs), are key components that enable optical links to convert light into electric signals. The optical absorption coefficients are largely enhanced in $Ge_{1-y}Sn_y$ and the absorption edge is

significantly extended toward longer wavelengths, thus forcing the detection range to expand beyond 2 μm. Because of the decoupled photon-absorption and carrier-collection paths in waveguide photodetectors (WGPD), simultaneous high-responsivity and high-speed operation can be achieved. For that purpose, a GeSn *p-i-n* WGPD can be engineered, as illustrated in Figure 7-1. The GeSn active layer can also be a GeSn/Ge multi-quantum well where a type-I heterostructure is introduced to confine carriers.

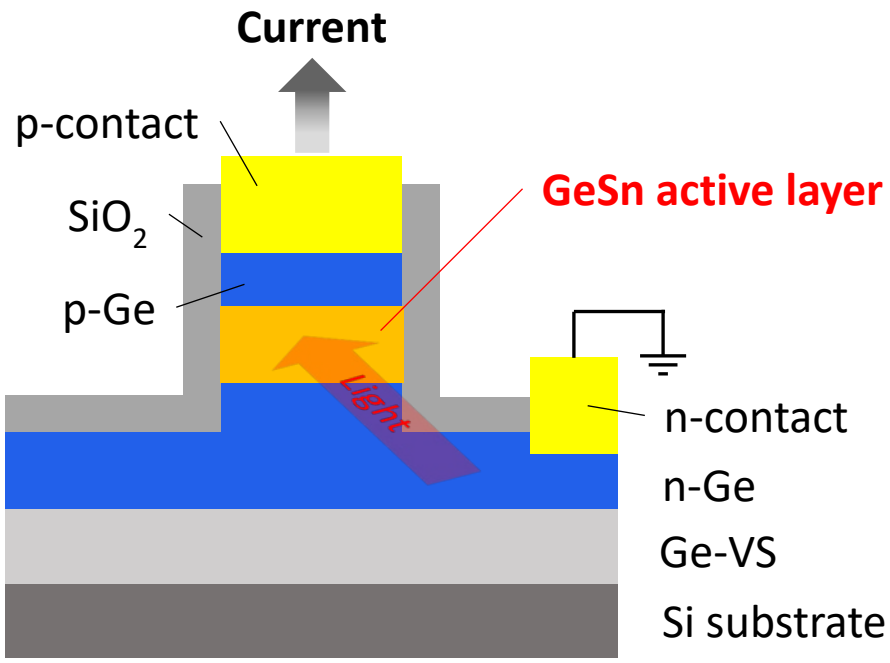

Figure 7-1: Cross-section illustration of a GeSn p-i-n WGPD

Second, extending the sp3s* tight binding formalism to evaluate the band structure of superlattices would be an important approach to engineer novel photonic group IV device structures. Nanostructuring permits the possibility to relax the constraints imposed by translational invariance and conversation of momentum which can induces band gap directness in superlattice. Additionally, alloying introduces extra degrees of freedom (strain and composition) to modify the band structure. Thus, combining nanostructuring with alloying can pave a path toward finding optically active, and direct gap system. For instance, Si/Ge superlattices has been extensively studied, experimentally and theoretically, and it has been shown that the optimal sequence for the Si/Ge superlattice is $SiGe_2Si_2Ge_2SiGe_n$. [256] Consequently, using the $Ge_{1-x-y}Si_xSn_y$ ternary alloy as a building block for a superlattice, will allow to decouple the effects of strain and composition

on the band structure. Computer-assisted search methods can be utilized to explore the $(Ge_{1-x_n-y_n}Si_{x_n}Sn_{y_n})_n/(Ge_{1-x_m-y_m}Si_{x_m}Sn_{y_m})_m$ superlattices with the explicit goal of finding a direct-gap and optically active material. This translates into finding the optimal Sn and Si concentrations (x, y) as well the number of monolayers (n, m) which renders it a computationally-expensive optimization procedure. Usually, first principle methods are used to evaluate electronic structure of superlattices. But, they limit the analysis to short-period superlattices (where n, m <10) due to computational overheat. Thus, using the sp3s* second-nearest neighbors approach as a substitute for computationally expensive first-principle method can extend the analysis to long-period superlattices, which will expand the search space. Furthermore, using a combination of differential genetic algorithms and band-structure calculation, we can identify the optimal motif that allows an increase of the dipole matrix element. So, an accurate evaluation of the dipole matrix element based upon the sp^3s^* approach is needed to finalize the framework needed to establish the optimal sequence for the superlattice optimization. Figure 7-2 shows a schematic sketch for a possible group IV superlattice.

Third, the most efficient solar cells currently in production uses lattice-matched Ge/GaInAs/GaInP triple-junctions grown on bulk Ge substrates. Although these architectures can achieve up to 40.7% efficiency by using solar concentrators, incorporating a fourth junction could provide further improvements in efficiency. To maximize the overall efficiency of solar cell multijunction, the band gaps of cell materials should cover the range from 0.6 to ~2.5 eV. Above 1.4 eV, III-V alloys (InGaAs, InGaP) are the materials of choice. At the low end of the energy spectra, Ge substrate is the most widely used for the bottom junction. In between the two ranges there lies a broad gap centered around 1.0 eV. Enhancing the absorption in this region is extremely important to improve the efficiency of multi-junction solar cells. However, to reach 1.0 eV bandgap using III-V alloys (InGaAs, InGaP) is relatively hard, while complying with lattice-matched condition. For that reason, $Ge_{1-x-y}Si_xSn_y$ is the perfect material candidate to be used because it can be easily lattice matched to Ge and have a tunable band gap that can reach ~1eV by accurately controlling the Sn and Si concentrations. The Si and Sn composition should be respectively between [1%,10%] and [4%,6%] to guarantee a lattice matched condition to Ge and $In_{0.08}Ga_{0.92}As$. Figure 7-3 shows a scheme of the cell in question.

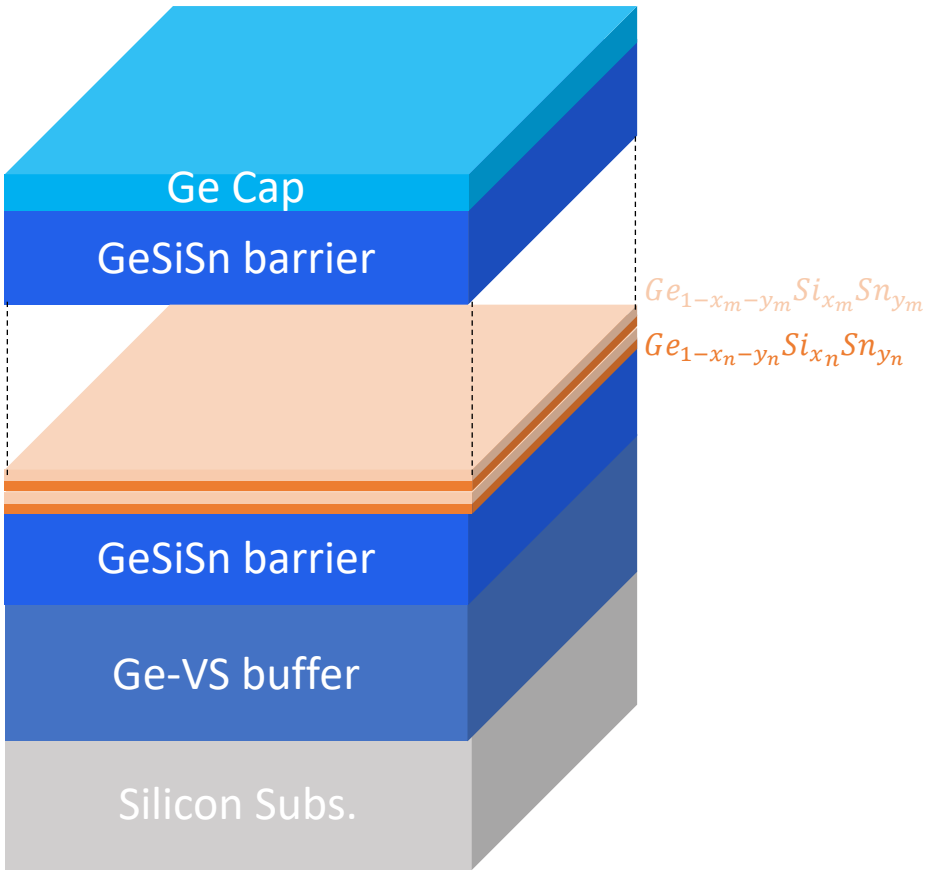

Figure 7-2: Schematic illustration of Group- IV $\left(Ge_{1-x_n-y_n}Si_{x_n}Sn_{y_n}\right)_n/\left(Ge_{1-x_m-y_m}Si_{x_m}Sn_{y_m}\right)_m$ Superlattices

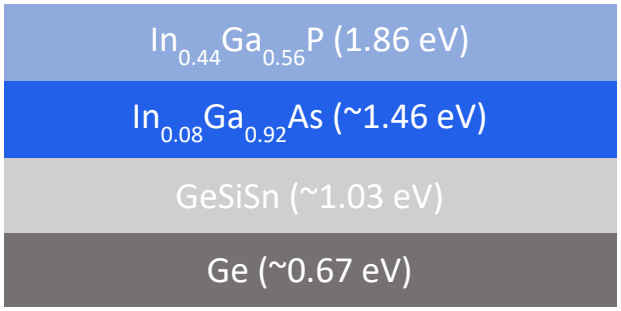

Figure 7-3: GeSiSn-based multi-junction solar cell with an optimal 1 eV sub-cell.

Nevertheless, tunnel junctions are an important part of the GeSiSn based solar cells that remain to be elucidated. Tunneling junctions are of paramount importance to form the connections between

consecutives p-n junctions. They function as an ohmic electrical contact in the middle of the semiconducting device.

Fourth, it is possible to design GeSn QW lasers that operate efficiently at room temperature. The necessary steps for this are elaborated below. Figure 7-4 depicts the schematic diagram of the proposed QW structure. The $Ge_{0.9}Sn_{0.1}$ QW, pseudomorphic to the Ge buffer layer, experiences a 1.1% compressive strain in the lattice structure. Based on the results discussed in Chapter 4, the 1.1% compressive strain forces the $Ge_{0.9}Sn_{0.1}$ to remain an indirect bandgap material. To overcome that constraint, a buffer layer with less lattice mismatch to $Ge_{0.9}Sn_{0.1}$ is desired. In this regard, a thick graded GeSn buffer layer can be grown where the Sn concentration is gradually increased to reach the condition to grow strain relaxed heterostructures. Therefore, the $Ge_{0.9}Sn_{0.1}$ QW could exhibit direct bandgap characteristics favorable for emitting light. Moreover, to provide sufficient carrier confinement in the GeSn QW layer, a SiGeSn cladding layer lattice matched to the new GeSn buffer can be used. Inserting that layer ensures the necessary barrier height due to the wider bandgap of SiGeSn compared to GeSn. Finally, a GeSn barrier layer lattice matched to GeSn buffer layer provides another level of confinement for the $Ge_{0.9}Sn_{0.1}$ QW region. The Sn composition of the GeSn buffer and barrier layers and the Si and Sn compositions of the lattice matched SiGeSn cladding layer should be carefully selected to provide the required direct bandgap $Ge_{0.9}Sn_{0.1}$ QW. To establish the desired values for the Sn composition in the $Ge_{1-y}Sn_y$ buffer layer, a contour plot of the energy difference between the Γ and L valleys ($\Delta E_c^{QW} = E_L - E_c$) *vs.* the Sn composition in the relaxed GeSn buffer and pseudomorphic GeSn well, need to be evaluated. Almost 10% Sn in the GeSn buffer layer is required to achieve direct band gap pseudomorphic $Ge_{0.9}Sn_{0.1}$ QW. However, this is not the only criteria that needs to be considered. The barrier height between the $Ge_{0.9}Sn_{0.1}$ QW and barrier layers plays a detrimental role in the design of the proposed structure. To that end, a map of the conduction band offset between the $Ge_{0.9}Sn_{0.1}$ QW and the GeSn buffer/barrier layers will help clarify the composition of the GeSn buffer layer. The GeSn buffer composition can be chosen to be between 4.5% and 5.5%. The next step in the QW structure design is to find the GeSiSn cladding layer lattice matched to the $Ge_{0.95}Sn_{0.05}$ buffer layer.

Figure 7-4: Direct band gap $Ge_{0.9}Sn_{0.1}$ QW with type-I band alignment and carrier confinement

Another reason that explains the use of 5% Sn in GeSn buffer layer is the critical thickness. A relaxed $Ge_{0.95}Sn_{0.05}$ buffer layer with the thickness of ~400nm is required because GeSn buffer layer with lower Sn content would not provide relaxed layer due to their critical thicknesses. Based on Vegard's law, the lattice constant of the $Ge_{0.95}Sn_{0.05}$ buffer layer is 5.6893 Å. Thus, both Si and Sn are required to provide a $Ge_{1-x-y}Si_xSn_y$ cladding layer with an in-plane lattice constant of 5.7 Å. Possible values for Si and Sn concentrations are in the range of 12-15% and 8.4-8.8%, respectively. This guarantees lattice matching condition as well as large band offsets between GeSiSn and the $Ge_{0.9}Sn_{0.1}$ layer in the order of ~100meV, which is higher than the thermal fluctuation energy of 25 meV.

To sum up, $Ge_{1-x-y}Si_xSn_y$ materials represent an exciting family of semiconductors for group IV-based light emitting devices, photodetectors, and low-power nanoelectronics devices. In the future, the next steps in this direction are better understanding and control the out-of-equilibrium growth dynamics of GeSiSn to be able to fabricate these devices. Furthermore, establishing accurate estimation of the conduction and valence band-offset of the $Ge_{1-x-y}Si_xSn_y$ superlattice, understanding the interplay between the strain and composition effect on the optical gap activity, and controlling the two doping types are key milestones towards the experimental implementation of these devices.

BIBLIOGRAPHY

[1] CISCO 2015 The Zettabyte Era: Trends and Analysis *Cisco* 1–29

[2] Moore G E 1965 Cramming more components onto integrated circuits (Reprinted from Electronics, pg 114-117, April 19, 1965) *Proc. IEEE* **86** 82–5

[3] International Rodamap Committee 2015 *International Technology Roadmap for Semiconductors 2.0: Executive Report*

[4] Vandenberghe L, Boyd S and Gamal A El 1998 Optimizing dominant time constant in rc circuits *IEEE Trans. Comput. Des. Integr. Circuits Syst.* **17** 110–25

[5] Anon 2000 International Technology Roadmap for Semiconductors *ITRS2.0*

[6] Delforge P and Whitney J 2014 Data Center Efficiency Assessment *Nat. Resour. Def. Counc.* 35

[7] Schien D 2014 ICT Innovations for Sustainability *Ser. Adv. Intell. Syst. Comput.* **310** 157

[8] V. C. Coroama et al 2014 ICT Innovations for Sustainability *Ser. Adv. Intell. Syst. Comput.* **310** 137

[9] Koomey J G 2011 Growth in Data Center Electricity use 2005 to 2010

[10] Tucker R S 2013 Research at the University of Melbourne's Centre for Energy-Efficient Telecommunications *IEEE Photonics Society* vol 27

[11] Dreibholz T, Becke M and Adhari H 2007 *Report to Congress on Server and Data Center Energy Efficiency Public Law 109-431* vol 109

[12] Pavesi, Lorenzo and Lockwood D J (Eds. . 2016 *Silicon Photonics III: Systems and Applications* ed D J (Eds. . Pavesi, Lorenzo, Lockwood (Springer-Verlag Berlin Heidelberg)

[13] Soref R 2010 Mid-infrared photonics in silicon and germanium *Nat. Photonics* **4** 495–7

[14] Soref R, Buca D and Yu S-Q 2016 Group IV Photonics: Driving Integrated Optoelectronics *Opt. Photonics News* **27** 32–9

[15] Zhou Z, Yin B and Michel J 2015 On-chip light sources for silicon photonics *Light Sci. Appl.* **4** 1–13

[16] Rickman A 2014 The commercialization of silicon photonics *Nat. Photonics* **8** 579–82

[17] Liang D, Roelkens G, Baets R and Bowers J E 2010 Hybrid Integrated Platforms for Silicon Photonics *Materials (Basel).* **3** 1782–802

[18] Sun C, Wade M T, Lee Y, Orcutt J S, Alloatti L, Georgas M S, Waterman A S, Shainline J M, Avizienis R R, Lin S, Moss B R, Kumar R, Pavanello F, Atabaki A H, Cook H M, Ou A J, Leu J C, Chen Y-H, Asanović K, Ram R J, Popović M A and Stojanović V M 2015 Single-chip microprocessor that communicates directly using light *Nature* **528** 534

[19] Åberg I, Ackland B, Beach J V, Godek C, Johnson R, King C A, Lattes A, O'Neill J, Pappas S, Sriram T S and Rafferty C S 2010 A low dark current and high quantum efficiency monolithic germanium-on-silicon (CMOS) imager technology for day and night imaging applications *2010 International Electron Devices Meeting* p 14.4.1--14.4.4

[20] Miller D A B 2017 Attojoule Optoelectronics for Low-Energy Information Processing and Communications *J. Light. Technol.* **35** 346–96

[21] Liu J, Michel J, Giziewicz W, Pan D, Wada K, Cannon D D, Jongthammanurak S, Danielson D T, Kimerling L C, Chen J, Ilday F Ö, Kärtner F X and Yasaitis J 2005 High-performance, tensile-strained Ge p-i-n photodetectors on a Si platform *Appl. Phys. Lett.* **87** 103501

[22] Liu J, Cannon D D, Wada K, Ishikawa Y, Jongthammanurak S, Danielson D T, Michel J and Kimerling L C 2005 Tensile strained Ge p-i-n photodetectors on Si platform for C and L band telecommunications *Appl. Phys. Lett.* **87** 011110

[23] Ishikawa Y, Wada K, Cannon D D, Liu J, Luan H-C and Kimerling L C 2003 Strain-induced band gap shrinkage in Ge grown on Si substrate *Appl. Phys. Lett.* **82** 2044–6

[24] Hansen M P and Malchow D S 2008 Overview of SWIR detectors, cameras, and applications *SPIE* vol 6939 p 69390I

[25] Rafferty C, King C, Ackland B, O'Neill J, Aberg I, Sriram T S, Mackay A and Johnson R 2008 Monolithic germanium SWIR imaging array *2008 IEEE Int. Conf. Technol. Homel. Secur. HST'08* 577–82

[26] Chen H, Asif M S, Sankaranarayanan A C and Veeraraghavan A 2015 FPA-CS: Focal plane

array-based compressive imaging in short-wave infrared *Proc. IEEE Comput. Soc. Conf. Comput. Vis. Pattern Recognit.* **07**–**12**–**June** 2358–66

[27] Bazovkin V M, Dvoretsky S A, Guzev A A, Kovchavtsev A P, Marin D V., Polovinkin V G, Sabinina I V., Sidorov G Y, Tsarenko A V., Vasil'Ev V V., Varavin V S and Yakushev M V. 2016 High operating temperature SWIR p+-n FPA based on MBE-grown HgCdTe/Si(013) *Infrared Phys. Technol.* **76** 72–4

[28] Kleipool Q L, Jongma R T, Gloudemans A M S, Schrijver H, Lichtenberg G F, van Hees R M, Maurellis A N and Hoogeveen R W M 2007 In-flight proton-induced radiation damage to SCIAMACHY's extended-wavelength InGaAs near-infrared detectors *Infrared Phys. Technol.* **50** 30–7

[29] Schmitt J 1999 Optical Coherence Tomography (OCT): A Review *IEEE J. Sel. Top. Quantum Electron.* **5** 1205–15

[30] Pralle M U, Carey J E, Homayoon H, Sickler J, Li X, Jiang J, Sahebi F, Palsule C and McKee J 2013 Infrared enhanced detection for laser imaging and biometrics *Proc. SPIE* **8734** 87340H–87340H–7

[31] Mcdonald S A, Konstantatos G, Zhang S, Cyr P W, Klem E J D, Levina L and Sargent E H 2005 Solution-processed PbS quantum dot infrared photodetectors and photovoltaics *Nat. Mater.* **4** 138–42

[32] Muñoz A, Meléndez J, Torquemada M C, Rodrigo M T, Cebrián J, de Castro A J, Meneses J, Ugarte M, López F, Vergara G, Hernández J L, Martín J M, Adell L and Montojo M T 1998 PbSe photodetector arrays for IR sensors *Thin Solid Films* **317** 425–8

[33] Wang J, Hu J, Becla P, Agarwal A M and Kimerling L C 2010 Resonant-cavity-enhanced mid-infrared photodetector on a silicon platform. *Opt. Express* **18** 12890–6

[34] Rogalski A 1999 Assessment of HgCdTe photodiodes and quantum well infrared photoconductors for long wavelength focal plane arrays *Infrared Phys. Technol.* **40** 279–94

[35] Mokkapati S and Jagadish C 2009 III-V compound SC for optoelectronic devices *Mater. Today* **12** 22–32

[36] Yang Y, Zhang Y H, Shen W Z and Liu H C 2011 Semiconductor infrared up-conversion

devices *Prog. Quantum Electron.* **35** 77–108

[37] Razeghi M 1998 Current status and future trends of infrared detectors *Opto-Electronics Rev.* **6** 155–94

[38] Gupta S, Magyari-Köpe B, Nishi Y and Saraswat K C 2013 Achieving direct band gap in germanium through integration of Sn alloying and external strain *J. Appl. Phys.* **113** 73707

[39] Eckhardt C, Hummer K and Kresse G 2014 Indirect-to-direct gap transition in strained and unstrained Sn_xGe_{1-x} alloys *Phys. Rev. B* **89** 165201

[40] Attiaoui A and Moutanabbir O 2014 Indirect-to-direct band gap transition in relaxed and strained $Ge_{1-x-y}Si_xSn_y$ ternary alloys *J. Appl. Phys.* **116** 063712

[41] He G and Atwater H A 1997 Interband Transitions in Sn_xGe_{1-x} Alloys *Phys. Rev. Lett.* **79** 1937–40

[42] D'Costa V R, Cook C S, Birdwell A G, Littler C L, Canonico M, Zollner S, Kouvetakis J and Menéndez J 2006 Optical critical points of thin-film $Ge_{1-y}Sn_y$ alloys: A comparative $Ge_{1-y}Sn_y/Ge_{1-x}Si_x$ study *Phys. Rev. B* **73** 125207

[43] Yin W-J, Gong X-G and Wei S-H 2008 Origin of the unusually large band-gap bowing and the breakdown of the band-edge distribution rule in the $Ge_{1-x}Sn_x$ alloys *Phys. Rev. B* **78** 161203

[44] Mathews J, Beeler R T, Tolle J, Xu C, Roucka R, Kouvetakis J and Menéndez J 2010 Direct-gap photoluminescence with tunable emission wavelength in $Ge_{1-y}Sn_y$ alloys on silicon *Appl. Phys. Lett.* **97** 221912

[45] Chen R, Lin H, Huo Y, Hitzman C, Kamins T I and Harris J S 2011 Increased photoluminescence of strain-reduced, high-Sn composition $Ge_{1-x}Sn_x$ alloys grown by molecular beam epitaxy *Appl. Phys. Lett.* **99** 181125

[46] Lin H, Chen R, Lu W, Huo Y, Kamins T I and Harris J S 2012 Investigation of the direct band gaps in $Ge_{1-x}Sn_x$ alloys with strain control by photoreflectance spectroscopy *Appl. Phys. Lett.* **100** 102109

[47] Gallagher J D, Senaratne C L, Kouvetakis J and Menéndez J 2014 Compositional dependence of the bowing parameter for the direct and indirect band gaps in $Ge_{1-y}Sn_y$ alloys

Appl. Phys. Lett. **105** 142102

[48] D'Costa V R, Wang W and Yeo Y-C 2016 Near-bandgap optical properties of pseudomorphic GeSn alloys grown by molecular beam epitaxy *J. Appl. Phys.* **120** 63104

[49] Lu Low K, Yang Y, Han G, Fan W and Yeo Y-C 2012 Electronic band structure and effective mass parameters of $Ge_{1-x}Sn_x$ alloys *J. Appl. Phys.* **112** 103715–9

[50] Gong X, Han G, Bai F, Su S, Guo P, Yang Y, Cheng R, Zhang D, Zhang G, Xue C, Cheng B, Pan J, Zhang Z, Tok E S, Antoniadis D and Yeo Y C 2013 Germanium-Tin (GeSn) p-Channel MOSFETs Fabricated on (100) and (111) Surface Orientations With Sub-400 C Si_2H_6 Passivation *IEEE Electron Device Lett.* **34** 339–41

[51] Guo P, Han G, Gong X, Liu B, Yang Y, Wang W, Zhou Q, Pan J, Zhang Z, Soon Tok E and Yeo Y-C 2013 $Ge_{0.97}Sn_{0.03}$ p-channel metal-oxide-semiconductor field-effect transistors: Impact of Si surface passivation layer thickness and post metal annealing *J. Appl. Phys.* **114** 44510

[52] Lieten R R, Maeda T, Jevasuwan W, Hattori H, Uchida N, Miura S, Tanaka M and Locquet J-P 2013 Tensile-Strained GeSn Metal–Oxide–Semiconductor Field-Effect Transistor Devices on Si(111) Using Solid Phase Epitaxy *Appl. Phys. Express* **6** 101301

[53] Oehme M, Kostecki K, Ye K, Bechler S, Ulbricht K, Schmid M, Kaschel M, Gollhofer M, Körner R, Zhang W, Kasper E and Schulze J 2014 GeSn-on-Si normal incidence photodetectors with bandwidths more than 40 GHz *Opt. Express* **22** 839–46

[54] Oehme M, Widmann D, Kostecki K, Zaumseil P, Schwartz B, Gollhofer M, Koerner R, Bechler S, Kittler M, Kasper E and Schulze J 2014 GeSn/Ge multiquantum well photodetectors on Si substrates *Opt. Lett.* **39** 4711–4

[55] Zhang D, Xue C, Cheng B, Su S, Liu Z, Zhang X, Zhang G, Li C and Wang Q 2013 High-responsivity GeSn short-wave infrared p-i-n photodetectors *Appl. Phys. Lett.* **102** 141111

[56] Su S, Cheng B, Xue C, Wang W, Cao Q, Xue H, Hu W, Zhang G, Zuo Y and Wang Q 2011 GeSn p-i-n photodetector for all telecommunication bands detection *Opt. Express, OE* **19** 6400–5

[57] Conley B R, Mosleh A, Ghetmiri S A, Du W, Soref R A, Sun G, Margetis J, Tolle J, Naseem

H A and Yu S-Q 2014 Temperature dependent spectral response and detectivity of GeSn photoconductors on silicon for short wave infrared detection *Opt. Express, OE* **22** 15639–52

[58] Gassenq A, Gencarelli F, Van Campenhout J, Shimura Y, Loo R, Narcy G, Vincent B and Roelkens G 2012 GeSn/Ge heterostructure short-wave infrared photodetectors on silicon. *Opt. Express* **20** 27297–303

[59] Wirths S, Geiger R, Driesch N V Den, Mussler G, Stoica T, Mantl S, Ikonic Z, Luysberg M, Chiussi S, Hartmann J M, Sigg H, Faist J, Buca D and Grützmacher D 2015 Lasing in direct-bandgap GeSn alloy grown on Si *Nat. Photonics* **9** 88–92

[60] Schwartz B, Oehme M, Kostecki K, Widmann D, Gollhofer M, Koerner R, Bechler S, Fischer I A, Wendav T, Kasper E, Schulze J and Kittler M 2015 Electroluminescence of GeSn/Ge MQW LEDs on Si substrate *Opt. Lett.* **40** 3209–12

[61] Oehme M, Werner J, Gollhofer M, Schmid M, Kaschel M, Kasper E and Schulze J 2011 Room-Temperature Electroluminescence From GeSn Light-Emitting Pin Diodes on Si *IEEE Photonics Technol. Lett.* **23** 1751–3

[62] Roucka R, Mathews J, Beeler R T, Tolle J, Kouvetakis J and Menéndez J 2011 Direct gap electroluminescence from Si/$Ge_{1-y}Sn_y$ p-i-n heterostructure diodes *Appl. Phys. Lett.* **98** 061109

[63] Du W, Ghetmiri S A, Conley B R, Mosleh A, Nazzal A, Soref R A, Sun G, Tolle J, Margetis J, Naseem H A and Yu S Q 2014 Competition of optical transitions between direct and indirect bandgaps in $Ge_{1-x}Sn_x$ *Appl. Phys. Lett.* **105** 5–6

[64] Zhao J and Green M A 1991 Optimized antireflection coatings for high-efficiency silicon solar cells *IEEE Trans. Electron Devices* **38** 1925–34

[65] Rim S-B, Zhao S, Scully S R, McGehee M D and Peumans P 2007 An effective light trapping configuration for thin-film solar cells *Appl. Phys. Lett.* **91** 243501

[66] Kuo M-L, Poxson D J, Kim Y S, Mont F W, Kim J K, Schubert E F and Lin S-Y 2008 Realization of a near-perfect antireflection coating for silicon solar energy utilization *Opt. Lett., OL* **33** 2527–9

[67] Pauzauskie P J and Yang P 2006 Nanowire photonics *Nat. Photonics* **9** 36–45

[68] Goodman C H L 1983 Direct-gap group IV semiconductors based on tin *IEE Proc. I Solid State Electron Devices* **130** 46

[69] Olesinski R W and Abbaschian G J 1984 The Ge-Sn (Germanium-Tin) system *Bull. Alloy Phase Diagrams* **5** 265–71

[70] Wirths S, Buca D and Mantl S 2016 Si-Ge-Sn alloys: From growth to applications *Prog. Cryst. Growth Charact. Mater.* **62** 1–39

[71] Amrane N, Ait Abderrahmane S and Aourag H 1995 Band structure calculation of GeSn and SiSn *Infrared Phys. Technol.* **36** 843–8

[72] Zaoui A, Ferhat M, Certier M, Khelifa B and Aourag H 1996 Optical properties of SiSn and GeSn *Infrared Phys. Technol.* **37** 483–8

[73] Alberi K, Blacksberg J, Bell L D, Nikzad S, Yu K M, Dubon O D and Walukiewicz W 2008 Band anticrossing in highly mismatched Sn_xGe_{1-x} semiconducting alloys *Phys. Rev. B* **77** 073202

[74] Attiaoui A and Moutanabbir O 2014 Optical and Electronic Propreties of GeSn and GeSiSn Heterostructures and Nanowires *ECS Trans.* **64** 869–79

[75] Brudevoll T, Citrin D S, Christensen N E and Cardona M 1993 Calculated band structure of zinc-blende-type SnGe *Phys. Rev. B* **48** 17128–37

[76] Shen J, Zi J, Xie X and Jiang P 1997 Ab initio Calculation of the structure of the random alloys $Ge_{1-x}Sn_x$ *Phys. Rev. B* **56** 12084–7

[77] Pandey R, Rérat M and Causà M 1999 First-principles study of stability, band structure, and optical properties of the ordered $Ge_{0.50}Sn_{0.50}$ alloy *Appl. Phys. Lett.* **75** 4127–9

[78] Moontragoon P, Ikonić Z and Harrison P 2007 Band structure calculations of Si–Ge–Sn alloys: achieving direct band gap materials *Semicond. Sci. Technol.* **22** 742

[79] Beeler R, Roucka R, Chizmeshya A V G, Kouvetakis J and Menéndez J 2011 Nonlinear structure-composition relationships in the $Ge_{1-y}Sn_y$/Si(100) ($y<0.15$) system *Phys. Rev. B* **84** 035204

[80] Lee M-H, Liu P-L, Hong Y-A, Chou Y-T, Hong J-Y and Siao Y-J 2013 Electronic band structures of $Ge_{1-x}Sn_x$ semiconductors: A first-principles density functional theory study *J. Appl. Phys.* **113** 063517

[81] Al-Kabi S, Ghetmiri S A, Margetis J, Du W, Mosleh A, Alher M, Dou W, Grant J M, Sun G, Soref R A, Tolle J, Li B, Mortazavi M, Naseem H A and Yu S-Q 2016 Optical Characterization of Si-Based $Ge_{1-x}Sn_x$ Alloys with Sn Compositions up to 12% *J. Electron. Mater.* **45** 2133–41

[82] Wegscheider W, Eberl K, Menczigar U and Abstreiter G 1990 Single-crystal Sn/Ge superlattices on Ge substrates: Growth and structural properties *Appl. Phys. Lett.* **57** 875–7

[83] Bauer M, Taraci J, Tolle J, Chizmeshya A V G, Zollner S, Smith D J, Menendez J, Hu C and Kouvetakis J 2002 Ge–Sn semiconductors for band-gap and lattice engineering *Appl. Phys. Lett.* **81** 2992–4

[84] Chizmeshya A V G, Bauer M R and Kouvetakis J 2003 Experimental and Theoretical Study of Deviations from Vegard's Law in the Sn_xGe_{1-x} System *Chem. Mater.* **15** 2511–9

[85] Ladrón de Guevara H P, Rodríguez A G, Navarro-Contreras H and Vidal M A 2004 Determination of the optical energy gap of $Ge_{1-x}Sn_x$ alloys with $0<x<0.14$ *Appl. Phys. Lett.* **84** 4532–4

[86] Grzybowski G, Beeler R T, Jiang L, Smith D J, Kouvetakis J and Menéndez J 2012 Next generation of $Ge_{1-y}Sn_y$ ($y = 0.01$-0.09) alloys grown on Si(100) via Ge_3H_8 and SnD_4: Reaction kinetics and tunable emission *Appl. Phys. Lett.* **101** 072105

[87] Dybała F, Żelazna K, Maczko H, Gladysiewicz M, Misiewicz J, Kudrawiec R, Lin H, Chen R, Shang C, Huo Y, Kamins T I and Harris J S 2016 Electromodulation spectroscopy of direct optical transitions in $Ge_{1-x}Sn_x$ layers under hydrostatic pressure and built-in strain *J. Appl. Phys.* **119** 215703

[88] Chibane Y, Bouhafs B and Ferhat M 2003 Unusual structural and electronic properties of Sn_xGe_{1-x} alloys *Phys. status solidi* **240** 116–9

[89] Chibane Y and Ferhat M 2010 Electronic structure of Sn_xGe_{1-x} alloys for small Sn compositions: Unusual structural and electronic properties *J. Appl. Phys.* **107** 053512

[90] Annane F and Bouarrissa N 2002 Electronic properties and elastic constants of the ordered $Ge_{1-x}Sn_x$ alloys - ScienceDirect *Mater. Sci. Eng. B* **95** 100–6

[91] Bouhafs B, Benkabou F, Ferhat M, Khelifa B, Dufour J P and Aourag H 1995 Energy band structure calculation of Ge_xSn_{1-x} and Si_xSn_{1-x} alloys *Infrared Phys. Technol.* **36** 967–72

[92] Mäder K A, Baldereschi A and von Känel H 1989 Band structure and instability of $Ge_{1-x}Sn_x$ alloys *Solid State Commun.* **69** 1123–6

[93] Jenkins D W and Dow J D 1987 Electronic properties of metastable $Ge_{1-x}Sn_x$ alloys *Phys. Rev. B* **36** 7994–8000

[94] Sau J D and Cohen M L 2007 Possibility of increased mobility in Ge-Sn alloy system *Phys. Rev. B* **75** 045208

[95] Dutt B, Lin H, Sukhdeo D S, Vulovic B M, Gupta S, Nam D, Saraswat K C and Jr J S H 2013 Theoretical Analysis of GeSn Alloys as a Gain Medium for a Si-Compatible Laser *IEEE J. Sel. Top. Quantum Electron.* **19** 1502706–1502706

[96] Zhu Z, Xiao J, Sun H, Hu Y, Cao R, Wang Y, Zhao L and Zhuang J 2015 Composition-dependent band gaps and indirect–direct band gap transitions of group-IV semiconductor alloys *Phys. Chem. Chem. Phys.* **17** 21605–10

[97] Cheng T-H, Peng K-L, Ko C-Y, Chen C-Y, Lan H-S, Wu Y-R, Liu C W and Tseng H-H 2010 Strain-enhanced photoluminescence from Ge direct transition *Appl. Phys. Lett.* **96** 211108

[98] Gassenq A, Guilloy K, Osvaldo Dias G, Pauc N, Rouchon D, Hartmann J-M, Widiez J, Tardif S, Rieutord F, Escalante J, Duchemin I, Niquet Y-M, Geiger R, Zabel T, Sigg H, Faist J, Chelnokov A, Reboud V and Calvo V 2015 1.9% bi-axial tensile strain in thick germanium suspended membranes fabricated in optical germanium-on-insulator substrates for laser applications *Appl. Phys. Lett.* **107** 191904

[99] Capellini G, Kozlowski G, Yamamoto Y, Lisker M, Wenger C, Niu G, Zaumseil P, Tillack B, Ghrib A, De Kersauson M, El Kurdi M, Boucaud P and Schroeder T 2013 Strain analysis in SiN/Ge microstructures obtained via Si-complementary metal oxide semiconductor compatible approach *J. Appl. Phys.* **113**

[100] Nam D, Sukhdeo D, Roy A, Balram K, Cheng S-L, Huang K C-Y, Yuan Z, Brongersma M, Nishi Y, Miller D and Saraswat K 2011 Strained germanium thin film membrane on silicon substrate for optoelectronics *Opt. Express* **19** 25866

[101] Reboud V, Gassenq A, Pauc N, Aubin J, Milord L, Thai Q M, Bertrand M, Guilloy K, Rouchon D, Rothman J, Zabel T, Armand Pilon F, Sigg H, Chelnokov A, Hartmann J M and Calvo V 2017 Optically pumped GeSn micro-disks with 16% Sn lasing at 3.1 μm up to 180 K *Appl. Phys. Lett.* **111**

[102] Lieten R R, Seo J W, Decoster S, Vantomme A, Peters S, Bustillo K C, Haller E E, Menghini M and Locquet J-P 2013 Tensile strained GeSn on Si by solid phase epitaxy *Appl. Phys. Lett.* **102** 052106

[103] Du W, Ghetmiri S, Al-Kabi S, Mosleh A, Pham T, Zhou Y, Tran H, Sun G, Soref R, Margetis J, Tolle J, Li B, Mortazavi M, Naseem H and Yu S-Q 2017 Silicon-based Ge0.89Sn0.11 photodetector and light emitter towards mid-infrared applications *Silicon Photonics XII* vol 10108 (International Society for Optics and Photonics) p 1010813

[104] Polak M P, Scharoch P and Kudrawiec R 2017 The electronic band structure of Ge1− x Snx in the full composition range: indirect, direct, and inverted gaps regimes, band offsets, and the Burstein–Moss effect *J. Phys. D. Appl. Phys.* **50** 195103

[105] Lan H-S and Liu C W 2017 Valence band structure calculations of strained $Ge_{1-x}Sn_x$ quantum well pFETs. *ArXiv e-prints* **1703.01812** 1–6

[106] Van de Walle C G 1989 Band lineups and deformation potentials in the model-solid theory *Phys. Rev. B* **39** 1871–83

[107] Chou H Y, Afanas'Ev V V., Houssa M, Stesmans A, Vincent B, Gencarelli F, Shimura Y, Merckling C, Loo R, Nakatsuka O and Zaima S 2014 Band alignment at interfaces of amorphous Al_2O_3 with $Ge_{1-x}Sn_x$ and strained Ge-based channels *Appl. Phys. Lett.* **104**

[108] Ye K, Zhang W, Oehme M, Schmid M, Gollhofer M, Kostecki K, Widmann D, Körner R, Kasper E and Schulze J 2015 Absorption coefficients of GeSn extracted from PIN photodetector response *Solid. State. Electron.* **110** 71–5

[109] Agrawal G E 2002 *Fiber-Optic Communication Systems* (New-York: John Wiley and sons)

[110] Pantellides S and Zollner S 2002 *Silicon-Germanium Carbon Alloys: Growth, Properties and Applications* vol 15 (New-York: Taylor and Francis)

[111] Xie J, Tolle J, D'Costa V R, Chizmeshya A V G, Menéndez J and Kouvetakis J 2009 Direct integration of active $Ge_{1-x}(Si4Sn)_x$ semiconductors on Si(100) *Appl. Phys. Lett.* **95** 181909

[112] D'Costa V R, Cook C S, Menéndez J, Tolle J, Kouvetakis J and Zollner S 2006 Transferability of optical bowing parameters between binary and ternary group-IV alloys *Solid State Commun.* **138** 309–13

[113] D'Costa V R, Fang Y-Y, Tolle J, Kouvetakis J and Menéndez J 2009 Tunable Optical Gap at a Fixed Lattice Constant in Group-IV Semiconductor Alloys *Phys. Rev. Lett.* **102** 107403

[114] D'Costa V R, Fang Y-Y, Tolle J, Kouvetakis J and Menéndez J 2010 Ternary GeSiSn alloys: New opportunities for strain and band gap engineering using group-IV semiconductors *Thin Solid Films* **518** 2531–7

[115] Chang G, Chang S and Chuang S L 2009 Theory for n-type doped , tensile-strained Ge – Si x Ge y Sn 1 − x − y quantum-well lasers at telecom wavelength Abstract : **17** 11246–58

[116] Sun G, Soref R a. and Cheng H H 2010 Design of an electrically pumped SiGeSn/GeSn/SiGeSn double-heterostructure midinfrared laser *J. Appl. Phys.* **108** 033107

[117] Chang G E, Chang S W and Chuang S L 2010 Strain-Balanced $Ge_zSn_{1-z}/Si_xSn_yGe_{1-x-y}$ Multiple-Quantum-Well Lasers *IEEE J. Quantum Electron.* **46** 1813–20

[118] Stange D, Wirths S, Geiger R, Schulte-Braucks C, Marzban B, Driesch N V Den, Mussler G, Zabel T, Stoica T, Hartmann J-M, Mantl S, Ikonic Z, Grützmacher D, Sigg H, Witzens J and Buca D 2016 Optically Pumped GeSn Microdisk Lasers on Si *ACS Photonics* **3** 1279–85

[119] Stange D, Dendriesch N Von, Rainko D, Roesgaard Sø, Povstugar I, Hartman J-M, Stoica T, Ikonic Z, Mantl S, GrÜtzmacher D and Buca D 2017 Short-wave infrared LEDs from GeSn/SiGeSn multiple quantum wells *Optica* **4** 185–8

[120] Ventura C I, Querales Flores J D, Fuhr J D and Barrio R A 2015 Electronic structure of $Ge_{1-x-y}Si_xSn_y$ ternary alloys for multijunction solar cells *Prog. Photovoltaics Res. Appl.* **23** 112–8

[121] Lin H, Chen R, Lu W, Huo Y, Kamins T I and Harris J S 2012 Structural and optical characterization of $Si_xGe_{1-x-y}Sn_y$ alloys grown by molecular beam epitaxy *Appl. Phys. Lett.* **100** 141908

[122] Aella P, Cook C, Tolle J, Zollner S, Chizmeshya A V G and Kouvetakis J 2004 Optical and structural properties of $Si_xSn_yGe_{1-x-y}$ alloys *Appl. Phys. Lett.* **84** 888–90

[123] Beeler R T, Xu C, Smith D J, Grzybowski G, Menéndez J and Kouvetakis J 2012 Compositional dependence of the absorption edge and dark currents in $Ge_{1-x-y}Si_xSn_y$/Ge(100) photodetectors grown via ultra-low-temperature epitaxy of Ge_4H_{10}, Si_4H_{10}, and SnD_4 *Appl. Phys. Lett.* **101** 221111–5

[124] Beeler R T, Menéndez J, Smith D J and Kouvetakis J 2013 High Performance Group IV Photodiodes with Tunable Absorption Edges based on Ternary SiGeSn Alloys *ECS Trans.* **50** 591–9

[125] Xu C, Jiang L, Kouvetakis J and Menéndez J 2013 Optical properties of $Ge_{1-x-y}Si_xSn_y$ alloys with y > x: Direct bandgaps beyond 1550 nm *Appl. Phys. Lett.* **103** 1–5

[126] Gallagher J D, Xu C, Jiang L, Kouvetakis J and Menéndez J 2013 Fundamental band gap and direct-indirect crossover in $Ge_{1-x-y}Si_xSn_y$ alloys *Appl. Phys. Lett.* **103** 202104

[127] Slater J C and Koster G F 1954 Simplified LCAO Method for the Periodic Potential Problem *Phys. Rev.* **94** 1498–524

[128] Vogl P, Hjalmarson H P and Dow J D 1983 A Semi-empirical tight-binding theory of the electronic structure of semiconductors† *J. Phys. Chem. Solids* **44** 365–78

[129] Jancu J-M, Scholz R, Beltram F and Bassani F 1998 Empirical $spds^*$ tight-binding calculation for cubic semiconductors: General method and material parameters *Phys. Rev. B* **57** 6493–507

[130] Boykin T B 1997 Improved fits of the effective masses at Γ in the spin-orbit, second-nearest-neighbor sp^3s^* model: Results from analytic expressions *Phys. Rev. B* **56** 9613–8

[131] Chadi D J 1977 Spin-orbit splitting in crystalline and compositionally disordered semiconductors *Phys. Rev. B* **16** 790–6

[132] Rahman A 2005 Exploring new channel materials for nanoscale CMOS devices: a

simulation approach (Purdue University)

[133] Phillips J 1970 Ionicity of the Chemical Bond in Crystals *Rev. Mod. Phys.* **42** 317–56

[134] Braunstein R, Moore A and Herman F 1958 Intrinsic Optical Absorption in Germanium-Silicon Alloys *Phys. Rev.* **109** 695–710

[135] F.Bohren C and Huffman D R 1998 Absorption and Scattering of Light by Small Particles (New York, NY: John Wiley & Sons, Ltd)

[136] Brönstrup G, Jahr N, Leiterer C, Csáki A, Fritzsche W and Christiansen S 2010 Optical properties of individual silicon nanowires for photonic devices. *ACS Nano* **4** 7113–22

[137] Kallel H, Chehaidar A, Arbouet A and Paillard V 2013 Enhanced absorption of solar light in Ge/Si core-sheath nanowires compared to Si/Ge core-sheath and $Si_{1-x}Ge_x$ nanowires: A theoretical study *J. Appl. Phys.* **114** 224312

[138] Liu W F, Oh J I and Shen W Z 2011 Light Trapping in Single Coaxial Nanowires for Photovoltaic Applications *IEEE Electron Device Lett.* **32** 45–7

[139] Xie W Q, Liu W F, Oh J I and Shen W Z 2011 Optical absorption in c-Si/a-Si:H core/shell nanowire arrays for photovoltaic applications *Appl. Phys. Lett.* **99** 033107

[140] Anon ASTM AM 1.5G, G173-03, Terrestrial Reference Spectra for photovoltaic Performance Evaluation; *Am. Soc. Test. Mater.*

[141] Cao L, White J S, Park J-S, Schuller J a, Clemens B M and Brongersma M L 2009 Engineering light absorption in semiconductor nanowire devices. *Nat. Mater.* **8** 643–7

[142] Cao L, Fan P, Vasudev A P, White J S, Yu Z, Cai W, Schuller J A, Fan S and Brongersma M L 2010 Semiconductor nanowire optical antenna solar absorbers. *Nano Lett.* **10** 439–45

[143] Oh J Il, Liu W, Xie W and Shen W 2013 Light Trapping in Coaxial Nanowires of c-Si Cores and a-Si Shells Silicon-based Nanomaterials Springer Series in Materials Science vol 187, ed H Li, J Wu and Z M Wang (New York, NY: Springer New York)

[144] Snyder A W 1983 Optical Waveguide Theory (Berlin, Heidelberg: Springer, Berlin)

[145] Tompkins H G and Irene E A Handbook of ellipsometry ed H G Tompkins and E A Irene (Springer-Verlag, Berlin)

[146] Woollam J A 2000 Ellipsometry, variable angle spectroscopic, *Wiley Encyclopedia of Electrical and Electronics Engineering* ed J G Weber (New York, NY: Wiley)

[147] D'Costa V, Cook C, Birdwell A G, Littler C, Canonico M, Zollner S, Kouvetakis J and Menéndez J 2006 Optical critical points of thin-film $Ge_{1-y}Sn_y$ alloys: A comparative $Ge_{1-y}Sn_y$/$Ge_{1-x}Si_x$ study *Phys. Rev. B* **73** 125207

[148] Johs B, Herzinger C M, Dinan J H, Cornfeld A and Benson J . 1998 Development of a parametric optical constant model for $Hg_{1-x}Cd_xTe$ for control of composition by spectroscopic ellipsometry during MBE growth *Thin Solid Films* **313–314** 137–42

[149] Hu Y Z, Zettler J-T, Chongsawangvirod S, Wang Y Q and Irene E a. 1992 Spectroscopic ellipsometric measurements of the dielectric function of germanium dioxide films on crystal germanium *Appl. Phys. Lett.* **61** 1098

[150] Palik E D 1998 *Handbook of Optical Constants of Solids* ed E D Palik (London, UK: Academic Press)

[151] Wirths S, Tiedemann A T, Ikonic Z, Harrison P, Holländer B, Stoica T, Mussler G, Myronov M, Hartmann J M, Grützmacher D, Buca D and Mantl S 2013 Band engineering and growth of tensile strained Ge/(Si)GeSn heterostructures for tunnel field effect transistors *Appl. Phys. Lett.* **102** 192103–4

[152] Sun G, Cheng H H, Menéndez J, Khurgin J B and Soref R A 2007 Strain-free Ge/GeSiSn quantum cascade lasers based on L-valley intersubband transitions *Appl. Phys. Lett.* **90** 251105

[153] Gallagher J D, Xu C, Jiang L, Kouvetakis J and Menéndez J 2013 Fundamental band gap and direct-indirect crossover in $Ge_{1-x-y}Si_xSn_y$ alloys *Appl. Phys. Lett.* **103** 202104

[154] Kouvetakis J, Menendez J and Chizmeshya A V G 2006 Tin-Based Group IV Semiconductors: New Platforms for Opto- and Microelectronics on Silicon *Annu. Rev. Mater. Res.* **36** 497–554

[155] Moontragoon P, Soref R A and Ikonic Z 2012 The direct and indirect bandgaps of unstrained $Si_xGe_{1-x-y}Sn_y$ and their photonic device applications *J. Appl. Phys.* **112** 073106

[156] Kotlyar R, Avci U E, Cea S, Rios R, Linton T D, Kuhn K J and Young I A 2013 Bandgap

engineering of group IV materials for complementary n and p tunneling field effect transistors Bandgap engineering of group IV materials for complementary n and p tunneling field effect transistors *Appl. Phys. Lett.* **102** 113106

[157] Fournier-Lupien J-H, Mukherjee S, Wirths S, Pippel E, Hayazawa N, Mussler G, Hartmann J M, Desjardins P, Buca D and Moutanabbir O 2013 Strain and composition effects on Raman vibrational modes of silicon-germanium-tin ternary alloys *Appl. Phys. Lett.* **103** 263103

[158] Mourad D and Czycholl G 2012 Theory of band gap bowing of disordered substitutional II–VI and III–V semiconductor alloys *Eur. Phys. J. B* **85** 1–13

[159] Rowlands D, Staunton J, Györffy B, Bruno E and Ginatempo B 2005 Effects of short-range order on the electronic structure of disordered metallic systems *Phys. Rev. B* **72** 045101

[160] Zunger A, Wei S-H, Ferreira L G and Bernard J E 1990 Special quasirandom structures *Phys. Rev. Lett.* **65** 353–6

[161] Küfner S, Furthmüller J, Matthes L, Fitzner M and Bechstedt F 2013 Structural and electronic properties of α-tin nanocrystals from first principles *Phys. Rev. B* **87** 235307

[162] Luisier M, Schenk A, Fichtner W and Klimeck G 2006 Atomistic simulation of nanowires in the $sp^3d^5s^*$ tight-binding formalism: From boundary conditions to strain calculations *Phys. Rev. B* **74** 205323

[163] Yamaguchi E 1988 Superlattice Approach to the Interface States in III–V Semiconductors *J. Phys. Soc. Jpn.* **57** 2461–75

[164] Boykin T B, Klimeck G, Bowen R C and Lake R 1997 Effective-mass reproducibility of the nearest-neighbor sp^3s^* models: Analytic results *Phys. Rev. B* **56** 4102–7

[165] A. Jameson 1995 Gradient Based optimization methods (Stanford University)

[166] J.J. More 1977 The Levenberg-Marquardt algorithm: implementation and theory *Lect. notes Math.* **630** 105–16

[167] Bjoerk A e. a. 1996 Numerical methods for least squares problems *Soc. Ind. Math.*

[168] S. Kirkpatrick 1984 Optimization by simulated annealing: Quantitative studies *J. Stat. Phys.* **34** 975–86

[169] Chakrabarti B and Das A Quantum annealing and related optimization methods (Springer)

[170] Cole E a. B 2009 Genetic algorithms and simulated annealing Mathematical and Numerical Modelling of Heterostructure Semiconductor Devices: From Theory to Programming (Springer London) pp 339–76

[171] Starrost F, Bornholdt S, Solterbeck C and Schattke W 1996 Band-structure parameters by genetic algorithm *Phys. Rev. B* **53** 12549–52

[172] Storn R and Price K 1997 Differential Evolution – A Simple and Efficient Heuristic for global Optimization over Continuous Spaces *J. Glob. Optim.* **11** 341–59

[173] Shim K and Rabitz H 1998 Universal tight-binding calculation for the electronic structure of the quaternary alloy $In_{1-x}Ga_xAs_{1-y}P_y$ *Phys. Rev. B* **57** 12874–81

[174] Adachi S Properties of Group-IV, III-V and II-VI Semiconductors vol 1 (Japan: John Wiley & sons)

[175] Chelikowsky J R and Cohen M L 1976 Nonlocal pseudopotential calculations for the electronic structure of eleven diamond and zinc-blende semiconductors *Phys. Rev. B* **14** 556–82

[176] Sieh K S and Smith P V. 1985 A Localized Orbital Description of Si Using Non-Local Potentials *Phys. status solidi* **129** 259–69

[177] Masovic D R, Vukajlovic F R and Zekovic S 1983 Local-pseudopotential calculation for optical properties and photoemission valence-band spectrum of silicon *J. Phys. C Solid State Phys.* **16** 6731–8

[178] Wachs A L, Miller T, Hsieh T C, Shapiro A P and Chiang T-C 1985 Angle-resolved photoemission studies of Ge(111)-c(2×8), Ge(111)-(1×1)H, Si(111)-(7×7), and Si(100)-(2×1) *Phys. Rev. B* **32** 2326–33

[179] Madelung O 2004 Semiconductors: Data Handbook vol 1 (Springer)

[180] Pollak F H, Cardona M and Higginbotham C W 1970 Energy-Band Structure and Optical Spectrum of Grey Tin *Phys. Rev. B* **2** 352

[181] Brust D 1964 Electronic Spectra of Crystalline Germanium and Silicon *Phys. Rev.* **134** A1337–53

[182] Zwerdling S, Lax B, Roth L and Button K 1959 Exciton and Magneto-Absorption of the Direct and Indirect Transitions in Germanium *Phys. Rev.* **114** 80–9

[183] Cohen M L and Bergstresser T K 1966 Band Structures and Pseudopotential Form Factors for Fourteen Semiconductors of the Diamond and Zinc-blende Structures *Phys. Rev.* **141** 789–96

[184] Via L, Höchst H and Cardona M 1985 Dielectric function of α-Sn and its temperature dependence *Phys. Rev. B* **31** 958–67

[185] Farrow R F C, Robertson D S, Williams G M, Cullis A G, Jones G R, Young I M and Dennis P N J 1981 The growth of metastable, heteroepitaxial films of α-Sn by metal beam epitaxy *J. Cryst. Growth* **54** 507–18

[186] Klimeck G, Bowen R C, Boykin T B, Salazar-Lazaro C, Cwik T a and Stoica A 2000 Si tight-binding parameters from genetic algorithm fitting *Superlattices Microstruct.* **27** 77–88

[187] Brudevoll T, Citrin D S, Cardona M and Christensen N E 1993 Electronic structure of α-Sn and its dependence on hydrostatic strain *Phys. Rev. B* **48** 8629–35

[188] Lin H, Chen R, Lu W, Huo Y, Kamins T I and Harris J S 2012 Structural and optical characterization of $Si_xGe_{1-x-y}Sn_y$ alloys grown by molecular beam epitaxy *Appl. Phys. Lett.* **100** 141908

[189] Chen R, Lin H, Huo Y, Hitzman C, Kamins T I and Harris J S 2011 Increased photoluminescence of strain-reduced, high-Sn composition $Ge_{1-x}Sn_x$ alloys grown by molecular beam epitaxy *Appl. Phys. Lett.* **99** 181125

[190] Laude L, Pollak F and Cardona M 1971 Effects of Uniaxial Stress on the Indirect Exciton Spectrum of Silicon *Phys. Rev. B* **3** 2623–36

[191] Fischetti M V and Laux S E 1996 *Band structure , deformation potentials , and carrier mobility in strained Si , Ge , and SiGe alloys*

[192] El Kurdi M, Sauvage S, Fishman G and Boucaud P 2006 Band-edge alignment of SiGe/Si quantum wells and SiGe/Si self-assembled islands *Phys. Rev. B* **73** 195327

[193] Harrison W A 1980 Electronic Structure and the Properties of Solids: the physics of chemical bond (New York: Dover Publication, Inc)

[194] Priester C, Allan G and Lannoo M 1988 Band-edge deformation potentials in a tight-binding framework *Phys. Rev. B* **37** 8519–22

[195] Muñoz M C and Armelles G 1993 X-point deformation potentials of III-V semiconductors in a tight-binding approach *Phys. Rev. B* **48** 2839–42

[196] Ng G, Vasileska D and Schroder D K 2011 Empirical pseudopotential band structure parameters of 4H-SiC using a genetic algorithm fitting routine *Superlattices Microstruct.* **49** 109–15

[197] Van de Walle C G and Martin R M 1986 Theoretical calculations of heterojunction discontinuities in the Si/Ge system *Phys. Rev. B* **34** 5621–36

[198] Kurdi M El, Fishman G, Sauvage S and Boucaud P 2010 Band structure and optical gain of tensile-strained germanium based on a 30 band kp formalism *J. Appl. Phys.* **107** 013710

[199] Boykin T B, Kharche N, Klimeck G and Korkusinski M 2007 Approximate bandstructures of semiconductor alloys from tight-binding supercell calculations *J. Phys. Condens. Matter* **19**

[200] Li Y-H, Gong X G and Wei S-H 2006 Ab initio calculation of hydrostatic absolute deformation potential of semiconductors *Appl. Phys. Lett.* **88** 042104

[201] Lim P H, Park S, Ishikawa Y and Wada K 2009 Enhanced direct bandgap emission in germanium by micromechanical strain engineering *Opt. Express* **17** 16358

[202] Tahini H, Chroneos a, Grimes R W, Schwingenschlögl U and Dimoulas a 2012 Strain-induced changes to the electronic structure of germanium. *J. Phys. Condens. Matter* **24** 195802

[203] Rieger M and Vogl P 1993 Electronic-band parameters in strained Si1-xGex alloys on Si1-yGey substrates *Phys. Rev. B* **48** 14276–87

[204] Landolt-Bornstein 1982 Numerical Data and Functional Relationships in Science and Technology ed O Madelung (Springer-Verlag, Berlin)

[205] Chandrasekhar M and Pollak F 1977 Effects of uniaxial stress on the electroreflectance spectrum of Ge and GaAs *Phys. Rev. B* **15** 2127–44

[206] Balslev I 1966 Influence of Uniaxial Stress on the Indirect Absorption Edge in Silicon and

Germanium *Phys. Rev.* **143** 636–47

[207] Bir G L and Pikus G E 1974 Symmetry and Strain Induced Effects in Semiconductor (Wiley, New York)

[208] Schmidt O, Eberl K and Rau Y 2000 Strain and band-edge alignment in single and multiple layers of self-assembled Ge/Si and GeSi/Si islands *Phys. Rev. B* **62** 16715–20

[209] Fischetti M V and Laux S E 1996 Band structure, deformation potentials, and carrier mobility in strained Si, Ge, and SiGe alloys *J. Appl. Phys.* **80** 2234–52

[210] El Kurdi M, Sauvage S, Fishman G and Boucaud P 2006 Band-edge alignment of SiGe/Si quantum wells and SiGe/Si self-assembled islands *Phys. Rev. B* **73** 195327

[211] BLACHA A, PRESTING H and M. CARDONA 1984 Deformation Potentials of k = 0 States of Tetrahedral Semiconductors *Phys. status solidi* **126** 11–36

[212] Klimeck G, Chris Bowen R, Boykin T B and Cwik T A 2000 sp^3s^* Tight-binding parameters for transport simulations in compound semiconductors *Superlattices Microstruct.* **27** 519–24

[213] Bertoni A, Royo M, Mahawish F and Goldoni G 2011 Electron and hole gas in modulation-doped GaAs/$Al_{1-x}Ga_xAs$ radial heterojunctions *Phys. Rev. B* **84** 205323

[214] Long A W and Wong B M 2012 PAMELA: An open-source software package for calculating nonlocal exact exchange effects on electron gases in core-shell nanowires *AIP Adv.* **2** 032173

[215] Ram-Mohan L R 2004 The Schrödinger–Poisson self-consistency in layered quantum semiconductor structures *J. Appl. Phys.* **95** 3081

[216] Brongersma M L, Cui Y and Fan S 2014 Light management for photovoltaics using high-index nanostructures. *Nat. Mater.* **13** 451–60

[217] Landreman P E and Brongersma M L 2014 Deep-subwavelength semiconductor nanowire surface plasmon polariton couplers *Nano Lett.* **14** 429–34

[218] Falk A L, Koppens F H L, Yu C L, Kang K, de Leon Snapp N, Akimov A V., Jo M-H, Lukin M D and Park H 2009 Near-field electrical detection of optical plasmons and single-plasmon sources *Nat. Phys.* **5** 475–9

[219] Tanaka N 2010 *Technology Roadmap: Solar photovoltaic energy*

[220] Nositschka W A, Beneking C, Voigt O and Kurz H 2003 Texturisation of multicrystalline silicon wafers for solar cells by reactive ion etching through colloidal masks *Sol. Energy Mater. Sol. Cells* **76** 155–66

[221] Schneider B W, Lal N N, Baker-Finch S and White T P 2014 Pyramidal surface textures for light trapping and antireflection in perovskite-on-silicon tandem solar cells *Opt. Express* **22** A1422–30

[222] Lu W and Lieber C M 2007 Nanoelectronics from the bottom up. *Nat. Mater.* **6** 841–50

[223] Fan Z, Wang D, Chang P C, Tseng W Y and Lu J G 2004 ZnO nanowire field-effect transistor and oxygen sensing property *Appl. Phys. Lett.* **85** 5923–5

[224] Lauhon L J, Gudiksen M S, Wang D and Lieber C M 2002 Epitaxial core-shell and core-multishell nanowire heterostructures. *Nature* **420** 57–61

[225] Goto H, Nosaki K, Tomioka K, Hara S, Hiruma K, Motohisa J and Fukui T 2009 Growth of core-shell InP nanowires for photovoltaic application by selective-area metal organic vapor phase epitaxy *Appl. Phys. Express* **2** 3–6

[226] Tian B, Zheng X, Kempa T J, Fang Y, Yu N, Yu G, Huang J and Lieber C M 2007 Coaxial silicon nanowires as solar cells and nanoelectronic power sources. *Nature* **449** 885–9

[227] Yu Y, Ferry V E, Alivisatos A P and Cao L 2012 Dielectric core-shell optical antennas for strong solar absorption enhancement. *Nano Lett.* **12** 3674–81

[228] Schuller J A and Brongersma M L 2009 General properties of dielectric optical antennas. *Opt. Express* **17** 24084–95

[229] Tang L, Kocabas S E, Salman L, Okyay A K, Dany-Sebastien Ly-Gagnon, Saraswat K C and Miller D A B 2008 Nanometre-scale germanium photodetector enhanced by a near-infrared dipole antenna *Nat. Photonics* **2** 226–9

[230] Ahn D, Hong C-Y, Liu J, Giziewicz W, Beals M, Kimerling L C, Michel J, Chen J and Kärtner F X 2007 High performance, waveguide integrated Ge photodetectors. *Opt. Express* **15** 3916–21

[231] O'Brien S and Pendry J B 2002 Photonic band-gap effects and magnetic activity in

dielectric composites *J. Phys. Condens. Matter* **14** 4035–44

[232] Schuller J a., Zia R, Taubner T and Brongersma M L 2007 Dielectric metamaterials based on electric and magnetic resonances of silicon carbide particles *Phys. Rev. Lett.* **99** 1–4

[233] Muskens O L, Diedenhofen S L, Van Weert M H M, Borgström M T, Bakkers E P a M and Rivas J G 2008 Epitaxial growth of aligned semiconductor nanowire metamaterials for photonic applications *Adv. Funct. Mater.* **18** 1039–46

[234] Schuller J A, Taubner T and Brongersma M L 2009 Optical antenna thermal emitters *Nat. Photonics* **3** 658–61

[235] Soref R A and Perry C H 1991 Predicted band gap of the new semiconductor SiGeSn *J. Appl. Phys.* **69** 539–41

[236] Zelazna K, Welna M, Misiewicz J, Dekoster J and Kudrawiec R 2016 Temperature dependence of energy gap of $Ge_{1-x}Sn_x$ alloys with $x<0.11$ studied by photoreflectance *J. Phys. D. Appl. Phys.* **49**

[237] Ghetmiri S A, Du W, Margetis J, Mosleh A, Cousar L, Conley B R, Domulevicz L, Nazzal A, Sun G, Soref R A, Tolle J, Li B, Naseem H A and Yu S Q 2014 Direct-bandgap GeSn grown on silicon with 2230 nm photoluminescence *Appl. Phys. Lett.* **105** 2012–7

[238] Hartmann J M, Abbadie A, Papon A M, Holliger P, Rolland G, Billon T, Fédéli J M, Rouvière M, Vivien L and Laval S 2004 Reduced pressure-chemical vapor deposition of Ge thick layers on Si(001) for 1.3-1.55-μm photodetection *J. Appl. Phys.* **95** 5905–13

[239] Hartmann J M, Abbadie A, Cherkashin N, Grampeix H and Clavelier L 2009 Epitaxial growth of Ge thick layers on nominal and 6° off Si(0 0 1); Ge surface passivation by Si *Semicond. Sci. Technol.* **24** 055002

[240] Shah V A, Dobbie A, Myronov M and Leadley D R 2011 High quality relaxed Ge layers grown directly on a Si(001) substrate *Solid. State. Electron.* **62** 189–94

[241] Pettersson L A A, Roman L S and Inganäs O 2011 Modeling photocurrent action spectra of photovoltaic devices based on organic thin films Modeling photocurrent action spectra of photovoltaic devices based on organic thin films *J. Appl. Phys.* **487** 487–96

[242] Lu Y C, Yang L, Huang W P and Jian S S 2008 Improved full-vector finite-difference

complex mode solver for optical waveguides of circular symmetry *J. Light. Technol.* **26** 1868–76

[243] Grzela G, Paniagua-Domínguez R, Barten T, Fontana Y, Sánchez-Gil J A and Rivas J G 2012 Nanowire Antenna Emission *Nano Lett.* **12** 5481−5486

[244] Seo M-K, Yang J-K, Jeong K-Y, Park H-G, Qian F, Ee H-S, No Y-S and Leet Y-H 2008 Modal characteristics in a single-nanowire cavity with a triangular cross section. *Nano Lett.* **8** 4534–8

[245] Yu Y, Ferry V E, Alivisatos A P and Cao L 2012 Dielectric Core–Shell Optical Antennas for Strong Solar Absorption Enhancement *Nano Lett.* **12** 3674–81

[246] Khudiyev T, Huseyinoglu E and Bayindir M 2014 Non-resonant Mie scattering: emergent optical properties of core-shell polymer nanowires. *Sci. Rep.* **4** 4607

[247] Fano U 1961 Effects of Configuration Interaction on Intensities and Phase Shifts *Phys. Rev.* **124** 1866–78

[248] Shockley W and Queisser H J 1961 Detailed balance limit of efficiency of p-n junction solar cells *J. Appl. Phys.* **32** 510–9

[249] Cao L, Fan P, Barnard E S, Brown A M and Brongersma M L 2010 Tuning the color of silicon nanostructures. *Nano Lett.* **10** 2649–54

[250] Cao L, Park J-S, Fan P, Clemens B and Brongersma M L 2010 Resonant germanium nanoantenna photodetectors. *Nano Lett.* **10** 1229–33

[251] Kallel H, Chehaidar A, Arbouet A and Paillard V 2013 Enhanced absorption of solar light in Ge/Si core-sheath nanowires compared to Si/Ge core-sheath and Si1−xGex nanowires: A theoretical study *J. Appl. Phys.* **114** 224312

[252] Kischkat J, Peters S, Gruska B, Semtsiv M, Chashnikova M, Klinkmüller M, Fedosenko O, Machulik S, Aleksandrova A, Monastyrskyi G, Flores Y and Ted Masselink W 2012 Mid-infrared optical properties of thin films of aluminum oxide, titanium dioxide, silicon dioxide, aluminum nitride, and silicon nitride *Appl. Opt.* **51** 6789

[253] Kerr M J and Cuevas A 2002 Recombination at the interface between silicon and stoichiometric plasma silicon nitride *Semicond. Sci. Technol.* **17** 166–72

[254] MäcKel H and Lüdemann R 2002 Detailed study of the composition of hydrogenated SiNx layers for high-quality silicon surface passivation *J. Appl. Phys.* **92** 2602–9

[255] Kim S-K, Zhang X, Hill D J, Song K-D, Park J-S, Park H-G and Cahoon J F 2015 Doubling Absorption in Nanowire Solar Cells with Dielectric Shell Optical Antennas *Nano Lett.* **15** 753–8

[256] D'Avezac M, Luo J W, Chanier T and Zunger A 2012 Genetic-algorithm discovery of a direct-gap and optically allowed superstructure from indirect-gap Si and Ge semiconductors *Phys. Rev. Lett.* **108** 1–5

APPENDIX A – ENHANCED IR LIGHT ABSORPTION IN GROUP IV-SIGESN CORE-SHELL NANOWIRES

A.1. Lorentz-Mie scattering theory for an infinite core-shell cylindrical nanowire.

To quantify, the absorption and scattering efficiencies in the core-shell nanowire, we need to know the corresponding absorption and scattering expansion coefficients. Furthermore, we need to quantify the electrical $\vec{E}$ and magnetic fields $\vec{H}$ inside the core and the shell in addition to the incident and scattering fields. To include the effect of the incidence angle in our calculation, we present a general expression of the electromagnetic fields in the CSNW. For that, lets us consider a long cylindrical core-shell nanowire as shown in Figure S1 (where the length L is almost 10 times larger than the radial dimensions r) oriented along the $\boldsymbol{e}_z$ direction and having a core of radius r_c and a complex refractive index N_c and a shell of radius r_s with a complex refractive index N_s. It is better to define some reduced constant to simplify the final expression of the electromagnetic fields and thus the scattering and absorption efficiencies. In each medium, the wavenumber is given by $k_j = 2\pi N_j/\lambda$ where $j \in \{\boldsymbol{M}, \boldsymbol{c}, \boldsymbol{s}\}$ for an arbitrary nonabsorbing ***M***edium in which the CSNW is embedded, the ***c***ore and the ***s***hell respectively and N_j is the corresponding complex refractive index. Besides, we define an incidence angle ξ between the x- and z- axis. Finally, we define a dimensionless radius $\rho_j(r) = r\sqrt{k_j^2 - h^2}$ where $h_j = -k_j \cos\xi$ and $j \in \{M, c, s\}$ will be used. Furthermore, r can take either value of the outer radius r_s or the inner radius r_c.

We start by defining the general electromagnetic (EM) field's expression in three regions: the outer region of the nanowire where are the incident $\{E_{inc}, H_{inc}\}$ and scattered $\{E_{sca}, H_{sca}\}$ EM fields, the shell region $\{E_s, H_s\}$, and the core region $\{E_c, H_c\}$. The total EM field outside the nanowire $\{E_t, H_t\}$ is the sum of both incident and scattered fields. Extending the work of Ref. [1,2], we present a general expression for the unpolarized EM fields, then the TE and TM modes while considering an arbitrary angle of incidence. Firstly, the incident EM field is given by

$$\boldsymbol{E}_{inc} = \frac{E_0}{k_M \sin\xi} \sum_{n=-\infty}^{\infty} (-i)^n \left\{ \boldsymbol{N}_n^{(1)}(\rho_M) - i\boldsymbol{M}_n^{(1)}(\rho_M) \right\} e^{in\phi} e^{ihz}$$

$$\boldsymbol{H}_{inc} = \frac{-ik_M}{\omega\,\mu_0} \frac{E_0}{k_M \sin\xi} \sum_{n=-\infty}^{\infty} (-i)^n \left\{ \boldsymbol{N}_n^{(1)}(\rho_M) - i\boldsymbol{M}_n^{(1)}(\rho_M) \right\} e^{in\phi} e^{ihz} \tag{A-1}$$

Where $\boldsymbol{N}_n^{(1)}(\rho_M) = \frac{\sqrt{k_M^2 - h_M^2}}{k_M} \begin{bmatrix} ih_M J_n'(\rho_M) \\ -h_M n J_n(\rho_M)/\rho_M \\ \sqrt{k_M^2 - h_M^2} J_n(\rho_M) \end{bmatrix}$, $\boldsymbol{M}_n^{(1)}(\rho_M) = \sqrt{k_M^2 - h_M^2} \begin{bmatrix} in\, J_n(\rho_M)/\rho_M \\ J_n'(\rho_M) \\ 0 \end{bmatrix}$

and ω and μ_0 are the angular frequency and the permeability of free space, respectively.

Secondly, the EM fields of the scattered wave are:

$$\boldsymbol{E}_{sca} = \frac{E_0}{k_M \sin\xi} \sum_{n=-\infty}^{\infty} (-i)^n \left\{ a_n \boldsymbol{N}_n^{(3)}(\rho_M) - ib_n \boldsymbol{M}_n^{(3)}(\rho_M) \right\} e^{in\phi} e^{ihz}$$

$$\boldsymbol{H}_{sca} = \frac{-ik_M}{\omega\,\mu_0} \frac{E_0}{k_M \sin\xi} \sum_{n=-\infty}^{\infty} (-i)^n \left\{ b_n \boldsymbol{N}_n^{(3)}(\rho_M) - ia_n \boldsymbol{M}_n^{(3)}(\rho_M) \right\} e^{in\phi} e^{ihz} \tag{A-2}$$

Where $\boldsymbol{N}_n^{(3)}(\rho_M) = \frac{\sqrt{k_M^2 - h_M^2}}{k_M} \begin{bmatrix} ih_M H_n'(\rho_M) \\ -h_M n H_n(\rho_M)/\rho_M \\ \sqrt{k_M^2 - h_M^2} H_n(\rho_M) \end{bmatrix}$, $\boldsymbol{M}_n^{(3)}(\rho_M) = \sqrt{k_M^2 - h_M^2} \begin{bmatrix} in\, H_n(\rho_M)/\rho_M \\ H_n'(\rho_M) \\ 0 \end{bmatrix}$

where a_n and b_n are the scattering field expansion coefficients.

Thirdly, the EM fields of the wave inside the core are:

$$\boldsymbol{E}_c = \frac{E_0}{k_c \sin\xi} \sum_{n=-\infty}^{\infty} (-i)^n \left[\alpha_n^c \boldsymbol{N}_n^{(1)}(\rho_c) - i\beta_n^c \boldsymbol{M}_n^{(1)}(\rho_c) \right] e^{in\phi} e^{ihz}$$

$$\boldsymbol{H}_c = \frac{-ik_c}{\omega\,\mu_0} \frac{E_0}{k_c \sin\xi} \sum_{n=-\infty}^{\infty} (-i)^n \left[\beta_n^c \boldsymbol{N}_n^{(1)}(\rho_c) - i\alpha_n^c \boldsymbol{M}_n^{(1)}(\rho_c) \right] e^{in\phi} e^{ihz} \tag{A-3}$$

Where $\boldsymbol{N}_n^{(1)}(\rho_c) = \frac{\sqrt{k_c^2 - h_c^2}}{k_c} \begin{bmatrix} ih_c J_n'(\rho_c) \\ -h_c n J_n(\rho_c)/\rho_c \\ \sqrt{k_M^2 - h_c^2} J_n(\rho_c) \end{bmatrix}$, $\boldsymbol{M}_n^{(1)}(\rho_c) = \sqrt{k_c^2 - h_c^2} \begin{bmatrix} in\, J_n(\rho_c)/\rho_c \\ J_n'(\rho_c) \\ 0 \end{bmatrix}$

Finally, the EM fields of the wave inside the shell are:

$$\boldsymbol{E}_s = \frac{E_0}{k_s \sin\xi} \sum_{n=-\infty}^{\infty} (-i)^n \left\{ \left[\alpha_n^s \boldsymbol{N}_n^{(1)}(\rho_s) + \gamma_n^s \boldsymbol{N}_n^{(2)}(\rho_s) \right] - i \left[\beta_n^s \boldsymbol{M}_n^{(1)}(\rho_s) + \delta_n^s \boldsymbol{M}_n^{(2)}(\rho_s) \right] \right\} e^{in\phi} e^{ihz}$$

$$\boldsymbol{H}_s = \frac{-ik_s}{\omega\,\mu_0} \frac{E_0}{k_s \sin\xi} \sum_{n=-\infty}^{\infty} (-i)^n \left\{ \left[\beta_n^s \boldsymbol{N}_n^{(1)}(\rho_s) + \delta_n^s \boldsymbol{N}_n^{(2)}(\rho_s) \right] - i \left[\alpha_n^s \boldsymbol{M}_n^{(1)}(\rho_s) + \gamma_n^s \boldsymbol{M}_n^{(2)}(\rho_s) \right] \right\} e^{in\phi} e^{ihz} \quad \text{(A-4)}$$

Where $\boldsymbol{N}_n^{(1)}(\rho_s) = \frac{\sqrt{k_s^2 - h_s^2}}{k_s} \begin{bmatrix} ih_s J_n'(\rho_s) \\ -h_s n J_n(\rho_s)/\rho_s \\ \sqrt{k_s^2 - h^2}\, J_n(\rho_s) \end{bmatrix}$, $\boldsymbol{N}_n^{(2)}(\rho_s) = \frac{\sqrt{k_s^2 - h_s^2}}{k_s} \begin{bmatrix} ih_s Y_n'(\rho_s) \\ -h_s n Y_n(\rho_s)/\rho_s \\ \sqrt{k_s^2 - h_s^2}\, Y_n(\rho_s) \end{bmatrix}$,

$$\boldsymbol{M}_n^{(1)}(\rho_s) = \sqrt{k_s^2 - h_s^2} \begin{bmatrix} in\, J_n(\rho_s)/\rho_s \\ J_n'(\rho_s) \\ 0 \end{bmatrix}, \qquad \boldsymbol{M}_n^{(2)} = \sqrt{k_s^2 - h_s^2} \begin{bmatrix} in\, Y_n(\rho_s)/\rho_s \\ H_n'(\rho_s) \\ 0 \end{bmatrix}$$

where α_n^j, γ_n^j are the expansion coefficients of the TM modes and β_n^j, δ_n^j are those of the TE modes in the shell ($j = s$) and in the core ($j = c$) and a_n and b_n are the expansion coefficients of the TM and TE modes, respectively, of the scattered wave.[3]

Next, Applying Maxwell's boundary conditions at the interfaces and the cylinder surface, the expansion coefficients of all waves inside the multilayered cylinder and of the scattered wave can be resolved by evaluating the following continuity equations

$$(\boldsymbol{E}_s - \boldsymbol{E}_c) \times \boldsymbol{e}_r = \boldsymbol{0}\,;\ (\boldsymbol{H}_s - \boldsymbol{H}_c) \times \boldsymbol{e}_r = \boldsymbol{0}$$
$$(\boldsymbol{E}_{sca} + \boldsymbol{E}_{inc} - \boldsymbol{E}_s) \times \boldsymbol{e}_r = \boldsymbol{0}\,;\ (\boldsymbol{H}_{sca} + \boldsymbol{H}_{inc} - \boldsymbol{H}_c) \times \boldsymbol{e}_r = \boldsymbol{0} \quad \text{(A-5)}$$

We can therefore set up an inhomogeneous system of linear equations $A\boldsymbol{x} = \boldsymbol{u}$ where A is an 8×8

$$\boldsymbol{u} = \begin{bmatrix} 0 \\ 0 \\ 0 \\ 0 \\ -\frac{k_M^2 - h_M^2}{k_M^2} J_n[\rho_M(r_s)] \\ -\frac{k_M^2 - h_M^2}{k_M^2} \frac{J_n[\rho_M(r_s)]}{\rho_M(r_s)} - i \frac{\sqrt{k_M^2 - h^2}}{k_M} J_n'[\rho_M(r_s)] \\ \frac{(k_M^2 - h_M^2)}{k_M} J_n[\rho_M(r_s)] \\ \frac{\sqrt{k_M^2 - h_M^2}}{k_M} hn \frac{J_n[\rho_M(r_s)]}{\rho_M(r_s)} + i\sqrt{k_M^2 - h_M^2} J_n'[\rho_M(r_s)] \end{bmatrix}; \boldsymbol{x} == \begin{bmatrix} a_n \\ b_n \\ \alpha_n^c \\ \beta_n^c \\ \alpha_n^s \\ \beta_n^s \\ \gamma_n^s \\ \delta_n^s \end{bmatrix} \quad \text{(A-6)}$$

matrix for the unpolarised case, **x** is a 8×1 vector of the expansion coefficients defined earlier and $\boldsymbol{u}$ is a constant vector. $\boldsymbol{x}$ and $\boldsymbol{u}$ are given in equation (A-6).

The matrix A is given in full detail in the equation below while considering a random incident wave of angle ξ.

$$A = \begin{bmatrix} 0 & 0 & -A_{13}^{c,c,J_n} & 0 & A_{15}^{s,c,J_n} & A_{16}^{s,c,Y_n} & 0 & 0 \\ 0 & 0 & -B_{23}^{c,c,J_n} & -C_{24}^{c,c,J_n} & B_{25}^{s,c,J_n} & iC_{26}^{s,c,J_n} & B_{27}^{s,c,Y_n} & iC_{28}^{s,c,Y_n} \\ 0 & 0 & 0 & D_{34}^{c,c,J_n} & 0 & -D_{36}^{s,c,J_n} & 0 & -D_{38}^{s,c,Y_n} \\ 0 & 0 & ik_cC_{43}^{c,c,J_n} & k_cB_{44}^{c,c,J_n} & -ik_sC_{45}^{s,c,J_n} & -k_sB_{46}^{s,c,J_n} & -ik_sC_{47}^{s,c,J_n} & -k_sB_{48}^{s,c,Y_n} \\ A_{51}^{M,s,H_n} & 0 & 0 & 0 & -A_{55}^{s,s,J_n} & 0 & 0 & A_{58}^{s,s,Y_n} \\ B_{61}^{M,s,H_n} & ik_MC_{62}^{M,s,H_n} & 0 & 0 & -B_{65}^{s,s,J_n} & -ik_sC_{66}^{s,s,J_n} & -B_{67}^{s,s,Y_n} & -ik_sC_{68}^{s,s,Y_n} \\ 0 & -k_MA_{72}^{M,s,H_n} & 0 & 0 & 0 & k_sA_{76}^{s,s,J_n} & 0 & k_sA_{78}^{s,s,Y_n} \\ -ik_MC_{81}^{M,s,H_n} & -k_MB_{82}^{M,s,H_n} & 0 & 0 & k_sC_{85}^{s,s,J_n} & k_sB_{86}^{s,s,J_n} & ik_sC_{87}^{s,s,Y_n} & k_sB_{88}^{s,s,Y_n} \end{bmatrix}$$

where each entry of the matrix A is described in detail in equation (A-7).

$$A_{pq}^{i,j,Z_n} = \frac{k_i^2 - h_i^2}{k_i^2} Z_n[\rho_i(r_j)];\ B_{pq}^{i,j,Z_n} = \frac{\sqrt{k_i^2 - h_i^2}}{k_i^2} hn \frac{Z_n[\rho_i(r_j)]}{\rho_i(r_j)}$$

$$C_{pq}^{i,j,Z_n} = \frac{\sqrt{k_i^2 - h_i^2}}{k_i} Z_n'[\rho_i(r_j)];\ D_{pq}^{i,j,Z_n} = \frac{(k_i^2 - h_i^2)}{k_i} Z_n[\rho_i(r_j)] \tag{A-7}$$

$$i, j \in \{(M, c, s) \times (c, s)\}; Z_n \in \{J_n, Y_n, H_n\}$$

It is important to mention that the matrix A is ill-conditioned, which implies the non-uniqueness of solutions for the equation $A.x = u$. Nevertheless, it is possible to solve it using GMRES algorithm already available in MATLAB® after improving the ill-conditioned matrix A using the method described in Ref. [4] .It is worth noting that the novelty of this approach resides in the explicit dependence of the TM and TE modes with the incidence angle ξ.

Furthermore, after we have obtained the electromagnetic fields inside the core and the shell as well as the scattered fields by the cylindrical core-shell nanowire, we can determine the Poynting vector at any point in space as a possible way to quantify energy distribution inside the core-shell structure, we evaluated the normalized time-averaged Poynting vector defined as

$$\langle \boldsymbol{S} \rangle = Re[\boldsymbol{E} \times \boldsymbol{H}^*] \tag{A-8}$$

We focused on the TE-TM polarization of the Poynting vector but we presented only the TM-like mode, due to low scattering and absorption efficiencies of TE-like mode at small core radii, where the highest efficiencies are usually located.

Finally, the analysis for the Si/$Ge_{0.88}Sn_{0.12}$/Si_3N_4 NW structure is similar to the CSNW one. Nevertheless, the differences will emerge when writing the EM field continuity equation around the three different interfaces: core/ inner-shell, inner-shell/outer-shell and outer-shell/medium (air). The mathematics development will not be shown here because it is similar to the CSNW case.

A.2. Experimental Validation of the Mie-Lorentz Calculation scattering for SiNW

It is important to evaluate the correctness and the exactitude of the Mie-Lorentz scattering approach before endeavouring in more complicated computation. For that reason, we start by studying the simplest system of SiNW by calculating the absorption or scattering efficiencies and comparing the results to the experimental measurement or theoretical calculation, reported in literature whenever available. Initially, we validate our calculation by reproducing the TE-polarized scattering efficiency of the SiNW based on the work of R. P-Dominguez et *al.*[5] The results are shown in Figure A.2(a) where we can see that we accurately reproduce the same resonance peaks for a silicon cylinder with a 180 nm radius as in Figure 1 from the previous reference. Additionally, we replicate the experimental measurement of scattering efficiencies of silicon nanowires with different diameters ranging from 30 to 180 nm, presented in the Figure 2b in the work of Cao et *al.*[6]. However, we need to verify that the approximation of infinitely long nanowire used in the Mie-Lorentz formalism still hold, where the diameter to the length ratio need to be negligible before 10($d/L \ll 10$). For instance, by inspecting the Figure 1b from the aforementioned reference, we can deduce that the length of the NW is approximately 8 μm and by comparing it to the biggest diameter (180 nm) from Figure A.2(b) [6], we can deduce that $d/L = 0.0225 \ll 10$. Thus, we can ascertain that the approximation of infinitely long nanowire still holds. Next, we present the result of our simulation in Figure A.2(b).

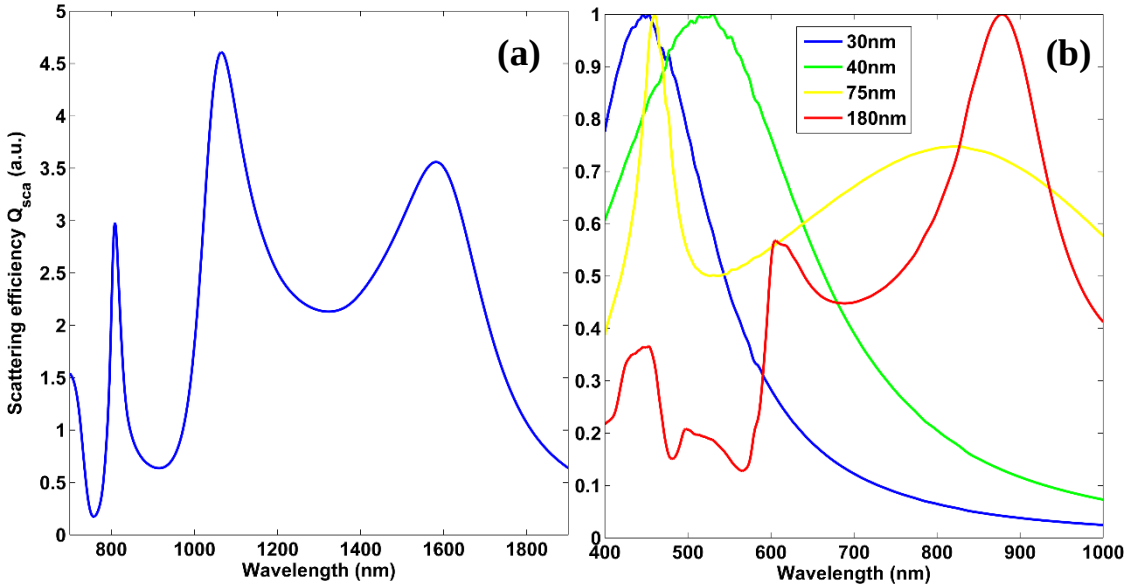

Figure A.2: Scattering efficiency of silicon nanowire **(a)** with a radius of 180 nm under TE-polarized plane wave incidence based on Ref. [5] and **(b)** with different diameters of 30 nm (blue), 40 nm (green), 75 nm (yellow), and 180 nm (red) under randomly polarized light based on Ref. [6] calculated with the Mie-Lorentz scattering formalism. The Q_{sca} was normalized to highlight spectral changes.

A.3. Full-Vector Finite-Difference complex mode solver for CSNW

To better understand the correlation between the geometrical dimension of the CSNW (the core radius and the shell thickness) and the absorption, we present in Figure A.3(a), we fix the core radius to 60 nm and we vary the shell thickness from $0.25 \times R_c$ to R_c. We can clearly see the Leaky mode TM_{41} highlighted with an eclipse. When the shell thickness increases, the leaky resonance mode moves toward longer wavelength, thus the polarized light is redshifted.

In addition, to better analyze the effect of the geometrical dimensions on the leaky modes of the CSNW, we used the improved full-vector Finite Difference (FVFD) mode solver for general circular waveguides, proposed in References [7,8], coupled with the coordinate stretching technique to implement the Perfectly Matched Layer (PML) boundary condition, in order to accurately extract and distinguish the leaky modes from the guided ones. Thus, we find the complex effective refractive index n_{eff} of the CSNW. Each complex solution is the eigenvalue of a specific

leaky mode. The real part (N_{real}) of the eigenvalue is related with the wavelength where the optical resonance (LMRs) takes place ($\lambda = 2\pi r_c/N_{real}$), and the imaginary part (N_{imag}) dictates the spectral width of the optical resonance. The Leaky waveguide modes are classified based on their azimuthal mode number, *m*, their radial mode number, *n*, which arises from the oscillatory behavior of the Bessel functions, and their polarization. Their polarization can be either TM (transverse magnetic, H_z=0), TE (transverse electric, $E_z = 0$), HE (magnetoelectric, TM-like), or EH (electromagnetic, TE-like). The only modes that are strictly TE or TM for arbitrary wavevector are the 0th order azimuthal modes, TM_{0n} and TE_{0n}. From the field profiles, presented in Supplementary Figure S3b, it is clear that the peaks at the 354 nm and 644 nm can be attributed to the HE_{11} and TM01 leaky waveguide modes, respectively when $R_c = 8\,nm$ and $t = 0.25R_c$. When $R_c = 60\,nm$, there are 3 main modes that are present: TM_{21}, TM_{31} and TM_{41} having respectively the following resonant wavelength: 988.3 nm, 851.7 nm and 681.2 nm. The field profiles of these modes, as determined from FVFD, can be found in references [9–11]. From absorption and scattering spectra, it can be observed that the lower modes broaden in scattering spectra and higher orders tend to disappear entirely, especially for smaller sizes (red curve of Figure A.3(b)), whereas for larger size, higher orders appear at near infrared region of the spectrum.

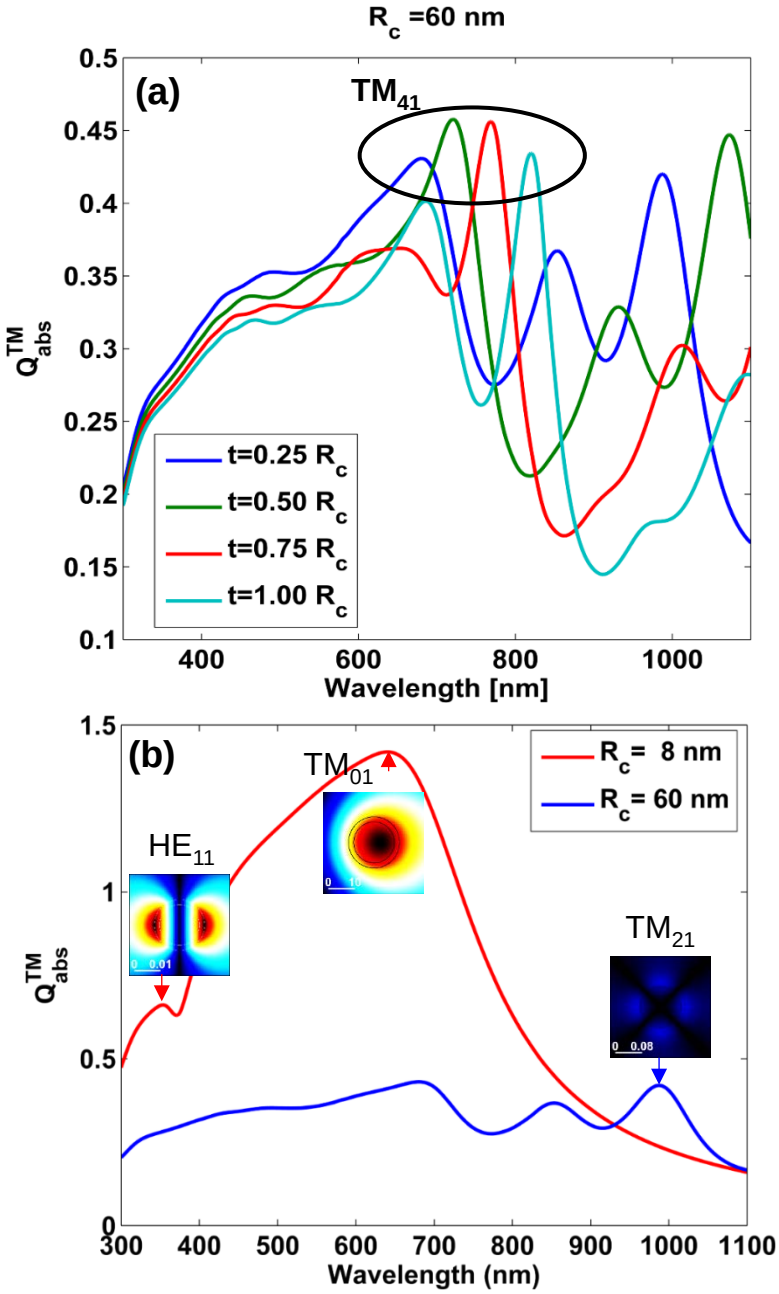

Figure A.3: **(a)** Effect of the shell thickness t on the leaky mode spectral position for the Si/GeSn CSNW. We specifically highlight the correlation between the shell thickness and the TM_{41} leaky mode for a core radius of 60 nm. Next, we present in panel **(b)** TM polarized absorption efficiency of Si/GeSn CSNW for 2 distinct core radii of 8 nm (red curve) and 60 nm (blue curve) and a shell thickness of $t = 0.25R_c$ as well as some corresponding electric field profile at the corresponding wavelength 354 (HE_{11}) and 644 nm (TM_{01}) for R_c=8 nm and 989 nm (TM_{21}) for R_c=60 nm.

A.4. Light Absorption Enhancement in $Ge/Ge_{0.88}Sn_{0.12}$ and $Si/Ge_{0.84}Si_{0.04}Sn_{0.12}$ CSNWs

We evaluate light absorption enhancement η_{abs} relative to SiNW for $Si/Ge_{0.88}Si_{0.04}Sn_{0.12}$ CSNW and relative to GeNW for $Ge/Ge_{0.88}Sn_{0.12}$ CSNW. We show in Figure A.4 the extreme enhancement for Si based CSNW in the NIR region. The $Ge/Ge_{0.88}Sn_{0.12}$ CSNW is a less efficient light absorber than the $Si/Ge_{0.88}Si_{0.12}Sn_{0.04}$ CSNW. We get for $Ge/Ge_{0.88}Sn_{0.12}$ CSNW at specific core radius 31 nm and shell thickness ($t = R_c$) and at a wavelength of 1100 nm, a 12-fold absorption enhancement compared to the GeNW.

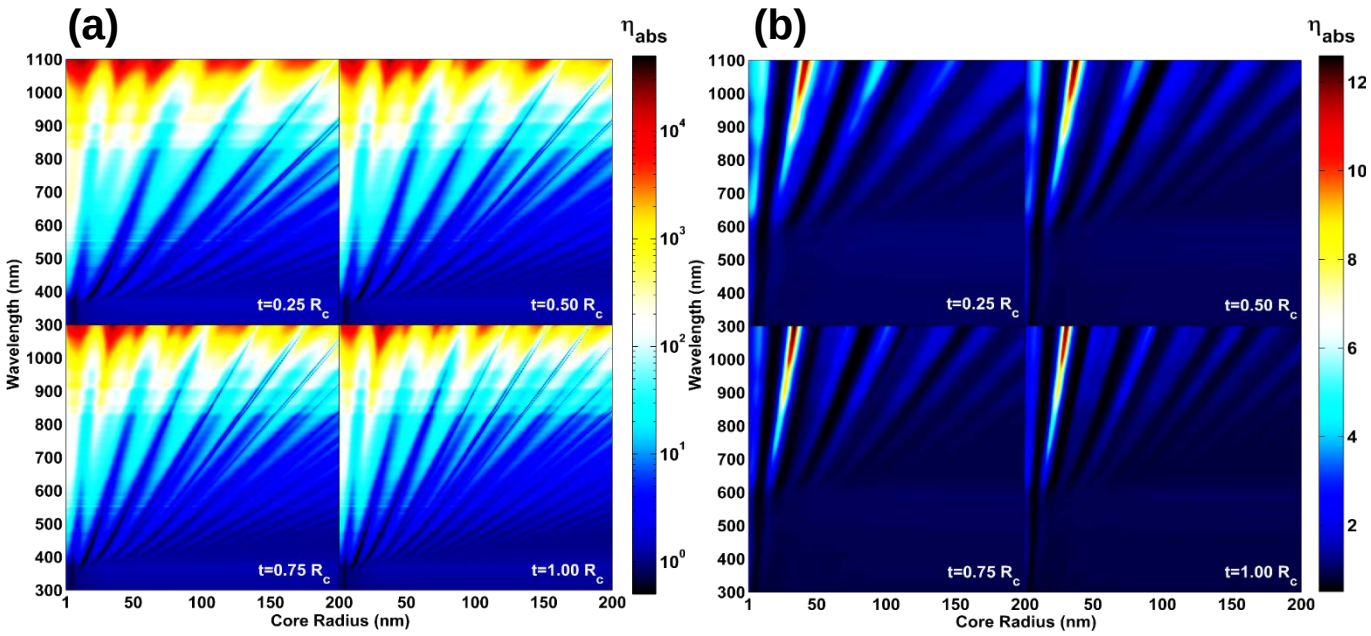

Figure A.4: Extreme light absorption enhancement map as a function of the core radius and the incident light wavelength for the **(a)** $Si/Ge_{0.84}Si_{0.04}Sn_{0.12}$ and **(b)** $Ge/Ge_{0.88}Sn_{0.12}$ CSNW for different shell thicknesses t= [0.25, 0.5, 0.75, 1] ×R_c.

A.5. References

[1] Mann S A and Garnett E C 2013 Extreme light absorption in thin semiconductor films wrapped around metal nanowires. *Nano Lett.* **13** 3173–8

[2] Kerker M and Matijević E 1961 Scattering of Electromagnetic Waves from Concentric Infinite Cylinders *J. Opt. Soc. Am.* **51** 506

[3] Quinten M 2011 *Optical Properties of Nanoparticle Systems: Mie and beyond* (Weinheim, Germany: Wiley-VCH Verlag GmbH & Co. KGaA)

[4] Rump S M 2009 Inversion of extremely Ill-conditioned matrices in floating-point *Jpn. J. Ind. Appl. Math.* **26** 249–77

[5] Paniagua-Domínguez R, Abujetas D R and Sánchez-Gil J A 2013 Ultra low-loss, isotropic optical negative-index metamaterial based on hybrid metal-semiconductor nanowires. *Sci. Rep.* **3** 1507

[6] Cao L, Fan P, Barnard E S, Brown A M and Brongersma M L 2010 Tuning the color of silicon nanostructures. *Nano Lett.* **10** 2649–54

[7] Lu Y C, Yang L, Huang W P and Jian S S 2008 Improved full-vector finite-difference complex mode solver for optical waveguides of circular symmetry *J. Light. Technol.* **26** 1868–76

[8] Chiang Y C, Chiou Y P and Chang H C 2002 Improved full-vectorial finite-difference mode solver for optical waveguides with step-index profiles *J. Light. Technol.* **20** 1609–18

[9] Grzela G 2013 *Directional Light Emission and Absorption by Semiconductor Nanowires,* (Eindhoven University of Technology)

[10] Cao L 2010 *Optical Resonances of Semiconductor Nanowires,* (Stanford University.)

[11] Snyder A W and Love J D 1983 *Optical Waveguide Theory* (Springer Berlin Heidelberg)

APPENDIX B – PUBLICATIONS RELATED TO THIS WORK

Articles:

[1] **Attiaoui A** and Moutanabbir O 2014 Indirect-to-direct band gap transition in relaxed and strained $Ge_{1-x-y}Si_xSn_y$ ternary alloys *J. Appl. Phys.* **116** 063712

[2] **Attiaoui A** and Moutanabbir O 2014 Optical and Electronic Properties of GeSn and GeSiSn Heterostructures and Nanowires *ECS Trans.* **64** 869–79

[3] **Attiaoui A**, Wirth S, Blanchard-Dionne A-P, Meunier M, Hartmann J M, Buca D and Moutanabbir O 2018 Extreme IR absorption in group IV-SiGeSn core-shell nanowires *J. Appl. Phys.* **123** 223102

[4] Juneau-Fecteau A, **Attiaoui A**, Moutanabbir O, Belarouci A and Fréchette L Selective Thermal Emission from a Polar Material on a Porous Silicon Photonic Crystal, submitted to ACS photonics

[5] Assali S, **Attiaoui A**, Hébert A, Mukherjee S and Moutanabbir O *Visible to mid-IR optical properties of TEOS spin-on-glass layers for low temperature opto-electronic device processing,* submitted to JVSTB

Conferences and talks

[6] S. Mukherjee, **A. Attiaoui**, and O. Moutanabbir*, Nuclear spin, Phonon and Bandgap Engineering in group IV nanowires, MRS spring 2015, California USA

[7] **A. Attiaoui**, S. Mukherjee, J.-H. Fournier-Lupien, and O. Moutanabbir*, Silicon-Germanium-Tin Heterostructures and Nanowires, MRS Spring 2015, California USA

[8] **A. Attiaoui** and O. Moutanabbir*, Optical and Electronic Properties of GeSn and GeSiSn Heterostructures and Nanowires, ECS 226th Meeting, Cancun Mexico, 7 octobre 2014

[9] **A. Attiaoui***, J.-H. Fournier-Lupien, Shedding new light on silicon, Global Material network (GMN), 13 May 2014, Montreal Canada (Invited speaker)

[10] N. Rousset*, J. Villeneuve, Jean-Hughes Fournier-Lupien, **A. Attiaoui**, G. Taillon, S. Francoeur and O. Daigle, EMCCD post-processing methods: Comparison for photon counting flux imaging, SPIE Conference, June 22nd, 2014, Montreal Canada

[11] S. Mukherjee*, **A. Attiaoui**, S. Wirths, H. Watanabe, D. Isheim, D. N. Seidman, and O. Moutanabbir, 3D Atom-By-Atom Mapping Of Emerging Group IV Semiconductors, ICSI9 2015, Montreal

[12] S. Assali*, **A. Attiaoui**, O. Moutanabbir, Enhanced IR Light Absorption in Direct Band Gap Group IV-SiGeSn Core/Shell Nanowire Arrays, PCSI-44 Santa Fe, USA, 17 Januray 2016

[13] **A. Attiaoui***, O. Moutanabbir, Extreme IR Light Absorption in Group IV-SiGeSn Core-Shell Nanowires, MRS Phoenix, USA, 17 Avril 2017

[14] S. Assali*, **A. Attiaoui**, S. Mukherjee, M-F. Deschênes, E. Bouthillier, and O. Moutanabbir, Silicon-Germanium-Tin Nanowires : Growth, Structure, and Device Properties, Invited talk, MRS Phoenix, USA, 18 Avril 2017.

[15] S. Assali*, **A. Attiaoui**, S. Mukherjee, and O. Moutanabbir, Structural and Optical Properties of SiGeSn nanowires, ICSI10 Warwick, UK, 17 May 2017.

[16] **A. Attiaoui***, Samik Mukherjee and Oussama Moutanabbir, Field evaporation of epitaxial diamond isotopic homojunctions, ICSI10 Warwick, UK, 17 May 2017.

[17] **A. Attiaoui***, Samik Mukherjee and Oussama Moutanabbir, The underlying physics of laser-assisted atom-by-atom- Field evaporation of diamond nanotips, CSSTC, Waterloo Canada, 22 August 2017.